# The properties of hydrogen and helium under extreme conditions

Jeffrey M. McMahon

*Department of Physics, University of Illinois at Urbana-Champaign, Urbana, Illinois 61801, USA*

Miguel A. Morales

*Lawrence Livermore National Laboratory, Livermore, California 94550, USA*

Carlo Pierleoni

*Department of Physical and Chemical Sciences, University of L'Aquila and CNISM UdR L'Aquila, Via Vetoio 10, I-67010 L'Aquila, Italy*

David M. Ceperley*

*Department of Physics, University of Illinois at Urbana-Champaign, Urbana, Illinois 61801, USA and NCSA, University of Illinois at Urbana-Champaign, Urbana, Illinois 61801, USA*

(published 13 November 2012)

Hydrogen and helium are the most abundant elements in the Universe. They are also, in principle, the most simple. Nonetheless, they display remarkable properties under extreme conditions of pressure and temperature that have fascinated theoreticians and experimentalists for over a century. Advances in computational methods have made it possible to elucidate ever more of their properties. Some of these methods that have been applied in recent years, in particular, those that perform simulations directly from the physical picture of electrons and ions, such as density functional theory and quantum Monte Carlo are reviewed. The predictions from such methods as applied to the phase diagram of hydrogen, with particular focus on the solid phases and the liquid-liquid transition are discussed. The predictions of ordered quantum states, including the possibilities of a low- or zero-temperature quantum fluid and high-temperature superconductivity are also considered. Finally, pure helium and hydrogen-helium mixtures, the latter which has particular relevance to planetary physics, are discussed.

DOI: 10.1103/RevModPhys.84.1607 PACS numbers: 62.50.−p, 67.80.F−, 81.30.−t, 61.20.Ja

**CONTENTS**



*ceperley@illinois.edu

 © 2012 American Physical Society

## I. INTRODUCTION

Hydrogen (H), being the first element, is correspondingly referred to as the most simple. The equations of quantum mechanics can be solved exactly for a single atom, which thus forms the mainstay problem of elementary quantum mechanics. The helium (He) atom, with only two electrons, is no longer analytically solvable, but still relatively simple. Despite their atomic simplicities, however, bulk hydrogen and helium are surprisingly complex. In this review, we describe what has been learned from experiments, theory, and computation about bulk hydrogen and helium under a variety of thermodynamic conditions of pressure and temperature, with particular focus on extreme conditions that are hard to achieve in the laboratory.

The primary motivation to study dense hydrogen and helium comes from the fact that they are the most abundant elements in the Universe. For example, they form ~70%–95% of the mass of Jupiter and Saturn in our Solar System, and are also the principle components of a large number of recently discovered exoplanets (Baraffe, Chabrier, and Barman, 2010). What is needed to model such planets is the equilibrium equation of state (EOS), the pressure as a function of temperature, density, and composition. Errors in the EOS lead to unreliable estimates of what is inside a planet, whether there are elements other than hydrogen and helium, their past history, and the process of their formation (Fortney, 2004; Fortney and Nettelmann, 2010). A long-standing puzzle, for example, is to understand why Saturn is ~50% more luminous than existing models. One possible explanation is additional energy sources that could come from H-He demixing (Fortney and Hubbard, 2003), as proposed by Smoluchowski (1967). In addition, the abundance in Saturn's atmosphere shows depletion of helium. Working backward from such astronomical observations though is a very indirect and uncertain way of learning about the phase diagram of H-He mixtures. Going the other way, it is estimated that the EOS needs to be accurate to ~1% to answer such fundamental questions about or make models regarding the composition and formation of planets (Stevenson, 2010).

Figure 1 shows the part of the phase diagram accessible to experiment along with the conditions needed to understand the planets. The isentropes of some of the well-characterized giant planets, including Jupiter and Saturn (Saumon and Guillot, 2004), the exoplanet HD 209458b (Guillot and Showman, 2002; Nellis, 2006b), and a representative brown dwarf G1 229B (Burrows *et al.*, 2001), are all shown. As seen, the isentropes lie outside the realm of static diamond

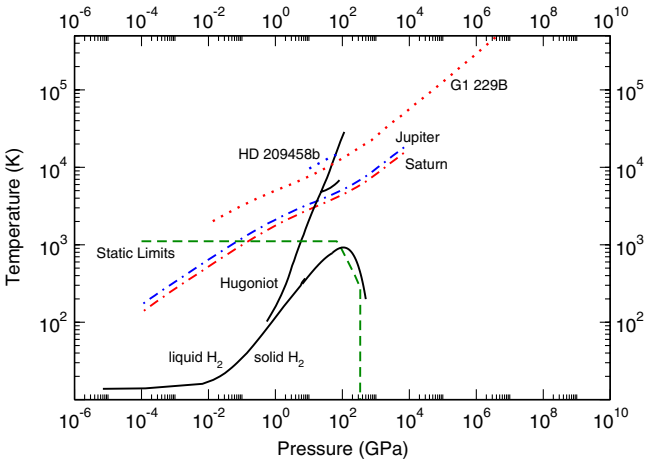


FIG. 1 (color online). A partial phase diagram of hydrogen. The principal Hugoniot (the pressures and temperatures that can be reached by shocking solid hydrogen initially at atmospheric pressure) is shown as a solid line and the secondary Hugoniot (i.e., points reached with a double shock) is shown branching from it. The isentropes of three giant planets (Jupiter, Saturn, and HD 209458b) and a representative brown dwarf (G1 229B) are shown using dashed lines. The estimated melting temperature of $H_2$ is shown as a solid line as well. Static DAC experiments, shown using a dashed line, are able to probe pressures less than ~300 GPa and temperatures less than 1100 K.

anvil cell (DAC) experiments, since these reliably only extend to pressures of ~320 GPa (Goncharov *et al.*, 2001; Loubeyre, Occelli, and LeToullec, 2002) and at relatively low temperatures, such as 1115 K at 73 GPa (Gregoryanz *et al.*, 2003). The experimental range of static measurements is depicted in Fig. 1. Dynamic shock compression (Nellis, 2006b), on the other hand, thus far can access similar temperature and pressure conditions as well as those that are much more extreme. The conditions do not overlap completely, but such experiments can be problematic because they suffer from great uncertainties [e.g., likely far greater than the aforementioned ~1% required accuracy (Stevenson, 2010)].

While we have thus far discussed only planetary importance, another motivation for studying hydrogen and helium is simply to understand and predict the properties of the "simplest" elements of the periodic table. Even for hydrogen though, much is still unknown. The longest outstanding issue concerns a possible insulator-to-metal (IM) transition; the observation of metallic hydrogen being referred to as the "holy grail" of high-pressure research. Early predictions suggested that hydrogen would become atomic and transform to a simple metal at a pressure of 25 GPa (Wigner and Huntington, 1935). Although as experimental pressures steadily increased beyond 300 GPa, the IM transition has not yet been seen, at least not at or below room temperature. This discrepancy arises because early predictions were based on the assumption that metallic hydrogen would be a simple metal with nondirectional metallic bonding. Recent work suggests that this is not the case, and that hydrogen will go through a sequence of phase transitions, first in the molecular phase and then in the atomic phase. One can view either the

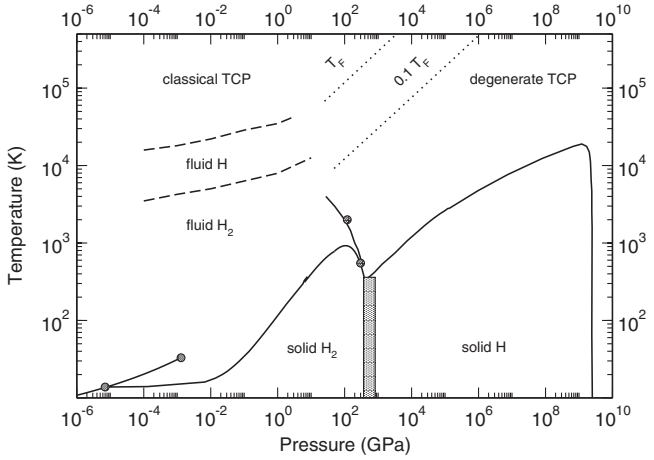


FIG. 2. Hydrogen phase diagram. Solid lines show the boundaries between the gas, liquid, and solid phases. The solid circles show the (approximate) location of critical or triple points. The dashed lines on the left estimate where fluid hydrogen changes from $H_2$ to H to a classical two-component plasma (TCP). The dotted lines at extreme temperatures estimate where the electrons become degenerate (i.e., the temperatures $T_F$ corresponding to the noninteracting Fermi energy $E_F$ and $0.1E_F$). The precise pressure mechanism by which hydrogen changes from solid $H_2$ to solid H is not well established, so it is shown as a shaded box. The line going vertically away from this shows the separation between the mostly insulating molecular fluid and the mostly conducting atomic fluid; the first-order LLT ends at a critical point, and what is shown at higher temperatures is a crossover. The almost vertical transition line at the extreme right indicates the quantum melting of the protons due to lattice compression.

IM transition as a change that occurs as one goes from molecules to atoms or simply as one that occurs directly in the molecular phase. Either is plausible, and according to Wigner's scaling argument (Wigner and Huntington, 1935) inevitable, but the question is which one is correct?

Figure 2 shows on an expanded scale the estimated physical regimes of hydrogen under discussion, as currently understood. It is seen that hydrogen transforms from a molecular crystal at low density to an atomic crystal at high density. Further, upon increasing temperature, it first melts, and then transforms into a plasma state.

While metallic hydrogen has not yet been observed in the low-temperature solid, metallization has been achieved in the fluid state in the range of 100–200 GPa and 2000–3000 K. But important questions regarding the characterization of this transition remain. For example, is it a first-order transition or a simple crossover? Landau and Zeldovich (1943) speculated that the IM transition at increasing density in liquid mercury would be a genuine phase transition. Since then, there has been recurring controversy concerning whether this transition in hydrogen, the so-called "plasma phase transition" (PPT), a second liquid-liquid transition (LLT) on the phase diagram, exists, and what its relation is to the molecular dissociation process. See Redmer and Holst (2010) for a recent overview. If the PPT exists at high enough temperatures, then there could be a surface inside the giant planets separating a conducting core from an insulating mantle. What is clear is that at least two different physical phenomena come together in the middle of the phase diagram caused by a combination of temperature and pressure, the IM and/or molecular-to-atomic transitions.

Perhaps even more interesting is that the zero-point motion (ZPM) of the protons in hydrogen can play an important role. At high pressures and as the temperature is lowered, the liquid will freeze. It has been suggested (Mon, Chester, and Ashcroft, 1980) that because of electronic screening, the effective proton-proton interaction is greatly reduced, and the liquid may remain stable. In fact, a large depression of the melting temperature is seen in other alkali metals, such as sodium and lithium. Further, if hydrogen is a liquid at sufficiently low temperatures, the effects of quantum statistics of the light protons could be important and lead to ordered quantum phases, such as those that occur in liquid $^3$He and $^4$He. Another possibility is that since electron-phonon coupling should be very large due to the bare Coulomb interaction as should ZPM, atomic hydrogen may be a room temperature superconductor (Ashcroft, 1968).

Another motivation for studying hydrogen, which is a major focus of this work, is to develop and test computer simulation methods. While hydrogen and helium are somewhat simpler than other elements, they pose unique difficulties. On the one hand, since they have no core electrons, their atomic structures are simple and the errors from the pseudopotential approximation, often employed to increase computational efficiency, are rather small or absent. Furthermore, relativistic effects are small, and hence spin orbit coupling can be ignored. On the other hand, because the protons, deuterons, and alpha particles that constitute the nuclei are so light, they too behave as quantum particles. This effect has such a strong influence that even the most basic properties of hydrogen are affected, such as relative stabilities of atomic structures (Natoli, Martin, and Ceperley, 1993). Unfortunately, simple approximations to account for ZPM do not always work. Thus, both electrons and ions should be treated using rigorous quantum mechanics in order to make definitive predictions. The availability of experimental data and the intense physical interest have made the study of high-pressure hydrogen and helium into test beds for theory and simulations. Considering that if the modern computational techniques, such as those based on density functional theory (DFT) and quantum Monte Carlo (QMC) calculations, are not accurate for hydrogen and helium, then there may be serious problems in trusting them for heavier elements.

There are even further motivations for studying dense hydrogen, such as technological applications, including inertial confinement fusion (ICF), where hydrogen gas is compressed with a laser-driven shock into the region where deuterium-tritium (D-T) fusion could occur. Such physical conditions are close to those of HD 209458b in Fig. 1. Such aspects will not be directly addressed in this review; the reader is instead referred to Lindl *et al.* (2004), for example.

This review concerns the thermodynamic properties of hydrogen and helium at pressures above 10 GPa and temperatures less than 100 000 K, focusing on advanced simulation methods and the comparison of their results with experiment. We start by describing the theoretical and numerical tools that are currently being used in Sec. II. We then provide a brief discussion of experimental techniques in

Sec. III, in order to facilitate the understanding of comparisons that follow. In Sec. IV, we describe the current understanding of the phase diagram of hydrogen under extreme conditions, as well as interesting predictions that have been made regarding it, such as metallization, superconductivity, and the possibility of a low- or zero-temperature quantum fluid. In Sec. V, we provide a discussion of helium as well as H-He mixtures important to planetary physics. Section VI concludes by discussing some of the open questions that remain.

## II. PREDICTING THE PROPERTIES OF MATTER UNDER EXTREME CONDITIONS

In this section, we review some of the computational methods to model hydrogen and helium at high pressures. Their properties, at the conditions of interest, are described to a high degree of accuracy by the nonrelativistic Hamiltonian for a collection of electrons and ions:

$$\begin{aligned}
&\hat{H} = \hat{T}_n + \hat{H}_{\rm el} = \hat{T} + \hat{V},\\
&\hat{H}_{\rm el} = \hat{T}_e + \hat{V}_{n-n} + \hat{V}_{e-e} + \hat{V}_{e-n}, \qquad \hat{T} = \hat{T}_n + \hat{T}_e,\\
&\hat{T}_n = \sum_{I=1}^{N_n} -\lambda_I \hat{\nabla}_I^2, \qquad \hat{T}_e = -\lambda_e \sum_{i=1}^{N_e} \hat{\nabla}_i^2,\\
&\hat{V} = \hat{V}_{n-n} + \hat{V}_{e-e} + \hat{V}_{e-n}, \qquad \hat{V}_{n-n} = \sum_{I<J} \frac{z_I z_J}{|\vec{R}_I - \vec{R}_J|},\\
&\hat{V}_{e-e} = \sum_{i<j} \frac{1}{|\vec{r}_i - \vec{r}_j|}, \qquad \hat{V}_{e-n} = -\sum_{i,I} \frac{z_I}{|\vec{r}_i - \vec{R}_I|},
\end{aligned} \tag{1}$$

where $N_n$ and $N_e$ are the number of ions and electrons, respectively, $\lambda_e = 1/2$, $\lambda_I = 1/(2M_I)$, and $M_I$ and $z_I$ are the mass and charge (in units of the electron mass $m_e$ and charge $e$) of the nucleus $I$.[1] Note that we implicitly assume charge neutrality of the system $\sum_I z_I = N_e$; hence, for hydrogen, the number of electrons is also $N_n$ and for helium it is $2N_n$. Note also that $\vec{r}$ with lower case indices $(i, j, \dots)$ is used to denote the position of electrons and $\vec{R}$ with upper case indices $(I, J, \dots)$ is used for the nuclei. When no indices are used, $\vec{r}$ and $\vec{R}$ represent the full $3N_e$ and $3N_n$ dimensional vectors. The electronic Hamiltonian $\hat{H}_{\rm el}$ corresponds to the solution of the problem in the clamped-nuclei approximation, where the ions produce a fixed external potential for the electrons. We always treat electrically neutral systems. Another quantity that is of interest is the electron number density given by $\rho$, and parametrized with $r_s = a/a_0$, where $4\pi a^3/3 = \rho^{-1}$. Given Eq. (1), we only need to add the temperature, particle statistics, and boundary conditions to completely specify the physical and numerical problem to be solved.

[1]In this section, we use atomic units, where Planck's constant $\hbar = m_e = k_B = e = 1$ with $k_B$ being Boltzmann's constant, and the energy is measured in Hartrees $E_{\rm h} = 315\,775$ K, $K = 27.2114$ eV. Note that, in these units, the energy of a hydrogen atom is $0.5E_{\rm h}$, the binding energy of a hydrogen molecule is $0.17E_{\rm h}$, the unit of length is the Bohr radius $a_0 = 0.0529$ nm, and the equilibrium bond length is $1.4a_0$.

Finding the eigenvalues and eigenfunctions of the Hamiltonian in Eq. (1) is a formidable task, impossible to do analytically except for the single hydrogen atom or the $H_2^+$ molecular ion. In practice, numerical or approximate theoretical methods must be used. Two of the most widely applicable methods are based on either imaginary-time path integrals or DFT, as discussed in the following sections. In what follows, we also briefly discuss semiempirical methods.

### A. The formalism of imaginary-time path integrals

Path integrals provide a theoretical and computational framework to discuss the many-body problem. The partition function of a quantum system at an inverse temperature $\beta = 1/k_B T$ is the trace of the many-body density matrix:

$$Z = \int d\vec{R} d\vec{r} \rho(\vec{R}, \vec{r}; \vec{R}, \vec{r}; \beta), \tag{2}$$

where $\rho(\vec{R}, \vec{r}; \vec{R}', \vec{r}'; \beta)$ is the density matrix in the position basis for the appropriate ensemble.[2] In the thermal ensemble, it has the form

$$\rho(\vec{R}, \vec{r}; \vec{R}', \vec{r}'; \beta) = \langle \vec{R}, \vec{r} | e^{-\beta \hat{H}} | \vec{R}', \vec{r}' \rangle. \tag{3}$$

The equilibrium average of an operator $\hat{O}$ can then be computed as

$$\begin{aligned}
\langle \hat{O} \rangle_\rho &= Z^{-1} \langle \hat{O}\, \hat{\rho} \rangle\\
&= Z^{-1} \int d\vec{R} d\vec{r} d\vec{R}' d\vec{r}' \rho(\vec{R}, \vec{r}; \vec{R}', \vec{r}'; \beta) \langle \vec{R}', \vec{r}' | \hat{O} | \vec{R}, \vec{r} \rangle.
\end{aligned} \tag{4}$$

The product property of the exponential of commuting operators,

$$e^{-(\beta_1+\beta_2)\hat{H}} = e^{-\beta_1 \hat{H}} e^{-\beta_2 \hat{H}}, \tag{5}$$

repeatedly applied, gives the path-integral expression for the partition function:

$$Z = \int \prod_{t=0}^{P-1} d\vec{R}^t d\vec{r}^t \langle \vec{R}^t, \vec{r}^t | e^{-\tau \hat{H}} | \vec{R}^{t+1}, \vec{r}^{t+1} \rangle, \tag{6}$$

where $\tau = \beta/P$ and periodic boundary conditions in the index $t$ applies: $\vec{R}_0 = \vec{R}_P$, $\vec{r}_0 = \vec{r}_P$. To account for Bose or Fermi statistics, a permutation of identical particles can also be applied, as we note below.

We define[3] the path as $\vec{\mathcal{R}} = \{\vec{R}^0, \vec{r}^0, \dots, \vec{R}^P, \vec{r}^P\}$; it consists of $3P(N_e + N_n)$ variables. This expression, exact for any value of $P$ (the number of time slices or beads), allows us to compute properties of a quantum system at inverse temperature $\beta$, using a density matrix evaluated at a smaller inverse temperature $\tau = \beta/P$. At small enough $\tau$, accurate and computationally simple approximations exist for the thermal density matrix which becomes exact as $\tau \to 0$. The best known example is the Trotter formula (Trotter, 1959):

[2]For simplicity, we limit our discussion to the canonical ensemble; it is straightforward to extend the discussion to other ensembles.

[3]Superscripts label imaginary-time indices, in order to avoid confusion.

$$e^{-\beta\hat{H}} = \lim_{P\to\infty} \prod_{P=0}^{P-1} e^{-\tau\hat{T}} e^{-\tau\hat{V}}; \tag{7}$$

one can ignore the commutator of the kinetic and potential operators in writing an integral expression for the density matrix at large $P$. Using the Trotter formula, the density matrix becomes (Feynman, 1972; Ceperley, 1992, 1996)

$$\rho(\vec{R}^0, \vec{r}^0; \vec{R}^0, \vec{r}^0; \beta) = \frac{1}{N!}\sum_{\mathcal{P}} (\pm 1)^{\mathcal{P}} \int_{\vec{R}^0 \to \mathcal{P}\vec{R}^0} d\vec{\mathcal{R}}\, e^{-S(\vec{\mathcal{R}})}, \tag{8}$$

where we included particle statistics (Bose or Fermi), by summing over permutations when the path is closed. $\mathcal{P}$ labels the permutation of the particles and $(\pm 1)^{\mathcal{P}}$ is its signature for bosons ( + ) or fermions ( − ). The "action" of the path $S(\vec{\mathcal{R}})$ (the logarithm of its probability density) is given (neglecting a constant term) by

$$S(\vec{\mathcal{R}}) = \int_0^\beta dt \left[ \frac{M_n}{2} \left| \frac{d\vec{R}(t)}{dt} \right|^2 + \frac{1}{2} \left| \frac{d\vec{r}(t)}{dt} \right|^2 + V(\vec{R}(t), \vec{r}(t)) \right] \tag{9}$$

$$\simeq \sum_{t=0}^{P-1} \left[ \frac{M_n |\vec{R}^t - \vec{R}^{t+1}|^2}{2\tau} + \frac{|\vec{r}^t - \vec{r}^{t+1}|^2}{2\tau} + \tau V(\vec{R}^t, \vec{r}^t) \right]. \tag{10}$$

Equation (9) represents the exact expression in the continuous path limit ($P \to \infty$, $\tau \to 0$, and $P\tau = \beta$). Note that to simplify the notation, above we considered a system with a single nuclear component of mass $M_n$; nuclei, being heavier, are represented by paths of much smaller size. For bosons (positive sign), or Boltzmannons (no sum over permutations), the integrand in Eq. (8) is positive, and the partition function becomes identical to the Boltzmann distribution of a classical system consisting of $(N_e \times N_n) \times P$ particles interacting with an effective classical "potential" $k_B T S(\mathcal{R})$.

The electronic integral can be formally performed, producing the influence functional $Z_{\rm el}[\vec{\mathcal{R}}_n]$:

$$\begin{aligned} Z &= \oint \mathcal{D}\vec{R} \oint \mathcal{D}\vec{r} \exp\left[ -\int_0^\beta dt [T_n(\vec{R}^t) + S_{\rm el}(\vec{R}^t, \vec{r}^t)] \right] \\ &= \oint \mathcal{D}\vec{R} \exp\left[ -\int_0^\beta dt T_n(\vec{R}^t) \right] Z_{\rm el}(\vec{\mathcal{R}}_n(t), [\vec{\mathcal{R}}_n]), \\ Z_{\rm el}(\vec{\mathcal{R}}_n(t), [\vec{\mathcal{R}}_n]) &= \oint \mathcal{D}\vec{r} \exp\left[ -\int_0^\beta dt S_{\rm el}(\vec{R}^t, \vec{r}^t) \right], \end{aligned} \tag{11}$$

where $\oint \mathcal{D}\vec{R}$ ( $\oint \mathcal{D}\vec{r}$) is a shorthand notation for the functional integral over all paths of length $\beta$, $\vec{\mathcal{R}}_n$ represents the nuclear coordinates of the path $\vec{\mathcal{R}}$, and the meanings of both $T_n$ (related to the nuclear kinetic energy operator in the Hamiltonian) and $S_{\rm el}$ should be clear from Eqs. (1) and (9). Equation (11) is just a formal manipulation of the partition function but it provides a useful framework to understand the Born-Oppenheimer (BO) approximation introduced below. Note that $Z_{\rm el}(\vec{\mathcal{R}}_n(t), [\vec{\mathcal{R}}_n])$ is a functional of the nuclear path $\vec{\mathcal{R}}_n$, a fact which becomes important below, as well as a function of imaginary time, through its explicit dependence on the nuclear path coordinates.

Equation (10) is the simplest approximation to the high-temperature density matrix, commonly employed in numerical calculations. In principle, any approximation correct to first order in imaginary time will give the same result as $\tau \to 0$. But for computational efficiency and stability for path-integral simulations, one can use improved actions, some of which include semiclassical expressions, higher order expansions (De Raedt and De Raedt, 1983; Takahashi and Imada, 1984), cumulant expansions (Ceperley, 1995), and pair-product actions (Barker, 1979; Ceperley, 1995). In most cases, improved actions lead to dramatic reductions in the numerical effort required to solve quantum problems. Of particular importance is the divergence in the potential as two charged particles approach one another.

Consider now the effect of incorporating the quantum statistics of the nuclei. The temperature $T_Q$ when quantum statistics becomes relevant can be estimated by setting the thermal de Broglie wavelength [proportional to $(k_B T_Q M_n)^{-1/2}$] to the average spacing between the ions given by $r_s$. One can show that for ideal fermions this corresponds to the Fermi energy up to a factor of the order of unity. For 3D protons we have $T_Q = (m_e/M_p) r_s^{-2} 5.84$ Ry $= 504$ K$/r_s^2$. At the metal-insulator transition ($r_s \simeq 1.4$), $T_Q \simeq 250$ K. In fact, the effects of quantum statistics for the protons are smaller than this estimate because the correlation between protons makes their exchange less probable than for noninteracting protons. Above the temperature $T_Q$ we can safely ignore the quantum statistics of the nuclei (Fermi-Dirac for hydrogen, Bose-Einstein for deuterium) and treat them as distinguishable particles.

To turn the path-integral expression into a numerical procedure, generalizations of classical simulation methods developed to perform high dimensional integrals and based on the Monte Carlo method are used. In the following sections, we describe the three main QMC methods that have been used to treat dense hydrogen and helium: path-integral Monte Carlo (MC) approaches for simulations at nonzero temperature; zero-temperature wavefunction-based approaches including variational, reptation, and diffusion Monte Carlo; and a method that explicitly separates electron and ionic degrees of freedom, the coupled electron-ion Monte Carlo (CEIMC). However, before discussing the numerical methods we discuss the BO approximation which is used in one of the quantum Monte Carlo methods to be discussed next, and in the first-principle molecular dynamics methods based on density functional theory which we review in some detail in Sec. II.E.

### B. The Born-Oppenheimer approximation

Electronic motion is much faster than that of the nuclei. The implications of the resulting separation in time scale were recognized in the early years of quantum mechanics, and led to the development of the BO approximation (Born and Oppenheimer, 1927). It is based on the fact that the proton is considerably heavier than the electron: $M_p/m_e \approx 1836$; all other nuclei are much heavier. Since the

velocity of electrons is much higher than that of ions, we can assume that electrons relax instantaneously and adiabatically to their equilibrium state as the ions move, neglecting any coupling between different electronic states, and also retardation effects in the electron-ion interaction. This leads to a partial decoupling of the electronic and ionic problems: the ions move in an effective potential defined by the solutions of the electronic Hamiltonian for fixed ionic positions.

In the BO approximation, the partition function can be expressed in path-integral notation (Feynman and Hibbs, 1965)

$$Z_{\mathrm{BO}} = \sum_q \oint \mathcal{D}\vec{R} \exp\left[ - \int_0^\beta dt[T_n(\vec{R}(t)) + E_q(\vec{R}(t))] \right], \tag{12}$$

where the sum is over a complete set of electronic states of $\hat{H}_{\mathrm{el}}$ for a fixed set of ionic positions with eigenvalues $E_q(\vec{R})$:

$$\hat{H}_{\mathrm{el}}(\vec{r}, \vec{R})\Phi_q(\vec{r}, \vec{R}) = E_q(\vec{R})\Phi_q(\vec{r}, \vec{R}). \tag{13}$$

If the temperature is low enough to neglect excited electronic states in Eq. (12), the standard form of the BO approximation is obtained, where the ions move in the potential energy surface defined by the electronic ground-state energy $E_0(\vec{R})$. For metals and systems at high temperatures, we must take into account the sum over electronic states. In that case, Eq. (12) requires a diagonalization of $\hat{H}_{\mathrm{el}}$ for every position of the ions, including all relevant electronic eigenstates. Following the work of Cao and Berne (1993), a simpler expression can be obtained by factorizing the exponential terms and performing the sum over electronic eigenstates, with the added complication that, in general, $T_n$ and $E_q$ do not commute. This leads to the following approximation to the partition function:

$$Z_{\mathrm{FEBO}} = \oint \mathcal{D}\vec{R} \exp\left[ - \int_0^\beta dt[T(\vec{R}) + F_{\mathrm{el}}(\vec{R}(t))] \right], \tag{14}$$

where we neglected terms of order $O(m_e/M_I)$; see Cao and Berne (1993) for additional details. Equation (14) is known as the free-energy Born-Oppenheimer (FEBO) approximation since the electronic free energy along the nuclear path $F_{\mathrm{el}}(\vec{R})$ at temperature $\beta$ appears. Note that in this approximation the influence functional has become a simple function of the nuclear path, losing the nonlocal (in imaginary time) dependence.

Equation (14) is the main result on this section; we managed to replace the potential energy operator with a local function of the ionic coordinates: the BO free-energy surface. By employing the BO approximation, we decoupled the problem into two parts, making a great simplification at the expense of a good approximation. The electronic problem has been completely encapsulated in the potential energy surface (PES) and can be solved with any suitable approximate method such as DFT or QMC. Once the PES has been defined, the ionic problem can be solved using path integrals for quantum ions or classical Monte Carlo or molecular dynamics for classical ions.

Note that the FEBO formulation provides a unifying framework to interpret several apparently different approximations routinely used in first-principle simulation methods. Consider thermodynamic conditions at which protons can be treated as classical particles. In the atomic phase, these conditions are realized for $T$ larger than $T_Q$ defined above. For example, at $r_s \simeq 1.4$, nuclear quantum effects are negligible for $T \gtrsim 1000$–$2000$ K. However, in the molecular phase, the bonding potential is much stronger than the intermolecular interaction and produces much larger quantum effects which results in a vibrational temperature of $\sim$6000 K in the isolated hydrogen molecule, and even higher values at finite density. However, the rotational temperature of a molecule is only $\sim$100 K. Therefore, in the molecular phase, quantum effects are important even at relatively high temperature, a fact often neglected in the applications. When nuclear quantum effects can be neglected, nuclear "imaginary-time paths" in Eq. (12) shrink to a single point and the electronic term appearing in the partition function is simply the exponential of the electronic free-energy function of the nuclear configuration. If, furthermore, thermal occupation of the electronic states can be neglected, the electronic free energy reduces to the ground-state electronic energy, and we recover the standard BO approximation. Conversely, if the temperature is low enough that neglecting thermal occupation of the electronic states is an accurate approximation, and nuclear quantum effects need to be taken into account, the sum over electronic states in Eq. (12) drops out and the action for the ionic paths depends only on the electronic ground-state PES. This is the BO approximation for quantum ions. Note that in the implementation of the numerical methods discussed below, in particular, in the DFT-based methods applied to metals, thermal occupation of the electronic states is necessary to ensure the stability of the self-consistent procedure. In view of our discussion, this fact seems to be more fundamental than simply a technical tool.

### C. Path-integral Monte Carlo approach

Path-integral methods for bosons and distinguishable particles are quite well developed (Ceperley, 1995) since there is no fermion minus sign. There are two main computational problems: choice of the action and sampling of the paths. As mentioned in Sec. II.A, there are several options for the path-integral action with varying degrees of efficiency and convergence properties. For hydrogen and helium, the optimal strategy has been the use of pair density matrices, where the two-body problem is solved exactly at very high temperature and the matrix squaring method is used to produce a density matrix at the desired temperature. Using the "pair action" instead of the bare potential reduces the number of time slices, and eliminates the instability that would otherwise occur in the primitive approximation to the path integral for the hydrogen atom caused by the potential going to $-\infty$ as an electron approaches a proton. The sampling of the paths is performed using a generalized Metropolis (Markov chain Monte Carlo) procedure. This is the only effective algorithm when the paths become very long, e.g., for electrons or at low temperatures. Special methods are used to change the permutation variables; see Ceperley (1995). As mentioned in Sec. II.B, as long as the temperature is high enough ($T > 100$ K for hydrogen in the metallization region,

$P \simeq 100$ GPa), nuclear exchange is irrelevant and only the identity permutation has a significant contribution to the partition function. In this case, ionic paths are isomorphic to ring polymers. When the path-integral representation is used for the ions and the electrons are treated with other methods (ground-state QMC or DFT), nuclear paths can also be sampled by molecular dynamics (MD); see Sec. II.E.5 for more details.

For electronic systems, it is possible to perform path-integral Monte Carlo (PIMC) simulations without invoking to the BO approximation. Both electrons and ions are represented in the path-integral expression, Eq. (8). Note that this is probably the only way to simulate directly electron-ion systems at finite temperature without approximations. In practice, the integration is complicated due to the cancellation of positive and negative contributions from the negative sign of the permutation, *the fermion sign problem*. The efficiency (inverse of computer time needed to reach a given precision) of treating this exactly scales as $\exp[-2\beta(F_F - F_B)]$, where $F_F - F_B$ is the free-energy difference between the Fermi and Bose systems; the exponent is extensive in the size of the system (Ceperley, 1996). Because of this, in the direct approach, one cannot treat systems where the number of electrons is large or the temperature is comparable with the Fermi energy.

However, it was shown (Ceperley, 1992, 1996) that one can evaluate the path integral by restricting the path to only positive contributions. One introduces a reference point $\vec{R}^*$ on the path that specifies the nodes of the fermion density matrix $\rho(\vec{R}, \vec{R}^*, t) = 0$ with respect to the reference point $\vec{R}^*$. A node-avoiding path for $0 < t \leq \beta$ never crosses a node: $\rho(\vec{R}(t), \vec{R}^*, t) \neq 0$. By restricting the integral to these paths,

$$\rho_F(\vec{R}_\beta, \vec{R}^*; \beta) = \int d\vec{R}_0 \rho_F(\vec{R}_0, \vec{R}^*; 0) \times \oint_{\vec{R}_0 \to \vec{R}_\beta \in \Upsilon(\vec{R}^*)} d\vec{R}_t e^{-S[\vec{R}_t]} \tag{15}$$

[$\Upsilon(\vec{R}^*)$ denotes the restriction] the contributions to the partition function are strictly positive. This, therefore represents, in principle, a solution to the sign problem, but only if the exact fermionic density matrix is used for the restriction. In practice, one must approximate the density matrix. The simplest approximation is to use a determinant of single particle density matrices:

$$\rho(\vec{R}, \vec{R}'; \beta) = \begin{vmatrix} \rho_1(\vec{r}_1, \vec{r}'_1; \beta) & \cdots & \rho_1(\vec{r}_N, \vec{r}'_1; \beta) \\ \cdots & \cdots & \cdots \\ \rho_1(\vec{r}_1, \vec{r}'_N; \beta) & \cdots & \rho_1(\vec{r}_N, \vec{r}'_N; \beta) \end{vmatrix}. \tag{16}$$

It can be shown that for temperatures larger than the Fermi energy, the interacting nodal surface approaches the free-particle (FP) nodal surface, i.e., the nodes of the determinant in Eq. (16) when FP single particle density matrices are used

$$\rho_1(\vec{r}, \vec{r}', \beta) = (2\pi\beta)^{-3/2} \exp\{-(\vec{r} - \vec{r}')^2/2\beta\}. \tag{17}$$

At low density, exchange effects are unimportant, for example, in the molecular phase, when electrons are localized in a molecule in a nodeless spin singlet state. However, in general, at temperatures much less than the Fermi energy, interactions could have a significant effect on the nodal surfaces and hence on which paths are allowed. Several methods have been developed to go beyond the FP restriction. Militzer and Ceperley (2000) used the nodal surface of a density matrix derived from a variational principle that includes interparticle interactions and electronic bound states. Also recently Khairallah, Shumway, and Draeger (2011) implemented a modified nodal restriction, the so-called antinodal-slice constraint. This method has the advantage of eliminating the reference point and thereby allowing the paths to be much more easily sampled than those that have a reference point; however, it introduces a systematic approximation which does not become exact even if exact nodes would be employed. Note that in these methods, the trial density matrix is used only to determine the nodal constraint; the complete potential is taken into account in the path-integral action (Ceperley, 1995). Although the PIMC fermion methods have not been extensively used, they show great promise for the study of more complex materials at high temperature [see, for instance, a recent application to water and carbon by Driver and Militzer (2012)].

An alternative simulation method based on path integrals for electron-ion systems, called the direct path-integral Monte Carlo (DPIMC) method, has been developed over the last decade by Filinov *et al.* (2005). At variance with the restricted PIMC (RPIMC), Fermi statistics for electrons is accounted by inserting a Slater determinant of single particle propagators in the last link of the electronic paths. The sampling of the fermionic loops is based on the absolute value of the determinant and the sign of the determinant is used for the estimator. This method is adequate in the semiclassical regime where the effect of Fermi statistics is marginal. However, it has a sign problem which will become more and more serious when approaching the quantum regime. For a given Hamiltonian, the probable phase space for fermions is very different from that of bosons; sampling by a bosonic density matrix will produce paths irrelevant for the fermions. This might be at the origin of formation of large density inhomogeneities observed by this method when lowering the temperature (Filinov *et al.*, 2003). Moreover, the systematic effect of finite imaginary-time step seems to not have been considered adequately in the original publications (Filinov *et al.*, 2005).

### D. QMC-based first-principles simulations

Once the BO approximation is employed, the electronic calculation can be solved with any appropriate electronic structure method. The most common approach is to use density functional theory; this leads to methods typically known as *ab initio* molecular dynamics or first-principles molecular dynamics. Section II.E gives a detailed description of DFT-based approaches. A more advanced approach consists of using QMC methods to solve the electronic problem. QMC, although more accurate than DFT in general, is also more expensive. As a consequence, only a small number of first-principles studies using QMC have been reported in the literature, all of them on high-pressure hydrogen and helium (Ceperley, Dewing, and Pierleoni, 2002; Pierleoni, Ceperley,

and Holzmann, 2004; Pierleoni and Ceperley, 2005; Delaney, Pierleoni, and Ceperley, 2006; Pierleoni and Ceperley, 2006; Attaccalite and Sorella, 2008; Pierleoni *et al.*, 2008; Morales, Pierleoni, and Ceperley, 2010a). This should be compared with the thousands of DFT-based FP simulations published so far (Marx and Hutter, 2000). In the framework of QMC-based simulations at nonzero temperature, only two approaches have been tried. In the CEIMC method, discussed below, QMC methods are used to calculate energy differences during a Metropolis MC simulation of the nuclei. This method was recently used to study the equation of state and the liquid-liquid transition in hydrogen (Morales *et al.*, 2010b); it has also been used to study hydrogen-helium mixtures (Morales, 2009) and to perform free-energy calculations (Morales, 2009; Morales, Pierleoni, and Ceperley, 2010a; Liberatore *et al.*, 2011). An alternative MD approach based on a "noisy" Langevin dynamics scheme, with ionic forces from QMC, has also been developed (Attaccalite and Sorella, 2008) and applied to high-pressure hydrogen.

Before discussing QMC-based first-principle methods to simulate finite-temperature systems, we provide a detailed description of ground-state QMC methods. These methods can be either used to obtain accurate solutions of the ground-state electronic problem in the finite-temperature QMC-based FP methods in the framework of the BO approximation or can be used, without resorting to the BO approximation, to obtain accurate solutions for electron-ion systems in their ground state.

### 1. Ground-state quantum Monte Carlo methods

Ground-state QMC methods were the first calculations that applied quantum simulation techniques to a many-body crystal including both the electronic and ionic degrees of freedom (Ceperley and Alder, 1981, 1987). The ultimate goal of QMC is to provide an exact stochastic solution to the Schrödinger equation, similar to the way Monte Carlo methods can be used to solve classical many-body problems. In practice, approximations must be used to treat fermions. The main advantage of QMC over alternative methods for electronic structure calculations is the balance that it provides between accuracy and computational cost. Currently, QMC can provide results that are more accurate than DFT for about an order of magnitude additional computational cost and QMC scales approximately as $N^2$ to $N^3$ with the number of electrons. Traditional chemistry methods, while providing a higher degree of accuracy in general, have an unfavorable scaling and as a consequence can be applied only to few electron systems. QMC, on the other hand, can be applied to systems with up to several thousand electrons with currently available computational resources.

#### *a. Variational Monte Carlo methods*

The simplest quantum simulation, variational Monte Carlo (VMC), was first introduced by McMillan (1965) for liquid helium (modeled as a single composite particle) and generalized to fermions by Ceperley, Chester, and Kalos (1977). VMC allows us to optimize the trial function needed in the projector methods, described below. Let $\psi_T(\vec{R})$ be an assumed trial function with adjustable parameters $\{a\}$. Using the Metropolis Monte Carlo technique (Metropolis *et al.*, 1953), one samples the un-normalized distribution $|\psi_T(\vec{R})|^2$ and calculates an upper bound to the ground-state energy,

$$E \le E_V(a) = \frac{\int d\vec{R}\Psi_T^*(\vec{R})\hat{H}\Psi_T(\vec{R})}{\int d\vec{R}\Psi_T^*(\vec{R})\Psi_T(\vec{R})} = \frac{\int d\vec{R}|\Psi_T(\vec{R})|^2 E_L(\vec{R})}{\int d\vec{R}|\Psi_T(\vec{R})|^2}. \tag{18}$$

The fluctuations in the energy estimator, the local energy $E_L(\vec{R}) = [\hat{H}\Psi_T]/\Psi_T$, are entirely due to inaccuracies of the trial function: as the trial wave function approaches the exact eigenfunction, the fluctuations, which control how quickly the energy converges, decrease to zero. At the same time, the estimate converges to the exact energy.

#### *b. The trial function*

The strategy in VMC is to pick a form for the trial wave function that incorporates as many properties of the exact many-body wave function as possible, while maintaining enough flexibility to allow for its efficient optimization. The pair-product trial wave function is the simplest extension of the Slater determinant of single particle orbitals used in mean field treatment of electronic systems:

$$\Psi_{SJ}(\vec{r}|\vec{R}) = \exp\left(-\sum_{i<j} u(r_{ij})\right) \det[\phi_k(\vec{r}_i, \sigma_i|\vec{R})], \tag{19}$$

where $\phi_k(\vec{r}, \sigma|\vec{R})$ is the $k$th spin orbital for a given configuration of the protons. The term $u(r_{ij})$, the (Jastrow) correlation factor, introduces two-body correlations into the many-body wave function. It is symmetric under particle exchange; antisymmetry is given by the determinant only. In the above trial function, we assumed that the Jastrow factor $u(r)$ depends only on the distance between two electrons; more generally it can also depend on the positions of the nuclei and their spin states. Often either or both of $\phi_k$ and $u$ are derived from an approximate theory such as the random-phase approximation (for $u$) or DFT (for $\phi$).

The spin orbitals are quite important because they provide the nodal structure of the trial function crucial in the fixed-node approximation described below. The choice of orbitals for hydrogen has evolved over the years. The first QMC calculation of metallic hydrogen (Ceperley and Alder, 1981, 1987) used plane waves $\phi_{\vec{k}}(\vec{r}, \sigma) = \exp[i\vec{k}\cdot\vec{r}]$. Although they are qualitatively correct in the metallic phase, since the electron-proton "cusp" can be taken into account in the correlation factor $u(r)$, quantitatively accurate results require better orbitals that include information about the positions of the ions.

The next step in development came from the work of Wang *et al.* (1990) and Natoli, Martin, and Ceperley (1993, 1995), where orbitals obtained from band-structure calculations were employed. Natoli and Ceperley (1995) established the fact that energies from plane-wave determinants in metallic hydrogen are higher than the values using DFT-LDA (local density approximation) orbitals by 0.05 eV/atom at the density at which the transition between molecular and metallic hydrogen is expected ($r_s = 1.31$).

Turning now to the correlation factors $u(r_{ij})$, optimal factors will obey the cusp condition at short distances

$$\left.\frac{du_{ij}}{dr}\right|_0 = -\alpha_{ij}, \tag{20}$$

where $\alpha_{ij} = 1/2$ if $i$ and $j$ have antiparallel spins, otherwise $\alpha_{ij} = 1/4$. Within the random-phase approximation (RPA) and neglecting antisymmetry, the correlation factors for the charged particles have the Fourier transforms

$$u_k = -\frac{1}{2} + \sqrt{1 + \frac{12r_s}{k^4}}. \tag{21}$$

This form has the exact behavior at both small and large distances for a metallic system. It is important to reproduce the correct $1/r$ behavior at large distances since that controls the dielectric properties. In practice, these RPA functions are typically augmented with flexible forms that preserve the asymptotic behaviors, e.g., Gaussians, but contain free parameters which can be tuned to improve the trial function.

The first corrections to the pair-product trial function are a three-body correlation term which modifies the correlation part of the trial function (Jastrow) and a "backflow" transformation which changes the orbitals and therefore the nodal structure (or the phase) of the trial function (Kwon, Ceperley, and Martin, 1993; Holzmann *et al.*, 2003; Pierleoni *et al.*, 2008). This transformation introduces correlation effects into the Slater determinant; the energy and the nodal surfaces of the trial function are improved. The modified trial function has the form

$$\Psi_T(\vec{r}|\vec{R}) = \det[\phi_k(\vec{x}_i, \sigma_i)]e^{-U_2-U_3}, \tag{22}$$

where $U_2 = \sum_{i<j} \tilde{u}(r_{ij})$ is the two-body correlation factor discussed previously [the˜indicates that it can differ from the original one, see Holzmann *et al.* (2003) for details], $U_3$ is a three-body term of the form

$$U_3 = -\sum_{i=1}^{N_e}\left[\sum_{j=1}^{N} \xi(r_{ij})\vec{r}_{ij}\right]^2, \tag{23}$$

and finally the "quasiparticle" coordinates appearing in the plane wave orbitals are given by

$$\vec{x}_i = \vec{r}_i + \sum_{j=1}^{N} \eta(r_{ij})\vec{r}_{ij} \qquad (i = 1, \ldots, N_e). \tag{24}$$

The RPA approximation was used (Holzmann *et al.*, 2003) to provide a general form for the functions $\xi(r)$, $\eta(r)$ in Eqs. (23) and (24), satisfying the correct limiting behavior at small and large distances. These functions can also be augmented with flexible functional forms and optimized with VMC.

As discussed, the trial wave function generally has variational parameters that need to be optimized at the VMC level. The optimization not only improves the quality of the final results in projector Monte Carlo methods, but also improves the efficiency of QMC calculations, which is directly related to the error of the trial wave function. Optimization methods in QMC have a long history (Umrigar, Wilson, and Wilkins, 1988; Drummond and Needs, 2005; Toulouse and Umrigar, 2007), with methods ranging from variance minimization and energy optimization to a combination of both. They received considerable attention over the last decade leading to the development of fairly robust and efficient approaches, such as the linear method of Umrigar *et al.* (2007), which are capable not only of optimizing all the parameters in the wave function, but also of handling extremely flexible wave functions with thousands of variational parameters (Attaccalite and Sorella, 2008; Clark *et al.*, 2011). Several forms of trial wave functions beyond the Slater-Jastrow backflow have been explored in recent years with some success, including Pfaffians (Bajdich *et al.*, 2006) and correlated geminals (Casula, Attaccalite, and Sorella, 2004).

### c. Projector Monte Carlo methods

We now describe how to go beyond VMC by applying a function of the Hamiltonian to project out the ground state. Because the diffusion Monte Carlo (DMC) method has been extensively reviewed elsewhere [see, e.g., Foulkes *et al.* (2001)], here we discuss a more recent technique, ground-state path-integral Monte Carlo (GSPI), also known as reptation quantum Monte Carlo (RQMC). We define the following quantity, formally similar to a partition function:

$$Z(t) = \langle\Psi_T|e^{-t\hat{H}}|\Psi_T\rangle = \langle\Psi_T(t/2)|\Psi_T(t/2)\rangle. \tag{25}$$

Here the projection time $t$ plays the role of the inverse temperature. The variational energy of $\Psi_T(t/2)$ at time $t$ is the derivative of the logarithm of $Z(t)$:

$$E(t) = -\frac{\partial}{\partial t}\ln Z(t) = \frac{\langle\Psi(t/2)|\hat{H}|\Psi(t/2)\rangle}{\langle\Psi(t/2)|\Psi(t/2)\rangle} \tag{26}$$

and the "variance" of $\Psi_T(t/2)$ given as

$$\sigma_E^2(t) = -\frac{\partial}{\partial t}E(t) = \langle[\hat{H} - E(t)]^2\rangle \geq 0, \tag{27}$$

is non-negative implying that the energy decreases monotonically with time. The exact ground state is reached at large time

$$\lim_{t\to\infty} E(t) = E_0, \tag{28}$$

$$\lim_{t\to\infty} \sigma^2(t) = 0, \tag{29}$$

as long as the trial wave function has a nonzero overlap with the ground-state wave function. Writing $Z(t)$ in coordinate space

$$Z(t) = \int d\vec{r}_1 d\vec{r}_2 \Psi_T^*(\vec{r}_1)\rho(\vec{r}_1, \vec{r}_2, t)\Psi_T(\vec{r}_2), \tag{30}$$

where $\rho(\vec{r}_1, \vec{r}_2, t) = \langle\vec{r}_1|\exp(-t\hat{H})|\vec{r}_2\rangle$ is the many-body thermal density matrix in coordinate space.

Thus, in order to compute any average over the ground state we need to know the thermal density matrix at large enough projection time. As we did earlier with path integrals, this is accomplished by breaking the projection into many small steps $\exp(-tH) = \exp(-\tau H)^n$, writing an explicit form for $\exp(-\tau H)$ and performing the needed integrals with Monte Carlo methods. The difference with PIMC is in the boundary conditions of the paths; instead of the paths closing on themselves, the paths are open and projected onto

a trial function at both ends. If the trial wave function $\Psi_T$ is accurate, GSPI computationally is a much more efficient way of computing ground-state properties than is PIMC.

As usual, the main difficulty is the fermion sign problem. For electrons, the trial wave function must be antisymmetric if two electrons with the same spin are exchanged. In general, the trial function is complexed valued. Hence the integrand of Eq. (30) is not necessarily positive. One could carry along the phases of the trial functions at the two ends as part of the calculated average, however, this becomes statistically very noisy and thus inefficient at large projection time and for many electrons. This is the "sign problem" for projector Monte Carlo methods. The solution to this problem is the fixed-node (for real $\Psi_T$) or fixed-phase (for complex $\Psi_T$) approximation: one requires that the unknown solution have the same phase as the trial function (Pierleoni and Ceperley, 2006). The resulting solutions, although approximate and dependent on the quality of the nodes of the trial wave function, are typically very good. The efficiency of the method is also reasonable for many-particle systems. The approximate results give an upper bound to the exact energy, the best upper bound with the assumed phase, and hence, the exact result if the assumed phase (or nodes) is exact.

The main advantage of GSPI is the fact that observables other than the energy are readily available from the simulation, as opposed to other projector methods such as DMC where further work is needed to obtain most observables. A crucial aspect of the GSPI method is the way the paths are sampled; sampling can become extremely inefficient. An important step forward was made with the development of the bounce algorithm (Pierleoni and Ceperley, 2005, 2006) which, with respect to the standard reptation algorithm previously used, allows for the efficient exploration of phase space, and significantly reduces the probability of obtaining persistent configurations.

### 2. Coupled electron-ion Monte Carlo method

The CEIMC method is based on the BO approximation. The nuclei are treated at finite temperature $T$, using a Metropolis MC algorithm and the electrons are treated at zero temperature using a ground-state QMC method. The method can be applied to both classical and quantum ions in the path-integral representation, by sampling the ionic paths from the appropriate distributions (Pierleoni, Ceperley, and Holzmann, 2004; Pierleoni and Ceperley, 2006). The acceptance probability in the Metropolis method is given by

$$A(\vec{R} \rightarrow \vec{R}') = \min[1, \exp(-\beta \Delta E_{\mathrm{BO}})], \tag{31}$$

where $\vec{R}$ represent here the set of nuclear coordinates. For simplicity, we assume a uniform *a priori* transition matrix and $\Delta E_{\mathrm{BO}} = E_{\mathrm{BO}}(\vec{R}') - E_{\mathrm{BO}}(\vec{R})$ is the difference in BO energy between nuclear states $\vec{R}$ and $\vec{R}'$. In the case of quantum ions, $\Delta E_{\mathrm{BO}}$ is the change in the action of the associated classical system; see Eq. (10). In CEIMC, the estimate of $\Delta E_{\mathrm{BO}}$ for a given trial function is computed by QMC and is therefore affected by statistical noise, which, if ignored, will bias the Metropolis random walk. Since the noise in the energy difference decreases with the number of Monte Carlo steps as $1/\sqrt{N}$, reducing the noise level by direct simulation to the point where the bias is negligible is time consuming. To solve this problem the penalty method is used (Ceperley and Dewing, 1999).

The basic idea of the penalty method is to relax the requirement of detailed balance for every step in the simulation and instead require detailed balance to hold only when we average over the noise distribution. Consider two ionic states $(\vec{R}, \vec{R}')$ and call $\delta(\vec{R}, \vec{R}')$ the "instantaneous" energy difference multiplied by $\beta = (k_B T)^{-1}$. Further assume that the average and the variance of $\delta(\vec{R}, \vec{R}')$ over the noise distribution $P(\delta|\vec{R} \rightarrow \vec{R}')$ exist: Since the noise is normally distributed because of the central limit theorem [assuming the variance of $\delta(\vec{R}, \vec{R}')$ is finite] (Feller, 1968), it can be shown (Ceperley and Dewing, 1999) that accepting the moves according to

$$a(\delta, \chi^2, n) = \min\left[1, \exp(-\delta - u_B)\right] \tag{32}$$

will lead to an exact sampling of the Boltzmann distribution even with noise. Here $u_B$ is a correction because the variance is also estimated from the data:

$$u_B = \frac{\chi^2}{2} + \frac{\chi^4}{4(n+1)} + \frac{\chi^6}{3(n+1)(n+3)} + \cdots, \tag{33}$$

where $\chi^2 = [1/n(n-1)] \sum_{i=1}^{n} (y_i - \delta)^2$ is an estimate of the variance of the energy difference from the sample data, and $n$ is the number of statistically uncorrelated estimates of $\delta(\vec{R}, \vec{R}')$. We also require that $\chi^2/n \leq 1/4$ for the asymptotic expansion in Eq. (33) to converge.

Equation (32) is similar to the standard Metropolis acceptance/rejection rule, with an extra rejection term $u_B(>0)$ which is related to the level of noise in the electronic energy difference between the two protonic configurations $R$ and $R'$. Since we only need to compute an energy difference from QMC, we can use a correlated sampling, a much more efficient method than performing two independent calculations (Ceperley, Dewing, and Pierleoni, 2002). The efficiency of the method is sensitive to the noise level; it depends on the size of the ionic steps and on the length of the sampling of the electronic configuration space. If the noise level is too low (because either we move ions very little or we run very long electronic calculations), the extra rejections are significantly reduced but the computer time required will be very large. On the other hand, if the noise level is too high, all moves will be rejected from the penalty term. The optimal noise level depends on the temperature and is well approximated by $\chi^2 \approx 1$.

One could get the impression that the penalty method causes a large decrease in the efficiency of CEIMC when decreasing the temperature, since the noise level in the energy would need to be at least as low as the temperature. However, at low temperatures, the nuclei need to be represented by their own path integrals and the relevant "temperature" is now the inverse of the imaginary-time step $\tau$, rather then the inverse physical temperature $\beta$, and the optimal noise level is $\tau\sigma = 1$, where $\sigma$ is now the noise on the energy difference at each time slice of the nuclear path. For a more detailed discussion on the implementation of nuclear path integrals in CEIMC, see Pierleoni and Ceperley (2006).

We can improve the efficiency of the CEIMC method by using a multilevel sampling approach. Trial ionic moves are

"screened" by first accepting or rejecting them using a simple effective potential $V_{\rm eff}(\vec{R})$:

$$A_1(\vec{R} \rightarrow \vec{R}') = \min\{1, \exp[-\beta \Delta V_{\rm eff}]\}, \tag{34}$$

where $\Delta V_{\rm eff} = V_{\rm eff}(\vec{R}') - V_{\rm eff}(\vec{R})$. If the move is accepted, the energy difference is calculated using QMC and the step accepted or rejected based on

$$A_2(\vec{R} \rightarrow \vec{R}') = \min\{1, \exp[-(\Delta - \beta \Delta V_{\rm eff}) - u_B]\}. \tag{35}$$

Since the evaluation of the effective potential is orders of magnitude faster than the evaluation of the QMC energy difference, the overhead produced by the prerejection is negligible. On the other hand, it can significantly increase the efficiency of the method by eliminating QMC calculations for "bad" steps and increasing the effective acceptance rate.

Another promising approach for QMC-based FP simulations is that of Attaccalite and Sorella (2008). In this approach, Langevin dynamics is used to perform a simulation with forces coming from QMC calculations. Similar to CEIMC, the forces contain a statistical uncertainty that will lead to a biased ionic sampling if used in Newtonian dynamics. Instead, they use a modified Langevin algorithm, robust to noise. They show that it is possible to add Gaussian correlated noise to the QMC forces, as long as the covariant matrix of the forces is finite and known. With this method, they are able to simulate liquid hydrogen close to the dissociation transition and predict a stable molecular liquid at room temperature at 300 GPa. While this calculation used VMC forces and did not include twist average boundary conditions (see the discussion on size effects below), the method shows great promise as a general purpose QMC-based first-principle method for arbitrary chemical systems. Along with CEIMC, this method represents one of the frontiers in the development of next-generation (beyond DFT) first-principles simulation methods.[4]

### E. DFT-based first-principles simulations

Almost all first-principles simulation methods using a DFT energy surface are performed with MD, although attempts have been reported using Monte Carlo methods (McGrath *et al.*, 2006). There are two general ways to use potential energy surfaces from DFT in a MD simulation: either a fully converged calculation for the electrons is performed for every nuclear position or a unified dynamical approach is used to propagate both electrons and ions simultaneously. Both approaches are described below. Before describing the solution of the ionic problem, we give a brief description of DFT methods, which form the basis of the first-principles molecular dynamics (FPMD) approach. For a more detailed discussion of DFT and FPMD methods, see Parr and Weitao (1994), Fiolhais, Nogueira, and Marques (2003), Martin (2004), Dykstra (2005), Mattsson *et al.* (2005), Hafner (2008), and Marx and Hutter (2009).

[4]Note that in what is called quantum molecular dynamics in the literature, classical dynamics of the ions is performed with forces computed with density functional theory.

#### 1. Density functional theory

Although theories based on functionals of the electron density have a long history in physics and chemistry, with the Thomas-Fermi theory as one of the earliest and better known examples (Fermi, 1927; Thomas, 1927), the term density functional theory (Parr and Weitao, 1994; Martin, 2004; Kohanoff, 2006) refers to the formulation based on Hohenberg-Kohn (HK) theorems (Hohenberg and Kohn, 1964) and the Kohn-Sham (KS) ansatz (Kohn and Sham, 1965).[5] The first HK theorem states that there is a one-to-one correspondence between the external potential (in this case the potential produced by the nuclei) and the ground-state electronic density. This means that for every wave function that is the ground state of some Hamiltonian, the external potential giving rise to it is unique up to an additive constant. Notice that while the wave function for the many electron system lives in a $3N_e$ dimensional space, the electron density is a function of only the three spatial coordinates. Thus, in principle, knowledge of the density implies knowledge of the wave function and, in turn, of all the properties of the system. The second HK theorem states that there exists a universal energy functional of the density $E[n]$ defined for any external potential, such that the global minima of this functional represents the ground-state energy of the system. The density at the minimum gives the ground-state electronic density.

One might hope that the HK theorems could simplify the description of the many electron problem since it uses the density rather than the full wave function as the fundamental variable, but, in practice, the universal energy functional is unknown and there is currently no known accurate way of extracting properties of electronic systems from the density alone. The approach of Kohn and Sham (1965) was to replace the original interacting problem by an auxiliary system defined in terms of noninteracting electrons that is more tractable and easier to solve. In their formulation of DFT, which is the implementation commonly used today, the auxiliary system is defined such that its ground-state electron density is the same as the density of the interacting system. This allows us to write down an explicit form for the energy functional in terms of the single-body orbitals of the noninteracting system:

$$\begin{aligned} E_{\rm KS}[n] &= -\frac{1}{2}\sum_{i=1}^{N} |\vec{\nabla}\psi_i(\vec{r})|^2 + \int d^3\vec{r} n(\vec{r}) V_{\rm ext}(\vec{r}) \\ &\quad + E_H[n] + E_{nn} + E_{\rm xc}[n], \\ E_H[n] &= \frac{1}{2}\int d^3\vec{r} d^3\vec{r}' \frac{n(\vec{r}) n(\vec{r}')}{|\vec{r} - \vec{r}'|}, \end{aligned} \tag{36}$$

where $\psi_i(\vec{r})$ are the eigenstates of the noninteracting Hamiltonian, $E_H$ is the Hartree energy (the classical electrostatic interaction of the density), $E_{nn}$ is the nuclei-nuclei interaction energy, and $E_{\rm xc}$ accounts for exchange and correlation energy. The density of the noninteracting system is defined by $n(\vec{r}) = \sum_{i=1}^{N} |\psi_i(\vec{r})|^2$.

[5]We do not describe earlier band theory methods on hydrogen since those methods have been generally superseded by DFT.

In the KS formulation all the many-body effects are encapsulated in the exchange-correlation functional $E_{xc}[n]$, which accounts not only for exchange and correlation effects, but also for many-body corrections to the kinetic energy. Although the existence and uniqueness of this functional are guaranteed by the HK theorem, its form is unknown and probably too complicated to be computed exactly. Nonetheless, it is much easier to find reasonable approximations for $E_{xc}$ since this term typically represents a small contribution to the total energy.

The ground-state HK theorems were extended to finite temperature by Mermin (1965). Although the study of the finite-temperature functional has not received as much attention over the years, its independent particle formulation is used frequently in FPMD with a form $F_{KS}[n] = E_{KS}[n] - TS[n]$, where $E_{KS}[n]$ is the usual KS energy functional. The density is a weighted average over excited states $n(\vec{r}) = \sum_{i=1}^{\infty} f_i |\psi_i(\vec{r})|^2$, $f_i$ defines the occupation of state $i$ (e.g., using the Fermi-Dirac formula) and the entropy has the form

$$S = -\sum_i f_i \log f_i + \sum_i (1 - f_i)\log(1 - f_i). \tag{37}$$

The free-energy functional plays a crucial role in the study of metals and is the basis of the FEBO method discussed above. It is found that using a small but finite temperature often leads to much faster and robust convergence for certain systems at low temperatures.

The accuracy of DFT depends on the exchange-correlation functional. The simplest possible form, known as the LDA, assumes that the functional is a local function of the density

$$E_{xc}^{LDA} = \int d^3\vec{r}\,\epsilon_{xc}(n(\vec{r}))n(\vec{r}), \tag{38}$$

where $\epsilon_{xc}(n)$ is the exchange-correlation energy density of the homogeneous electron gas with density $n$, calculated using QMC methods by Ceperley and Alder (1980) and subsequently parametrized by Perdew and Zunger (1981) and others. While the LDA generally produces reasonable results, in particular, for weakly inhomogeneous systems, current calculations typically include information about the density variation, producing better approximations. In the next level of accuracy, the generalized gradient approximation (GGA), a semilocal expansion of the exchange-correlation density, is used including also the density gradient, typically expressed in terms of the dimensionless combination $s = |\vec{\nabla} n|/(2k_F n)$. There are various implementations of GGA functionals, e.g., variational forms fitted to reproduce experimental results in molecular systems and condensed phases, and implementations based on perturbation treatments. The Perdew-Burke-Ernzerhof (PBE) (Perdew, Burke, and Ernzerhof, 1996) exchange-correlation functional is the most used choice for dense hydrogen, and, as we show, produces a good description at high pressure.

Beyond the GGA approximation, in the metaGGA formulation (Perdew and Schmidt, 2001) the noninteracting kinetic energy density $\tau(\vec{r}) = \frac{1}{2}\sum_i |\vec{\nabla}\psi_i(\vec{r})|^2$ is used in the construction of the exchange-correlation energy density. In the orbital dependent formulations (Kümmel and Kronik, 2008), the Kohn-Sham orbitals are used in the construction of the exchange-correlation functional. In this case, a generalized KS formulation must be used because the resulting potential becomes orbital dependent; this invalidates the original formulation by HK. Nonetheless, the use of orbitals still allows for a rigorous formulation of DFT and, in general, produces a large increase in accuracy and has become the standard for quantum chemistry calculations. The best example of orbital dependent DFT is the hybrid functional approach, where the exchange-correlation functional includes a fraction of exact exchange from Hartree-Fock theory (Becke, 1993). The best known hybrid functionals in the condensed matter community are PBE0 (Perdew, Ernzerhof, and Burke, 1996), which uses a mixture of 25% of Hartree-Fock exchange with 75% PBE, and the HSE (Heyd, Scuseria, and Ernzerhof, 2003) functional, which uses a combination of range separation and the same mixing fractions as in PBE0; the Hartree-Fock calculation is done only on the short-range part of the potential.

The KS band gap differs from the true one by a discontinuity in the derivative of the exchange-correlation potential $\nabla_{xc}$ (Perdew and Levy, 1983) with respect to density. Since $\nabla_{xc} = 0$ for standard DFs, the width of the gap at a given density (pressure) as well as the density at which it actually closes are both underestimated (Johnson and Ashcroft, 2000; Städele and Martin, 2000). However, the exact-exchange method (Städele *et al.*, 1997, 1999) provides an approximation to $\nabla_{xc} = 0$; the resulting nonlocality in exchange causes an overestimation of the width of the gap. One can partially cancel these errors by mixing a fraction of exact exchange with a standard DF, such as is done by Heyd, Scuseria, and Ernzerhof (2003): relatively accurate band gaps are obtained (Brothers *et al.*, 2008). Exact-exchange functionals, e.g., HSE, require significantly more computational effort compared to a standard DF. An alternative to hybrid functionals are many-body Green's function techniques, e.g., the *GW* approximation (Onida, Reining, and Rubio, 2002; Fiolhais, Nogueira, and Marques, 2003), which has been applied to hydrogen with encouraging results (Chacham and Louie, 1991; Chacham, Zhu, and Louie, 1992).

In another problem, most DFs (i.e., those which treat electron correlations at a local or semilocal level) cannot describe van der Waals (vdW) interactions (dispersion interactions), giving rise to errors in the application of DFT to the low-pressure region of the hydrogen phase diagram, where weak vdW interactions between molecules are important (Silvera, 1980). Recent progress in DFT has been made, however, with the advent of so-called vdW DFs (Dion *et al.*, 2004; Lee *et al.*, 2010) and semiempirical density-dependent vdW corrections (Tkatchenko and Scheffler, 2009).

Once an approximate exchange-correlation functional is chosen, the DFT energy functional is well defined. For calculations, we must first choose the representation of the orbitals, i.e., the basis set. The most common bases are plane waves and linear combinations of localized functions, e.g., Gaussian functions. For calculations with periodic boundary conditions, plane waves are natural since they represent extended, delocalized states and they do not suffer from superposition errors of localized bases: the orbitals are written as

$$\psi_i(\vec{r}) = \sum_{\vec{G}} c_{\vec{G}}^i e^{i\vec{G}\cdot\vec{r}}, \tag{39}$$

where $\vec{G}$ belong to the reciprocal space of the simulation cell and the sum extends over all vectors such that $|\vec{G}|^2/2 < E_{\text{cut}}$. $E_{\text{cut}}$ is a cutoff parameter that controls the accuracy of the expansion. The value of the $E_{\text{cut}}$ needed to achieve a given accuracy depends on details such as the pseudopotential (see below), and the nature of the electronic states. While the kinetic and Coulomb energies are given by sums over $\vec{G}$, the exchange-correlation energy is most easily evaluated as a sum over a real space grid. The fast Fourier transform method is used to transform between real and reciprocal space during the solution.

However, plane waves require a dense grid to represent localized or highly oscillatory orbitals. This creates a problem for core states that are localized in the core region. In the majority of systems, core states are chemically inert so we should be able to remove them from the calculation without affecting the chemical properties which are determined by the valence states. Pseudopotentials are renormalized electron-nuclei potentials for the valence states that include both the Coulomb attraction of the nuclei and the screening effects resulting from the presence of core electrons. By employing pseudopotentials, not only do we remove core states from the calculation, but we also obtain valence states which are smooth in the core region; this greatly reduces the computational demands. There are many different types of pseudopotentials with different levels of transferability (the ability to reproduce the properties of the atom under different environments) and complexity. For additional details, see Martin (2004).

In DFT calculations, pseudopotentials are used for both hydrogen and helium even though neither of them possesses core electrons, but because the Coulomb potential $1/r$ requires a large plane wave cutoff greatly increasing the computational demands of the calculations. Since the pseudopotentials are built to reproduce the scattering properties of the atom, valence states should not be significantly affected outside of the core region.

#### 2. Treatment of proton zero-point motion

Within the normal framework of DFT, the treatment of nuclear quantum effects poses challenges. These are especially important in hydrogen, due to the light proton mass. Often, the treatment of ZPM is perturbative, adding corrections to the ground-state DFT results. Perhaps the simplest approximation is obtained by considering the ZPM to be harmonic, by neglecting anharmonic terms. The harmonic approximation gives the zero-point energy (ZPE) as an integral over the phonon density of states $F(\omega)$:

$$E_{\text{ZPE}} = \int d\omega F(\omega)\hbar\omega/2. \tag{40}$$

While this approximation is widely employed, it has long been known that this approximation can easily fail for light elements. For example, early calculations by Straus and Ashcroft (1977) showed that the harmonic approximation can incorrectly predict the relative stabilities of atomic crystal structures (see Sec. IV.A.6). In particular, only by treating coupling between the phonons self-consistently (i.e., including anharmonicity) are some structures energetically stabilized. In fact, anharmonic terms can be roughly equal in magnitude to the harmonic ones (Natoli, Martin, and Ceperley, 1993). While methods for approximating anharmonicity in ZPE estimates, such as the self-consistent *ab initio* lattice dynamics method (Souvatzis *et al.*, 2008) exist, these are still approximate, considering protons as classical particles. Rigorous inclusion of proton ZPM can be obtained by QMC calculations treating both the nuclei and electrons quantum mechanically at $T = 0$ K (Ceperley and Alder, 1987; Natoli, Martin, and Ceperley, 1993) or by using path-integral methods at a sufficiently low temperature as discussed elsewhere in this section.

#### 3. Born-Oppenheimer molecular dynamics

The simplest and more computationally time consuming way to perform FPMD simulations with DFT is to evaluate the forces on the nuclei at each MD step from a fully converged DFT calculation. This approach is known as Born-Oppenheimer molecular dynamics (BOMD) (Payne *et al.*, 1992; Marx and Hutter, 2009). The forces on the ions are calculated by the Hellman-Feynman theorem (Hellmann, 1937; Feynman, 1939), valid for the orbitals and density that minimize the KS energy functional. Since the Hellmann-Feynman theorem is applicable only at the variational minimum of the KS energy functional, the DFT calculation must be well converged. This makes the approach more expensive than the alternative method described below. Almost all DFT calculations employ iterative schemes to minimize the KS energy functional. The number of iterations needed to reach convergence depends crucially on the initial guess for the orbitals and electronic density. In order to make the calculations fast enough to make the BOMD approach practical for large systems, the orbitals at time $t + dt$ are estimated from the results at times $(t, t - dt, t - 2dt, \ldots)$, thus saving large factors of computer time, especially for systems with many electrons.

In the case of free-energy Born-Oppenheimer simulations, which includes thermal electronic excitations, the forces are calculated as the gradients of the electronic free-energy functional $\vec{F}_i = -\vec{\nabla}_i F_{\text{BO}}^{\text{KS}}$, corresponding to the approximation described in Sec. II.B.

#### 4. Car-Parrinello molecular dynamics

The Car-Parrinello molecular dynamics (CPMD) method (Car and Parrinello, 1985; Vuilleumier, 2006) started the field of first-principles simulations; it represented a major breakthrough in our ability to use computers to study the properties of materials. The approach enabled the direct study of the thermodynamic, optical, and transport properties of materials using much more realistic interatomic forces since the forces were calculated "on the fly" using DFT. CPMD is the main alternative to BOMD, appropriate if there is a gap in the excitation spectrum of the electrons. In the CPMD approach, instead of treating the electron and nuclear problems independently, the dynamics of both the ions and electronic KS orbitals are done simultaneously, but still within the BO approximation. The Lagrangian, used to define the dynamics, depends on the potential energy surface, regarded as a function, not only of the nuclear positions, but also of the electronic degrees of freedom: $E^{\text{KS}} = E^{\text{KS}}(\vec{R}, \{\psi_i\})$. The

orthogonality between KS orbitals is enforced using Lagrangian multipliers. The resulting Lagrangian is given by

$$\mathcal{L} = \sum_{i=1}^{N_e} \mu \int d\vec{r} |\dot{\psi}_i(\vec{r})|^2 + \sum_{I=1}^{N_n} \frac{1}{2} M_I \dot{\vec{R}}_I^2 - E^{\mathrm{KS}}(\psi, \vec{R}) + \sum_{i,j} \Lambda_{ij} [\langle \psi_i | \psi_j \rangle - \delta_{ij}], \quad (41)$$

where $\mu$ is a fictitious mass assigned to the electronic degrees of freedom. This leads to the following set of equations of motion for the orbitals and nuclear positions:

$$\mu \ddot{\Psi}_i(\vec{r}, t) = -\hat{H}_{\mathrm{KS}} \Psi_i(\vec{r}) + \sum_k \Lambda_{ik} \Psi_k(\vec{r}, t),$$
$$M_I \ddot{\vec{R}}_I = \vec{F}_I^{\mathrm{KS}} = -\frac{\partial E^{\mathrm{KS}}}{\partial \vec{R}_I}. \quad (42)$$

In addition, thermostats and barostats are added to produce constant temperature or variable cell algorithms (Martyna, Tobias, and Klein, 1994; Tuckerman and Parrinello, 1994a, 1994b; Hutter, Tuckerman, and Parrinello, 1995).

A simulation is begun using orbitals that minimize the KS energy functional. During the simulation, both nuclear positions and electronic orbitals are evolved in time simultaneously. The fictitious mass is adjusted so that the electronic subsystem remains sufficiently close to the Born-Oppenheimer energy surface, while the nuclei are kept at the physical temperature $T$. In a successful application of the method, the electronic degrees of freedom oscillate around the instantaneous BO energy surface throughout the entire simulation. This can be achieved only if the flow of energy between the electronic and nuclear degrees of freedom is eliminated, or reduced to a point where long enough simulations are possible before heating effects of the electronic degrees of freedom are seen. For the orbitals to follow the nuclei adiabatically and energy transfer not take place, the power spectra in the frequency domain of the two subsystems should not overlap (Marx and Hutter, 2000). This can be achieved for a system with an electronic gap and for a careful choice of the (fictitious) mass of the electronic orbitals. But for metals, the flow of energy between the two subsystems is hard to control. In practice, a separate thermostat can be applied to the electronic degrees of freedom to maintain them at low temperature. With the development of faster and more robust algorithms for DFT calculations, BOMD simulations have slowly gained popularity over CPMD, since they are easier to control and offer smaller chances of failure compared to CPMD. Nonetheless, CPMD is still a widely used and applicable method for FPMD simulations.

#### 5. Path-integral molecular dynamics

As mentioned in Sec. II.B, it is possible to introduce nuclear quantum effects within a BO framework with path-integral methods. The ionic quantum problem at finite temperature is mapped to a classical problem where each ion is represented by a ring polymer system; see Sec. II.B. If DFT is used to determine the forces arising from the electrons with either of the methods presented above, (CPMD or BOMD), the usual approach is to simulate ionic degrees of freedom (the ring polymers) also with molecular dynamics: path-integral molecular dynamics (PIMD). To achieve adequate sampling of the phase space of the ionic polymers, well-designed thermostats need to be used (Tuckerman *et al.*, 1993; Marx and Parrinello, 1996). Recent developments by Ceriotti *et al.* (2010) and Ceriotti, Manolopoulos, and Parrinello (2011) represent a promising alternative to thermalize PIMD simulations efficiently using generalized Langevin equations. Note that much more computer time is needed to include quantum effects of the nuclei, typically by 1 to 2 orders of magnitude, depending on the temperature and mass of the nuclei.

### F. Size effects

No discussion of simulation methods is complete without discussing the problem of size effects. Simulation methods try to reproduce the properties of bulk materials by studying a finite number of atoms in periodic boundary conditions. Since the particles interact with their (artificial) periodic images, the resulting calculations depend on the number of atoms used in the primitive cell. In principle, the most straightforward way to eliminate these effects is to study larger systems until the computed properties are independent of the number of atoms. While this is possible in simulations with semiempirical potentials, first-principles simulations are limited to systems of up to $\sim$1000 electrons. Hence, great care must be taken to ensure that results are close to the thermodynamic limit.

Size effects come in various forms and affect results in different ways; they can be divided into electronic and structural origin. Electronic size effects come about because electronic wave functions can be sensitive to the size and shape of the simulation cell and the Coulomb interaction between particles that are far apart must be correctly taken into account. This is particularly important in metallic systems where electronic states are delocalized over extended regions of the material. In electronic structure methods based on the single-body picture such as DFT, size effects are handled by integrating over the Brillouin zone of the unit cell, often called $k$-point integration (Martin, 2004). In this case it is possible to remove all electronic size effects from a unit cell of arbitrary size by considering sufficiently dense grids in the Brillouin zone; smaller unit cells require denser grids. Calculations at the so-called $\Gamma$ point, where Brillouin zone integration is not performed, are thus susceptible to finite-size errors. For all many-body methods such as QMC and PIMC there is, in principle, no way to obtain fully converged results using small unit cells exclusively; it is always necessary to consider progressively larger cells until results can be safely extrapolated to the infinite cell limit.

The understanding of size effects in many-body systems has progressed considerably over the last decade. The first step came with the introduction of twist averages boundary conditions (TABC) in QMC simulations (Lin, Zong, and Ceperley, 2001). TABC is the generalization of Brillouin zone integration to many-body quantum systems and is used to eliminate shell effects in the kinetic energy of metallic systems. By twisted boundary conditions, we mean

$$\Psi_\theta(\vec{r}_1, \ldots, \vec{r}_j + \vec{L}, \ldots, \vec{r}_N) = e^{i\theta} \Psi_\theta(\vec{r}_1, \ldots, \vec{r}_j, \ldots, \vec{r}_N), \quad (43)$$

where $\Psi_\theta$ is the many-body wave function of the system and $\vec{L}$ is the size of the periodic cell. Observables are then averaged over all twist vectors, similar to the procedure in single-body theories:

$$\langle \hat{A} \rangle = \int_{-\pi}^{\pi} \frac{d\vec{\theta}}{(2\pi)^3} \langle \Psi_\theta | \hat{A} | \Psi_\theta \rangle. \tag{44}$$

Chiesa *et al.* (2006) showed that most of the remaining finite-size errors in the energy come from discretization errors induced by the use of PBC, in particular, in the incorrect treatment of charge-charge interactions at wavelengths greater than the simulation cell. This work led to explicit formulas for the finite-size corrections to the energy and the pressure that are quite accurate in practice (Chiesa *et al.*, 2006; Drummond *et al.*, 2008). The method was extended to the Fermi-liquid parameters in the homogeneous electron gas (Holzmann, Bernu, and Ceperley, 2011), and the renormalization factor of sodium (Huotari *et al.*, 2010).

Size effects can also affect structural properties of the ions as the following two examples illustrate. First, for a finite simulation cell, only density fluctuations smaller than the length of the simulation are nonzero. This can be important near phase transitions, in particular, near critical points in the phase diagram, since there fluctuations have a longer wavelength. Second, in simulations of solids, only structures commensurate with the chosen simulation cell can be reached in a simulation causing a possible bias in structural predictions.

### G. Other theoretical methods

Here we briefly review other theoretical methods applied to hydrogen and helium at high pressure, focusing on the type of approximations employed and their expected range of applicability. With the rapid development and widespread use of first-principles methods over the last two decades, the use of semiempirical methods has become less important. Nonetheless, they can produce reliable and accurate results, and can be combined with first-principles methods, for example, by using FPMD results to determine intermolecular forces (Ercolessi and Adams, 1994).

#### 1. One-component and screened Coulomb plasma models

For temperatures and densities where the atoms are fully ionized, the electrons can be integrated out, and the proton-proton pair interaction treated using linear-response theory. In the limit of very high density, the electrons behave as a rigid background and the system can be modeled as the one-component plasma. This model, with classical protons, has been extensively studied since the early days of simulation (Brush, Sahlin, and Teller, 1966) to compute thermodynamics, structural and dynamical properties (Hansen, 1973; Pollock and Hansen, 1973; Hansen, McDonald, and Pollock, 1975; Vieillefosse and Hansen, 1975). The effect of quantum zero-point motion on the melting line has also been studied (Jones and Ceperley, 1996) by path-integral Monte Carlo methods.

At lower densities, the electrons cannot be treated as a uniform, nonresponding background. However, if the density is high enough ($r_s < 0.6$) for the electron-proton coupling to be a small perturbation to the electron system, the electronic screening can be computed by linear-response theory, and the electron-proton system mapped onto a system of protons interacting through an effective pair potential; the bare Coulomb potential screened by the electrons: the screened Coulomb plasma model (Galam and Hansen, 1976; Ashcroft and Stroud, 1978; Hansen and McDonald, 1981). This model was studied in the 1970s by Monte Carlo and thermodynamic perturbation methods in the high temperature regime (low Coulomb coupling) relevant to stellar interiors (Hubbard and Slattery, 1971; Hubbard, 1972; Ross and Seale, 1974; Ichimaru, 1982; Totsuji and Tokami, 1984; Dharma-wardana and Perrot, 2002), and, recently, at much lower temperatures to compute the melting line (Liberatore, Pierleoni, and Ceperley, 2011) of metallic hydrogen and deuterium at ultrahigh pressure. The electronic response function, the property of the many-body electron system that determines the effective proton's interaction, has been the subject of many investigations: many-body techniques, perturbation theory and diagrammatic theory, and numerical work using DFT and QMC (Giuliani and Vignale, 2005). Note that these are *ab initio* models; however, the range of validity of the description in terms of an effective interaction is limited to very high density or pressure. At lower density, nonlinear response theory needs to be used and the interaction between protons is no longer pairwise additive, complicating the description as an effective interaction (Nagao *et al.*, 2003).

#### 2. Semiempirical methods and chemical models

At low density, hydrogen forms molecules and an accurate description can be obtained by semiempirical models. At densities where the bond length of $H_2$ is less than the distance between molecules, it is accurate to assume that $H_2$ is a spherical particle interacting with other molecules through pair potentials, in particular, for parahydrogen and orthodeuterium. The effective potential has been optimized to represent the EOS of solid and liquid hydrogen at low pressure by Silvera and Goldman (1978) (SG). The SG potential reproduces the fluid isotherms of hydrogen from 75 to 300 K up to 2.0 GPa and the melting curve to 5.7 GPa, but cannot predict the Hugoniot curves. To remedy this Ross, Ree, and Young (1983) proposed a modified effective potential, the Ross, Ree, and Young (RRY) potential, by softening the SG potential at short range. Further improvements to match experimental data at higher pressures and temperatures in the liquid phase were proposed by Ross, Ree, and Young and tested by Matsuishi *et al.* (2003). Unfortunately, the transferability of effective potentials (i.e., the ability of a given potential fit in one set of conditions to adequately represent data for different conditions) is quite limited even when the system remains in the same thermodynamic phase.

More difficult is to extend the semiempirical approach to higher temperatures and/or higher densities under conditions where hydrogen is changing from molecular, to atomic and, ultimately, to the plasma state. Both pressure and temperature play roles in the transformation. In order to model this complex system, free-energy models based on the *chemical picture* were developed. One assumes a fixed set of chemical species, using pair interactions typically taken from empirical data, calculations, or from perturbation theory. The free

energy of the system is typically calculated assuming that the partition function factorizes into internal (vibrational-rotational and electronic excitations) and external (interaction between centers of mass) degrees of freedom. The resulting model is solved using some form of thermodynamic perturbation theory, integral equations from the theory of liquids, or classical simulations.

Several chemical models for hydrogen and hydrogen-helium mixtures have been proposed in the astrophysical community over the last 40 years (Ross, Ree, and Young, 1983; Ebeling and Richert, 1985; Saumon, Chabrier, and Horn, 1995; Juranek and Redmer, 2000; Juranek, Schwarz, and Redmer, 2003). An elaborate chemical model, known as the SCVH model, has been developed by Saumon, Chabrier, and van Horn (1995) by assuming a mixture of $H_2$, H, $e^-$, and $p^+$ and suitable pair potentials. This model reproduces most of the experimental data available, at both low temperature and high pressure (before crystallization) and high temperature and high pressure. The hydrogen EOS provided by this model is a standard for the planetary physics community. Another well-known model for hydrogen was developed by Kerley (1972, 2003). Its latest version produces results in very good agreement with first-principles simulations after a simple correction is made (Morales *et al.*, 2012). A similar strategy was developed to model high-pressure helium and to predict its EOS by Winisdoerfer and Chabrier (2005); however, existing models for H-He mixtures are still based on the EOS for the two pure systems and the linear mixing hypothesis. We show in Sec. V.B the limitations of this assumption.

### H. Comparison of simulation methods

To conclude our discussion of computational methods for dense hydrogen and helium we briefly summarize some of the strengths and weaknesses of the two most well-developed simulation methods: methods based on DFT and those based on QMC. Both methods are reliable *ab initio* methods and have been made feasible by the computer hardware available today.

Although DFT is, in principle, an exact theory, in practice only approximations to the density functional (DF) are known. This results in a number of challenges associated with the application of DFT to the study of dense hydrogen and helium. At present, many DFs exist (Burke, 2012). Moreover, it is not *a priori* known which is the most accurate for a given problem without experimental data or explicitly correlated calculations (e.g., QMC) to compare to. In other words, for any given problem, there is no internal measure of error within DFT with respect to the choice of the DF.

DFT in general shows serious deficiencies describing non-equilibrium geometries, such as reaction barriers and configurations with competing bonding patterns (Foulkes *et al.*, 2001; Martin, 2004). The simplest example, also particularly pertinent to our focus, is the molecular-to-atomic transition in hydrogen $H_2 \rightarrow 2H$ as two protons are pulled apart. The quality of the DFT description of each state ($H_2$ and 2H) is likely not equivalent, and so the physics associated with molecular dissociation will be poorly described. A much related problem, discussed already in Sec. II.D.1, is the accurate description of the band gap. Clearly one needs a reliable method for the band gap to describe well the metal-insulator transition in hydrogen.

QMC methods, are able to get around some of the problems that DFT methods have. For hydrogen, perhaps the biggest advantage is that QMC is able to treat molecular dissociation rather simply, while DFT methods have difficulty. In addition, no assumption is made about the density functional, and QMC does not need either pseudopotentials or basis sets. Another advantage of QMC methods is their ability to treat the zero-point motion of the protons in the same formalism, i.e., without making the Born-Oppenheimer approximation: at zero temperature by using projector methods for both electrons and nuclei, or using RPIMC for non-zero temperatures.

However, QMC methods typically take more computer resources than DFT methods and they come with different types of errors, both statistical and systematic. QMC methods face a difficulty arising from the mass difference of the proton and electron: since $M_p/m_e \simeq 1836$, the electrons move much faster than the protons in the DMC dynamics, resulting in a significant computational cost. At finite temperature, the mass ratio requires electronic paths to be much longer than nuclear paths causing difficulty in sampling the path space. The major conceptual bottleneck in QMC calculations is the "fermion sign problem": a direct QMC calculation is very inefficient; one has to resort to the fixed-node or fixed-phase approximation for calculations of extended systems, requiring an ansatz for when the wave function or density matrix changes sign. In most cases, fixed-node QMC methods have proved to be much more accurate than mean field methods. In contrast to DFT, the variational principle provides a rigorous way of deciding which ansatz is superior. RPIMC remains the only method to test (Militzer and Ceperley, 2001) predictions of chemical models (Saumon, Chabrier, and Horn, 1995) in the low density region of the phase diagram ($P \leq 1$ GPa) where molecules are well formed and nuclear motion occurs in the electronic ground state. In this situation the detailed structure of the nodes becomes irrelevant since electrons are paired in the bonding singlet state inside each molecule while molecules interact with the dipole-induced-dipole mechanism. Conventional DFT methods will be inaccurate and also very expensive unless localized basis sets are used.

In the past, QMC simulations have been limited in their ability to do simulations of sufficiently large systems. However, because QMC can be more easily adapted to a highly parallel environment, the computational limitations have lessened. As we show below, DFT and QMC, in fact, are giving similar results in many cases, providing confidence in their predictions.

## III. EXPERIMENTAL METHODS

The two primary experimental methods that have been used in the last decades to study hydrogen at high pressures are dynamic-compression methods based on shock experiments (Nellis, 2006b) and static-compression methods based on DACs (Mao and Hemley, 1994; Goncharov and Hemley, 2006). These two techniques are complementary, being applicable in different pressure and temperature conditions,

as discussed in Sec. I. In this section, we outline them, in order to facilitate the understanding of results that follow.

### A. Dynamic compression

Dynamic-compression techniques apply a very strong force to a small sample and then measure the properties of the resulting shock wave and its aftermath with specialized techniques. These methods can achieve higher pressures and temperatures than static methods, for example, ~500 GPa in hydrogen and temperatures of 50 000 K. However, such measurements typically have large uncertainties in the resulting pressures and temperatures, or in the measured properties, since they must be done very rapidly. In addition, there are limitations in the accessible values of pressure and temperature, as discussed below.

Traditional dynamic methods apply one or more shocks to a system, producing a sharp increase in pressure over a short time (e.g., ~100 GPa over 1 ps). Because the shock process is adiabatic, large increases in temperature also occur with the increases in pressure. A number of techniques have been developed to produce shocks, including gas guns (Nellis, Mitchell *et al.*, 1983), laser-driven compression (Da Silva *et al.*, 1997; Collins, Da Silva *et al.*, 1998; Collins *et al.*, 1998; Hicks *et al.*, 2009; Sano *et al.*, 2011b), magnetically driven flyers (Knudson *et al.*, 2001, 2004; Knudson and Desjarlais, 2009), and hemispherically converging explosives (Boriskov *et al.*, 2005).

If the applied force is strong enough, a shock wave propagates into the sample. One measures the velocity of the material at the surface of the sample and that of the resulting shock wave. Assuming that the shock is a plane, the conservation laws of mass, momentum, and energy lead to the Rankine-Hugoniot equations. In principle, this gives the pressure, energy, and density of the postshocked material in terms of the measured velocities and the values of the initial energy, pressure, and density. The locus of states reachable from a given initial state using different amounts of applied force is called the Hugoniot curve, which satisfies (Zeldovich and Raizer, 1967)

$$E - E_0 = \frac{p + p_0}{2}(v_0 - v), \tag{45}$$

where $E$, $p$, and $v$ are specific internal energy, pressure, and specific volume, respectively, and the subscript 0 refers to the state of the sample prior to the shock. One can explore different regions in phase space by either shocking precompressed samples or measuring properties after the shock wave reflects from a boundary. As can be seen, shock compression cannot access all values of temperature and pressure.

Hugoniot states for deuterium up to ~100 GPa are shown in Fig. 1. Many shock measurements have been performed on deuterium rather than hydrogen, because its initial density is higher (the larger mass of deuterium reduces its ZPM, and thus the molecular bond length and spacing between molecules as well) and has a lower shock impedance. Thus, the same shock applied to both hydrogen and deuterium will achieve higher pressures in the latter. In passing, we mention that the principle Hugoniot for hydrogen has in fact recently been measured up to 55 GPa using laser-driven shock compression (Sano *et al.*, 2011b). See Sec. IV.B.1 for a detailed discussion of the measured (and calculated) Hugoniots of both isotopes.

Dynamic-compression methods other than single shock exist to reach off-Hugoniot states, the simplest being a double shock (Nellis, Mitchell *et al.*, 1983; Fortov *et al.*, 2003). Such data for deuterium (Nellis, Mitchell *et al.*, 1983) are also shown in Fig. 1. Other methods, for example, include explosive-driven generators (Fortov *et al.*, 2007), shock reverberation (Weir, Mitchell, and Nellis, 1996), and isentropic compression (Nellis, 2006b). The latter are capable of achieving lower temperatures than the single-shock method, due to the fact that compression occurs over much longer time scales. Furthermore, these can tune independently between states on the Hugoniot and those obtained by isentropic compression, allowing many pressure and temperature points to be reached. Although, because of their complexity relative to single shocks, it is more difficult to assess errors in the measurements.

If the data obtainable from dynamic measurements were highly accurate, besides being useful for planetary modeling, they would constitute an excellent benchmark for simulation methods. However, the shock velocities need to be measured very precisely and accurately to get reliable EOS points. Even then, there are many assumptions that must be made to analyze the measurements. For a single shock, one assumes that the material in front of the shock is not preheated, that the material after the shock passes through is in equilibrium, that the shock remains one dimensional and parallel to the camera angle, and that there are no other shock waves reflected from the boundaries of the sample. Note that the temperature is not directly measured either, but is usually estimated by fitting the spectrum of the emitted radiation to a gray-body formula. Hence, a further assumption is that the radiation is predominately coming from the material after it has been shocked and not from other parts of the apparatus.

As can be seen, there are advantages and disadvantages to dynamic-compression techniques; while they can reach relatively high pressures and temperatures, the conditions are transient (the time of the shock) and reaching general thermodynamic point is difficult, and there are therefore large uncertainties in measured properties.

### B. Static compression

Static-compression techniques, produced by DACs, can also realize extreme thermodynamic conditions (Mao and Hemley, 1994; Goncharov and Hemley, 2006). Because they are static (or nearly so), they are more precise and accurate than their dynamic counterparts. At the same time though, the pressures and temperatures are more limited. Recent advancements allow pressures to be reached near the limit of mechanical strength of the DACs and temperatures of thousands in Kelvin. The scope of these conditions is outlined in Fig. 1.

In general, static-compression methods are based on compressing a sample between diamond anvils (used for their large mechanical strength) and heating it using external resistive couplers or lasers. Note that metal gaskets are placed along the sides of the system to prevent the escape of the

sample. Optical measurements, such as Raman and/or IR spectroscopy, or x-ray scattering is then used to monitor and analyze the sample.

At high pressures, the chemical reactivity of a material often increases greatly, and hydrogen is no exception. This causes challenges for static techniques, since chemical reactions can occur with both the diamond anvils of the gasket material. Such a reaction can then contaminate the sample. Also, hydrogen can penetrate into small cracks and escape, or catalyze the growth of fractures in the diamonds; and because hydrogen is so compressible, stresses in the diamond are more of a problem than with other materials. These issues limit achievable pressures to lower values than otherwise obtainable. However, the recent advancement of using liners, such as gold (Datchi, Loubeyre, and LeToullec, 2000), allowed pressures near the limit of mechanical strength of the diamond, ~320 GPa (Goncharov *et al.*, 2001; Loubeyre, Occelli, and LeToullec, 2002), as remarked above.

Creating high temperatures has also been a challenge for static methods, since these cause the diamonds to become less stable. Two types of heating methods exist, external resistive heating and that by laser, as also mentioned above. The former provides uniform temperatures, but limits those accessible to less than ~1000 K. Laser heating of a small part of the sample is capable of producing higher temperatures, but also can result in large thermal gradients; although, recent advancements now allow relatively uniform heating (Lin *et al.*, 2004) and temperatures up to ~1500 K have been achieved (Subramanian *et al.*, 2011).

Measuring the precise pressures and temperatures that are achieved is challenging. Pressure sensors often rely on the optical properties of materials, such as the fluorescent properties of small ruby crystals embedded in the sample, the signals of which decrease and broaden with temperature. Furthermore, both temperature and pressure sensors measure only local conditions, and gradients may be important, as mentioned above. Additional challenges exist, such as temperatures affecting pressures, drift of the diamond anvil cells, etc. It is important to note though that many of these issues have been minimized to a large extent, as outlined by Goncharov and Hemley (2006).

The major advantage of static-compression methods is that they allow long, accurate, and repeatable measurements at precise thermodynamic conditions. As discussed, these include optical properties, such as IR and Raman spectra (Goncharov *et al.*, 2001; Loubeyre, Occelli, and LeToullec, 2002), as well as structural properties using x-ray diffraction (Akahama *et al.*, 2010). It is measurements such as these that have proven most vital for understanding the low-temperature properties of hydrogen, as discussed in Sec. IV.

### C. Coupling static and dynamic compressions

Recently, techniques that combine static and dynamic compressions have been proposed that hold promise to explore the phase diagram of hydrogen and other systems over a broader range of conditions than either type of compression alone. Since the Hugoniot is entirely determined by the initial state of the sample, precompression allows one to explore a range of final states. The feasibility of such experiments has in fact been demonstrated on hydrogen. Loubeyre *et al.* (2004), for example, used DACs to precompress hydrogen, which was then shocked using a focused laser. This method was found to provide consistent results for thermodynamic points between the principal Hugoniot of cryogenic hydrogen subjected to a single shock and those generated by a reverberating shock wave experiment (Weir, Mitchell, and Nellis, 1996). In a similar study by Grishechkin *et al.* (2004b), precompressed gaseous targets were shocked. In passing, we note that this technique was also applied to other systems, such as high-pressure helium (Eggert *et al.*, 2008) and water (Jeanloz *et al.*, 2007).

## IV. HYDROGEN UNDER EXTREME CONDITIONS

In this section, we discuss the properties of pure hydrogen under extreme conditions. Because experimental studies under such conditions pose many challenges, much of our understanding comes from theoretical predictions and simulations. Efforts to understand the low-temperature properties are first discussed, namely, the solid phases. Properties of the liquid phase follow, with a particular focus on the LLT. A discussion of some novel theoretically predicted phases, including superconducting and low- or zero-temperature fluid states, concludes.

### A. Solid phases

Experimental measurements revealed the existence of at least three low-temperature solid phases, with the possibility of two more at elevated temperatures. What is currently known about the phase diagram from both experiments and simulations is shown in Fig. 3; this is discussed further below. Theoretical calculations greatly contributed to its understanding, predicting the existence and qualitative properties of several phases prior to experimental discoveries. In this section, we first discuss the low-temperature (ground-state) solid phases, and then those at elevated temperatures that have been experimentally observed. Following this, we discuss theoretical and computational predictions of the existence of additional phases at pressures beyond those currently accessible experimentally. We then consider the melting of the molecular crystals. Finally in this section, we consider metallization and molecular dissociation to an atomic state, effects that may or may not occur simultaneously.

#### 1. Solid molecular hydrogen at low temperatures

DAC experiments have made many important discoveries concerning the phase diagram of solid molecular hydrogen at high pressures (Mao and Hemley, 1994). Figure 3 shows a detailed view of the experimental phase diagram of solid hydrogen at high pressure and low temperatures. The three low-temperature phases firmly established experimentally are labeled as phases I, II, and III. Note that in the literature, the latter two phases are also known as the broken symmetry phase (BSP) and the hydrogen-*A* (H-*A*) phase, respectively.

At low pressures, anisotropic intermolecular interactions between hydrogen molecules are weak. Because of this, the angular momentum of an individual molecule ($J$) remains a good quantum number. Further, since there is a large

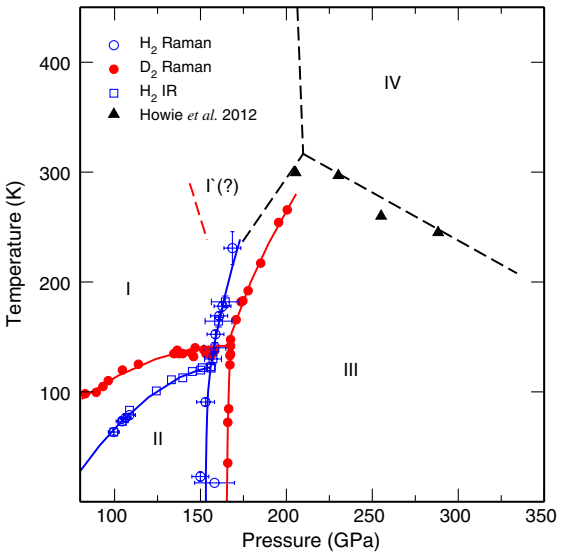


FIG. 3 (color online). High-pressure phase diagram of solid molecular hydrogen. Open and filled circles are Raman measurements for hydrogen and deuterium, respectively, and open squares are IR data for the former. Triangles and corresponding dashed lines indicate inferred boundaries for the recently proposed phase IV (Howie *et al.*, 2012). Note also that the dashed line and the existence of phase I' are still matters of debate, as discussed in the text. Adapted from Goncharov, Hemley, and Mao, 2011.

separation of the rotational energy levels, only either the $J = 0$ (parahydrogen or para-$H_2$) or $J = 1$ (orthohydrogen or ortho-$H_2$) states are thermally populated at low temperatures. $p$-$H_2$ molecules freely rotate about their centers of mass (i.e., each has essentially a spherically symmetric wave function, and the molecular bond angles are completely disordered, even at $T = 0$ K), whereas $o$-$H_2$ aligns even at very low temperatures. At the low pressures under discussion, the interconversion between $o$- and $p$-$H_2$- is very slow, and the phase diagram is thus sensitive to their concentration (this is also because they interact differently). For example, it has been found that $p$-$H_2$ at low pressures crystallizes in the close-packed hcp structure (Keesom, de Smedt, and Mooy, 1930; Hazen *et al.*, 1987), referred to as phase I, whereas molecules in $o$-$H_2$ orient along the body diagonals of a fcc structure with $Pa3$ symmetry (Clouter and Gush, 1965; Mills and Schuch, 1965; Mills, Yarnell, and Schuch, 1973; Yarnell, Mills, and Schuch, 1975). An extensive review and discussion of the low-pressure theory and experiment for solid molecular hydrogen can be found in Silvera (1980).

As the pressure is increased, while at temperatures lower than ~140 K, the rotational symmetry of phase I is broken, and hydrogen transforms into phase II (hence the designation as the BSP). Thus, the structure of phase II is determined by the zero-point rotational energy of the molecules, and therefore the boundary between the two phases is sensitive to isotope. It is sensitive to the temperature as well, but when this is very low, it occurs near 27.8 GPa in $o$-$D_2$ (Silvera and Wijngaarden, 1981), 70 GPa in HD (Moshary, Chen, and Silvera, 1993), and 110 GPa in $p$-$H_2$ (Lorenzana, Silvera, and Goettel, 1990).

As the pressure is increased to ~150 GPa, molecular hydrogen undergoes another phase transition (Hemley and Mao, 1988; Lorenzana, Silvera, and Goettel, 1989) to phase III. The thermodynamic stability range of this phase has recently been experimentally demonstrated to extend to pressures beyond 300 GPa and temperatures up to 300 K (Zha, Liu, and Hemley, 2012). This transition is more robust than that between phases I and II, with the pressure being relatively insensitive to the isotope. This suggests that phase III is mainly determined by the Born-Oppenheimer energy of interacting static molecules (i.e., classical ordering).

Experimental measurements have only been able to provide limited information about the molecular orientations in the higher pressure phases (II and III) of hydrogen. The small sample sizes and low x-ray scattering efficiency (proportional to the atomic number squared) pose challenges to structural identifications (the primary method to determine such information). Although recent measurements (Akahama *et al.*, 2010) up to 183 GPa indicate that the center of each molecule remains close to the hcp lattice sites of phase I in all phases. The basic hexagonal symmetry was also seen in neutron scattering measurements of phase II of deuterium (Goncharenko and Loubeyre, 2005), which is furthermore evidence for partial orientational ordering.

The most important experimental constraints come from spectroscopy. Three IR modes and one Raman mode are observed for phase II (Cui, Chen, and Silvera, 1995). Then, at the phase II ⟶ III transition, a jump in the intermolecular vibron (Hemley and Mao, 1988; Lorenzana, Silvera, and Goettel, 1989) and a large increase in absorbance of the IR-active vibron are observed. The number of low-frequency Raman-active modes and possible second Raman vibron indicate that, in phase III, the primitive cell should contain at least four molecules (Goncharov *et al.*, 1998). Furthermore, the fact that the IR and Raman vibrons and phonons have different frequencies implies a center of symmetry. Finally, the presence of Raman-active phonons means that any center of inversion is between molecules.

There have been many, and varied, attempts to identify the structures of phases II and III via simulations. As we demonstrate however, a consensus has not yet been reached.

At relatively low pressures, thus pertinent to both $o$-$H_2$ in phases I and II, an appropriate simplified model has found extensive use (Freiman *et al.*, 2003); this model consists of quantum rotors fixed on a lattice which interact via a quadrupolar interaction (Nakamura, 1955; Felsteiner, 1965):

$$H = \sum_{i=1}^{N} B\mathbf{L}_i^2 + \sum_{i<j} V(\Omega_i, \Omega_j; \mathbf{R}_{ij}), \tag{46}$$

where $B$ is the rotational constant (the presence of which highlights the expected differences between isotopes), $\mathbf{L}_i$ is the angular momentum operator of rotor $i$, and $V$ is the interaction energy between two quadrupoles, where $\Omega_i$ ($\Omega_j$) is the orientation of rotor $i$ ($j$) and $\mathbf{R}_{ij}$ is the vector between rotors. Equation (46) provides immediate physical insight into hydrogen. For example, an array of classically ordered electric quadrupoles has a lower energy in a fcc lattice than in hcp, which explains the observed structure and ordering in phase I of $o$-$H_2$. While this model assumes classical rotors, its use was early on supported with a more rigorous treatment involving a quantum mechanical model (Raich and James, 1966). Although the model is not perfect,

as, for example, the observed lattice of $p$-$H_2$ is hcp, presumably effects not described in the above Hamiltonian favor its formation in this case.

There have been several adaptations of the quantum rotor model. For example, PIMC simulations by Runge *et al.* (1992) on phase II used a more accurate pairwise intermolecular potential derived from LDA calculations. It was found that $o$-$D_2$ would indeed order first into the $Pa3$ structure, but then transform to an ordered hcp structure, whereas $p$-$H_2$ would order directly into the latter. Unfortunately, while providing results qualitatively consistent with what one would expect for both the isotope effect of the transition and finite-temperature features, a group theoretical analysis (Cui, Chen, and Silvera, 1995) showed that both structures are quantitatively incompatible with the constraints imposed by the observed number of IR (3) and Raman (1) modes. Later calculations expanded these ideas even further. PIMC calculations by Surh *et al.* (1997) considered both fcc and hcp lattices of rotors, finding a structure with $P6_3/m$ symmetry, which is hexagonal with some molecules in plane and some perpendicular to it. Unfortunately, the group theoretical analysis by Cui, Chen, and Silvera (1995) also rules out this structure, due to an insufficient number of IR vibrons. One such calculation that has not yet been ruled out are the PIMC calculations by Cui *et al.* (1997), where $Pa3$-type ordering (i.e., molecules along the body diagonals) on a hcp lattice was suggested. This prediction has recently been suggested to be qualitatively consistent with neutron diffraction of deuterium (Goncharenko and Loubeyre, 2005). Confusing these predictions, however, are the facts that those experiments suggest that the structure of phase II may be isotope dependent and those from more recent simulations suggest that phase II cannot be described in terms of a single classical structure (Geneste *et al.*, 2012). As can be seen, quantitative predictions (for phase II) are still lacking.

Other approaches to predict molecular orientations are based on fully *ab initio* calculations, including DFT or QMC. Typically, these have been based on evaluating BO energies for static lattices, which as discussed below, neglect important contributions to the energetics from proton ZPM and thermal effects. A number of candidate structures have been proposed for phase II (and III) based on such calculations, some of the most well-studied structures including $Cmc2_1$ (Kitamura *et al.*, 2000), $P2_1/c$ (Johnson and Ashcroft, 2000; Zhang *et al.*, 2007), and $Pca2_1$ (Kohanoff *et al.*, 1997; Nagao, Takezawa, and Nagara, 1999; Städele and Martin, 2000). These lattices and molecular orderings are shown in Fig. 4. As can be seen, besides differing molecular orientation, they are all similar, consisting of orthorhombic primitive cells with lattice sites close to hcp.

Among the structures shown in Fig. 4, $Pca2_1$ has been one of the most thoroughly studied and considered a strong candidate for phase II. This structure was first suggested as the ground state of a classical quadrupolar system (Kitaigorodskii and Mirskaya, 1965), and then later proposed as the ground state of hydrogen based on DFT calculations (Nagara and Nakamura, 1992). Further DFT calculations employing an exact-exchange functional (Städele and Martin, 2000) also supported the stability of

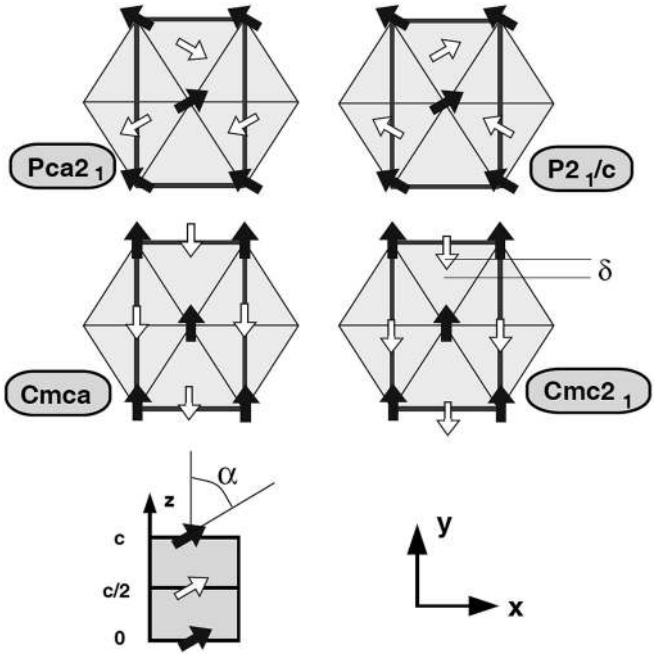


FIG. 4. Possible molecular orientations (indicated via arrows) for dense hydrogen (phases II and III), assuming four molecules per unit cell. The solid (empty) arrows represent molecules at $c$ ($c/2$) lattice positions. Molecules are tilted with respect to the $c$ axis at an angle $\alpha$ of $\sim 55°$, and $\delta$ indicates the distance of each molecular center (of mass) from an ideal hcp lattice. From Städele and Martin, 2000.

$Pca2_1$. However, the correctness of $Pca2_1$ is called into question by the Raman experiments; a single mode is observed, while $Pca2_1$ should exhibit four. An explanation though might be found in either a relatively small signal-to-noise ratio or cancellations between various vibrational modes in the experiments (Cui, Chen, and Silvera, 1995; Kohanoff *et al.*, 1997).

Recently, more sophisticated methods to determine crystal structures have been proposed (Woodley and Catlow, 2008), and some of these have been applied to hydrogen. These methods attempt to find the most stable crystal structure without necessarily imposing any constraints on the unit cell. In the *ab initio* random structure searching (AIRSS) method (Pickard and Needs, 2006), for example, one relaxes a number of randomly produced structures by minimizing the BO energy. After a large number of trials, one assumes that the correct structure has been found. Such calculations have been applied to hydrogen by Pickard and Needs (2007), which in fact again revealed the $Pca2_1$ and $P6_3/m$ structures, or possibly a similar structure with 24 atoms, $P21/c$-24 (Pickard and Needs, 2009). As indicated, many of the searches to date have been based on determining molecular orderings with classical protons, and adding an approximate ZPE as a second step. Dynamical lattice calculations using DFT linear-response theory (Zhang *et al.*, 2006), for example, suggested that $Pca2_1$ remains stable if ZPE is taken into account in the pressure range $110 \leq P \leq 150$ GPa. Furthermore, even though this approach lacks rotational motion (relevant to phase II, for example), an examination of the rotational energies of a set of candidate structures further suggests that $Pca2_1$ is the least energetic (Moraldi, 2009).

Early on, Barbee, III *et al.* (1989) used DFT to focus exclusively on structures for phase III, finding a structure with molecular bonds aligned along the $c$ axis of a hcp lattice. However, later DFT calculations found more stable structures with molecules oriented in the $(a, b)$ plane (Kaxiras, Broughton, and Hemley, 1991; Kaxiras and Broughton, 1992). QMC calculations by Natoli, Martin, and Ceperley (1995) agreed with this assessment, finding the orientation angle to be roughly 60° (as are the structures shown in Fig. 4). Note that this is consistent with the experimental data, as molecular orientation along the $c$ axis will not exhibit IR activity. By considering larger unit cells, Nagara and Nakamura (1992) found the hexagonal $Pca2_1$ structure. However, this structure is inconsistent with phase III (Cui, Chen, and Silvera, 1995), and is a more likely candidate for phase II, as discussed above. Most promising is the AIRSS study by Pickard and Needs (2007), which revealed a structure with 12 molecules per unit cell with molecular centers close to distorted hcp lattice sites and overall $C2/c$ symmetry, as shown in Fig. 5. This prediction agrees qualitatively well with both the limited diffraction data (Akahama *et al.*, 2010) and the spectroscopic data for phase III, such as the intense IR activity.

As can be seen, the use of computational methods to predict the structures of phases II and III of hydrogen has resulted in unexpected complexity. While qualitative insight has been provided, suggesting $Pca2_1$ and $C2/c$ as plausible candidates for phases II and III, respectively, many open questions remain; and although methods to find systematically the lowest energy structure have made impressive advances recently (Woodley and Catlow, 2008) (albeit at a greatly increased computational cost), challenges remain. One of the most significant problems is how to accurately estimate the effect of proton ZPM. For example, by estimating the ZPE using frozen-phonon calculations, Surh, Barbee, III, and Mailhiot (1993) suggested that $c$-oriented molecules in an hcp lattice were actually more stable than $Pca2_1$, directly in contrast with the static-lattice predictions. Of course, more accurate estimates of ZPM could be made via a PIMD, PIMC, or QMC (Ceperley and Alder, 1987) simulations, at a much increased computational cost. We return to the issue of ZPM in Sec. IV.A.6. It is important to keep in mind that since the ZPE of the protons can be larger than the difference in energy between various candidate structures, structure searching, even including an approximate ZPE should be approached with caution. Also, the structure-searching results discussed above have relied primarily on DFT, the accuracy of which depends on the assumed DF. Many calculations have employed LDA or GGA DFs, which do not adequately describe vdW interactions at low pressures and severely underestimate the band gap at higher ones (Städele and Martin, 2000). As discussed in Sec. II.H though, recent advancements have been made to improve DFs so that one may hope for much more reliable predictions in the near future. In any case, it is clear that more work needs to be done both theoretically and experimentally to understand solid molecular hydrogen at low temperature.

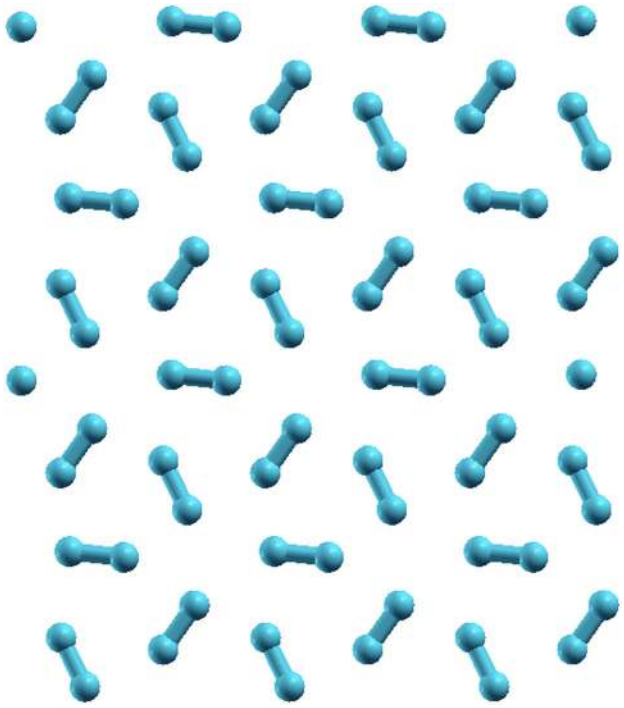

FIG. 5 (color online). The most likely candidate for phase III of hydrogen, the $C2/c$ structure, as predicted by Pickard and Needs (2007). This structure essentially consists of rings of three molecules, which are responsible for its strong optical activity.

### 2. Solid molecular hydrogen at finite temperature

Goncharov *et al.* (1995) noticed a change in the slope of the I–III phase line of deuterium, along with a subtle discontinuity of the intramolecular vibron as a function of pressure. In addition, the observed discontinuity in the vibron frequency across the I–III transition line became vanishingly small above 254 K. These observations suggest that there may be another phase, denoted by I', located at higher temperature than phase I ($T \geq 170$ K). Those results suggest that this phase is isostructural with phase III with a critical (or tricritical) point where the vibron discontinuity vanishes [see, e.g., Fig. 5 of Goncharov *et al.* (1995)].

Further support in favor of phase I' was provided by PIMC calculations based on the quantum rotor model (see Sec. IV.A.1) by Surh *et al.* (1997). However, the accuracy of the used effective intermolecular potentials is unknown.

Recent experimental support for phase I' was provided by Baer, Evans, and Yoo (2007, 2009) using coherent anti-Stokes Raman spectroscopy on deuterium samples. Comparing the pressure dependence of the Raman shift of the deuterium vibron along two isotherms, at 77 and at 300 K, they observed a change of slope around 140 GPa which they ascribed to the signature of the phase transition from phase I to I' along the 300 K isotherm, in agreement with Surh *et al.* (1997), and in qualitative agreement with the early experimental results. However, to reconcile the two different experiments, the I–I' phase line would need to have a negative slope (see Fig. 3), thus exhibiting a strong temperature dependence not observed in the early experiments (Goncharov *et al.*, 1995).

Most recently, Goncharov, Hemley, and Mao (2011) performed a more refined study and concluded that the new data and analysis do not support the existence of phase I'. As can be seen, uncertainties still remain surrounding the existence and the details of phase I', and further systematic investigations are necessary.

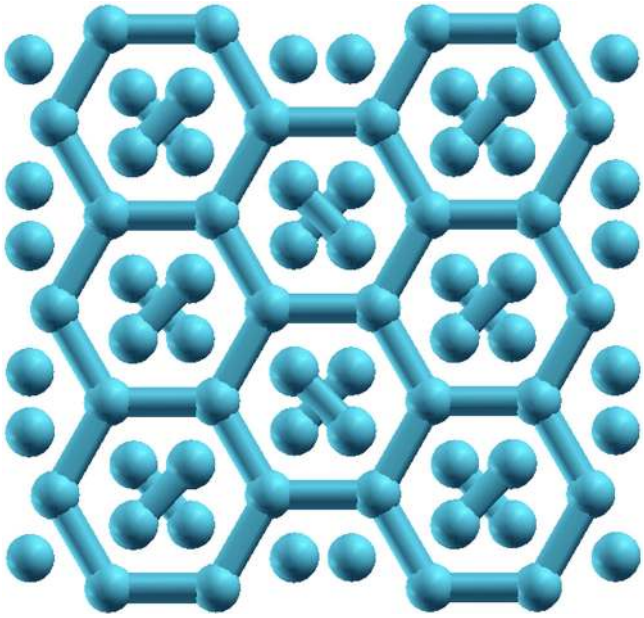

FIG. 6 (color online). The candidate structure of phase IV of hydrogen, suggested by Howie *et al.* (2012) and Pickard, Martinez-Canales, and Needs (2012a). The structure consists of alternating atomic graphenelike and molecular layers.

Recently Raman and visible transmission spectroscopy measurements at room temperature ($T \sim 300$ K) (Eremets and Troyan, 2011; Howie *et al.*, 2012) suggest yet a further phase transition, an entropically driven (and reversible) one to phase IV.[6] After compressing to phase III, Howie *et al.* (2012) observed three spectroscopic signals near 220 GPa, indicative of this transition: (i) the appearance of the second fundamental vibrational mode, (ii) a dramatic softening and broadening of the first fundamental vibrational mode, and (iii) the appearance of new low-frequency phonon excitations.

The Raman spectra suggest that two distinct local environments exist in phase IV. By comparing these data to the previously predicted ground-state structures of solid hydrogen (Pickard and Needs, 2007), Howie *et al.* (2012) suggested that phase IV could be a mixture of graphenelike layers and unbound hydrogen molecules, such as is shown in Fig. 6. Note that the graphenelike layers are shown with equal distances between protons [corresponding to the *Ibam* structure of Pickard and Needs (2007)]. However, experiments suggest that equal bond distances occur only at higher pressures; at lower pressures, hydrogen dimers undergo pairing fluctuations (Howie *et al.*, 2012), possibly resulting in a lower-symmetry structure, such as *Pbcn* (Pickard and Needs, 2007).

Immediately following the experimental evidence for phase IV (Eremets and Troyan, 2011; Howie *et al.*, 2012), AIRSS was reapplied to the problem of high-pressure molecular hydrogen (Pickard, Martinez-Canales, and Needs, 2012a, 2012b), this time using larger unit cells. A number of consistent mixed phases were found with space groups *Pc*. These results are consistent with even more recent metadynamics calculations (Liu *et al.*, 2012) based on DFT which suggest the finite-temperature structure is partially disordered, with hydrogen molecules ordering in one layer and disordering in the next. Particularly interesting about these calculations is that by estimating the ZPE and its entropic contribution to the free energy within the quasiharmonic approximation, they have lower free energies relative to the presumed structure for phase III, $C2/c$ (Pickard and Needs, 2007), consistent with experiment (Howie *et al.*, 2012). Although, one must keep in mind that the errors involved in this approximation and the used DF could possibly be larger than the differences in energies of the various proposed structures.

Around the same time of these measurements and calculations, however, Zha, Liu, and Hemley (2012) performed IR and optical absorption measurements using DACs at similar thermodynamic points that were studied by both Eremets and Troyan (2011) and Howie *et al.* (2012). Their measurement did not reveal strong evidence for, or even suggest, a transition to a new phase. However, the temperatures were slightly lower, and from their results such a transition could not be completely ruled out.

### 3. Additional solid molecular phases

DAC measurements indicate that the thermodynamic stability range of phase III is quite large; the strong IR absorption of the vibron (Goncharov *et al.*, 1998) was early on demonstrated to persist up to at least 320 GPa, at relatively low temperatures (Goncharov *et al.*, 2001; Loubeyre, Occelli, and LeToullec, 2002). Measurements (Zha, Liu, and Hemley, 2012) recently extended this range even further, to 360 GPa (at low temperatures) and up to 300 K (at low pressures). Calculations support this large stability range and also suggest that additional solid phases may exist at elevated pressures.

The recent AIRSS studies by Pickard and Needs (2007) and Pickard, Martinez-Canales, and Needs (2012a) (see Sec. IV.A.1), for example, predicted not only a plethora of structures for phases II and III, but also suggested two further phase transitions at higher pressures. Above 285 GPa, they suggested that phase III will transform to a structure with *Cmca* symmetry and 12 atoms in the unit cell, which is thus referred to as *Cmca*-12, as shown in Fig. 7. *Cmca*-12 is rather similar to the (presumed) structure of phase III ($C2/c$, Fig. 5); for example, consisting of three-molecule rings, except the layering in *Cmca*-12 has the form $\cdots ABA \cdots$, the molecules lie flat within each layer, and the distortion of the molecular centers from hcp packing is larger.

Considering ZPM in the quasiharmonic approximation, these studies also suggested that the transition from phase III should be primarily pressure driven (i.e., temperature independent), occurring near 240–285 GPa, which is indicated in the phase diagram in Fig. 3. One might wonder why the transition to *Cmca*-12 has not been directly observed in the DAC experiments (Goncharov *et al.*, 2001; Loubeyre, Occelli, and LeToullec, 2002; Zha, Liu, and Hemley, 2012). Of course, it is plausible that there are inaccuracies in the calculations that affect these predictions, such as the DF employed in the DFT calculations or the perturbative treatment of proton ZPM, errors which are expected to become increasingly important with increasing pressure, and which we have iterated numerous times already. Further calculations and

[6]A transition to a high-pressure and high-temperature phase was already reported by Mao and Hemley (1989), but not characterized.

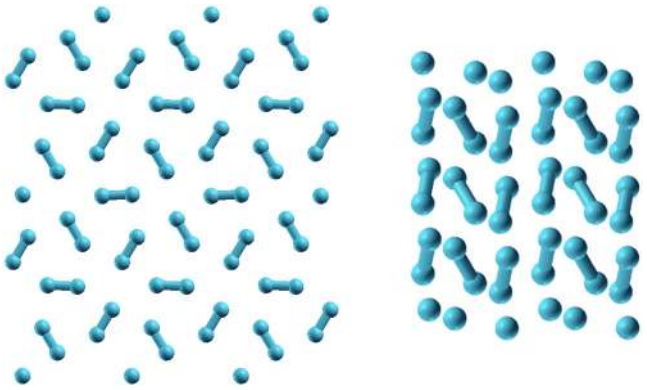

FIG. 7 (color online). A single layer of the *Cmca*-12 structure (Pickard and Needs, 2007) at 300 GPa (left) and the $C2/c(2)$ structure (Liu, Wang, and Ma, 2012) at 500 GPa (right). Note that due to the higher compression, $C2/c(2)$ has been enlarged relative to *Cmca*-12. Note also that the other predicted high-pressure molecular phase *Cmca*, occurring at pressures intermediate between *Cmca*-12 and $C2/c(2)$, is shown in Fig. 4.

experiments are necessary to assess the accuracy of these predictions.

The other phase transition predicted by the AIRSS study of Pickard and Needs (2007) occurs near 385 GPa, from *Cmca*-12 to *Cmca*, the structure originally proposed by Edwards, Ashcroft, and Lenosky (1996); see Sec. IV.A.1 and recall that its structure is shown in Fig. 4. The recent metadynamics calculation by Liu *et al.* (2012) supports the transition to *Cmca*, and further suggests that at finite temperature, phase III may transform directly to it without passing through *Cmca*-12.

Labet *et al.* (2012) and Labet, Hoffmann, and Ashcroft (2012a, 2012b, 2012c) recently considered this process of molecular dissociation more in-depth, by focusing on the relationship between and variations of intramolecular and intermolecular bond lengths with pressure, or more precisely, the shortest ($r_{\mathrm{H\text{-}H}}$) and second-shortest ($R_{\mathrm{H_2\text{-}H_2}}$) proton distances, respectively. To quantify their results, they introduced an equalization function $\xi(P)$ at pressure $P$ introduced as

$$\xi(P) = 1 - \frac{R_{\mathrm{H_2\text{-}H_2}}(P) - r_{\mathrm{H\text{-}H}}(P)}{R_{\mathrm{H_2\text{-}H_2}}(P_{1\ \mathrm{atm}}) - r_{\mathrm{H\text{-}H}}(P_{1\ \mathrm{atm}})}. \tag{47}$$

$\xi$ is an order parameter, evolving from $\xi = 0$ (free-space molecules) to 1 (an atomic state, where all proton distances are equal), during dissociation. Focusing on the structures predicted in the AIRSS study by Pickard and Needs (2007), Labet *et al.* (2012), and Labet, Hoffmann, and Ashcroft (2012a, 2012b, 2012c) found a discontinuous shift at the transition from *Cmca* to the atomic phase, leading them to propose an intermediate phase that would allow for continuous dissociation. While the proposed static lattices have higher energies than *Cmca* (Edwards, Ashcroft, and Lenosky, 1996; Pickard and Needs, 2007) and $C2/c(2)$ (Liu, Wang, and Ma, 2012) (see below), such continuous structures could be stabilized by proton ZPM, which was not included in their calculations.

Recently, an alternative to AIRSS, the particle-swarm optimization (PSO) method for structure prediction (Wang *et al.*, 2010), was applied to dense hydrogen (Liu, Wang, and Ma, 2012). These calculations revealed a stable hydrogen phase beyond *Cmca* ($\sim$ 470–590 GPa). What is particularly interesting about this structure is that it possesses two different nearest-neighbor proton separations (which we refer to at these high pressures as intramolecular bonds), in a space group $C2/c(2)$ [note that we added the designation (2) to distinguish it from the $C2/c$ structure predicted for phase III]. This structure is also shown in Fig. 7. Furthermore, both bond distances are larger than the intramolecular separations in the *Cmca* structure, showing indication of molecular dissociation, and suggesting one structure (perhaps of others) that allows for the continuous dissociation mechanism suggested by Labet *et al.* (2012) and Labet, Hoffmann, and Ashcroft (2012a, 2012b, 2012c).

### 4. Melting of the molecular crystal

Significant progress was made both experimentally and computationally in determining the melting line of hydrogen, as reviewed by Silvera and Deemyad (2009). At ambient pressure, both hydrogen and deuterium crystallize in a hcp lattice at temperatures of 14 and 19 K, respectively (Silvera, 1980). Before the development of DAC techniques, measurements of the melting line (of hydrogen) were limited to pressures below $\sim$2 GPa (Liebenberg, Mills, and Bronson, 1978). Such techniques though extended the melting line to pressures above 7 GPa (Diatschenko and Chu, 1981; Diatschenko *et al.*, 1985), and the results fit well to a modified Simon equation. With improvements in static-compression techniques (see Sec. III.B), Datchi, Loubeyre, and LeToullec (2000) and Gregoryanz *et al.* (2003) were able, by monitoring the shift in the Raman-active vibron, to measure the melting line up to 15 and 44 GPa, respectively, results which are shown in Fig. 8. The latter measurements interestingly also found a decrease in the slope of the melting line with respect to pressure, suggesting a maximum in the curve. This was, in fact, indicated in earlier work by Datchi, Loubeyre, and LeToullec (2000), on the basis of an extrapolation of the Kechin melting curve, which has a maximum near 128 GPa and 1100 K.

Using constant-pressure CPMD simulations (neglecting ZPM), Scandolo (2003) predicted that the melting line at high pressures will have a negative slope, as a consequence of the LLT (see Sec. IV.B.2). Following that prediction, two-phase (solid and liquid) CPMD simulations were performed to trace the melting line to even higher pressures (Bonev *et al.*, 2004). A maximum in the melting line below 1000 K was found, as well as a negative slope that extrapolates to 0 K near 400 GPa. Of course, such extrapolations do not take into account possible phase changes in either the liquid or solid at higher pressures. These calculations were recently corroborated by Morales *et al.* (2010b) up to a pressure of 200 GPa, where the melting line of hydrogen was calculated by comparing the (DFT) Gibbs free energy of the liquid and solid molecular phases (using phase I, rotationally disordered). Recent measurements using laser heating of hydrogen in a DAC (Deemyad and Silvera, 2008) observed a maximum and subsequent decrease of the melting temperature with increasing pressure. These measurements are consistent with those reported by Eremets and Trojan

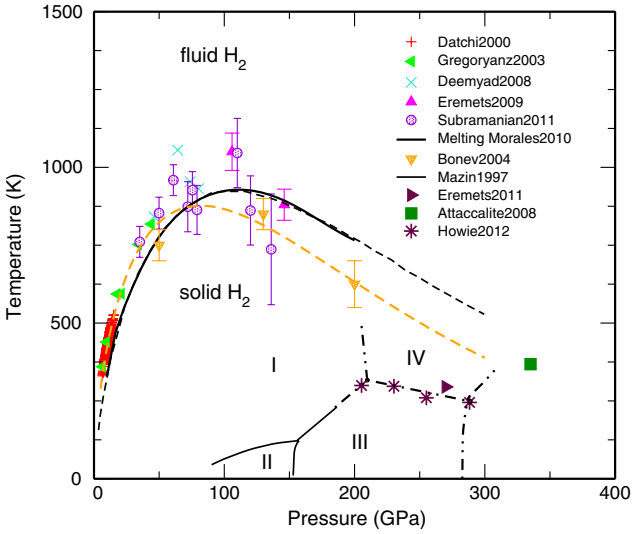


FIG. 8 (color online). Reentrant melting line of phase I of hydrogen. Experimental data: crosses (Datchi, Loubeyre, and LeToullec, 2000), left triangles (Gregoryanz *et al.*, 2003), crosses (Deemyad and Silvera, 2008), up triangles (Eremets and Trojan, 2009), and dashed circles (Subramanian *et al.*, 2011). Theoretical predictions: BOMD (triangles) (Bonev *et al.*, 2004) and free-energy calculations (solid line) (Morales *et al.*, 2010b). The dashed line at lower temperature is a fit of the Datchi, Gregoryanz and Bonev data to a Kechin equation, while the dashed line at higher temperature is a fit to the Morales data using the same functional form. A stable fluid point predicted by MD using QMC forces (square) (Attaccalite and Sorella, 2008) is also shown. Below the melting lines are the experimental solid phases (identical to Fig. 3) as well as the recently reported IM transition (Eremets and Troyan, 2011).

(2009) and Subramanian *et al.* (2011). The various measurements and theoretical predictions are shown in Fig. 8.

Comparison of the experimental data to the DFT predictions of melting for pressures between 10 and 140 GPa is a gratifying confirmation of their accuracy. However, we note that at pressures when metallization is occurring (estimated to be at about 250 GPa and 500–600 K), one expects LDA or GGA DFs in DFT to bias the results, causing the predictions to be much less accurate. Also, we note that the effect of the ZPM of the protons on the melting line tends to cancel out only if the crystal and liquid phase are both molecular or atomic. Otherwise, ZPM of the protons needs to be taken into account in determining the melting temperature. We also point out that extrapolations based on the low-pressure crystal structures are highly susceptible to error. Despite these expected inaccuracies, the Kechin equation (Kechin, 2004a, 2004b) $T_m(K) = 14.025(1 + P_m/a)^b \exp(-P/c)$ was used to extrapolate the low-pressure data to higher pressures, and in Fig. 8 two such extrapolations are reported. The first one, represented by the dashed line at lower temperature, considers experimental points from Datchi, Loubeyre, and LeToullec (2000) and Gregoryanz *et al.* (2003) as well as FPMD points from Bonev *et al.* (2004), suggesting $a = 0.030\,355$, $b = 0.599\,91$, and $c = 137$, while the second one, represented by the dashed line at higher temperature, considers only simulation results from free-energy calculations (Morales *et al.*, 2010b), which suggests $a = 0.1129$, $b = 0.7155$, and $c = 149$. What is particularly interesting about these extrapolations is that they suggest that at higher pressures, the molecular crystal phase might vanish in favor of a low- or zero-temperature fluid phase with unusual properties (see Sec. IV.C.2).

### 5. Metallization of solid molecular hydrogen

Wigner and Huntington (1935) predicted that hydrogen would undergo an IM transition at sufficiently high pressure. For the general Hamiltonian in Eq. (1), one can easily show that the potential energy scales as $r_s^{-1}$ while the kinetic energy does so as $r_s^{-2}$. Hence, as the density (and pressure) increases ($r_s \to 0$), the latter will dominate. Since the free-particle wave function minimizes the kinetic energy, this implies that any electronic system will go to an uncorrelated wave function (a simple metal). We note that at finite temperature, there is always some thermal excitation of carriers, and thus some conductivity. A precise definition of the IM transition is therefore only possible at 0 K. In a later section, we discuss the shock experiments of Weir, Mitchell, and Nellis (1996) and Nellis, Weir, and Mitchell (1999), where the IM transition was observed at high temperature ($\sim 2600$ K) and relatively low pressure ($\sim 140$ GPa) in the liquid phase; see also Maksimov and Shilov (1999) and Robitaille (2011). To determine precisely how and when hydrogen at low temperature becomes a metal has been a long-outstanding question of high-pressure physics.

The early assumption was that the IM transition would occur simultaneously with molecular dissociation (Wigner and Huntington, 1935; Abrikosov, 1954). However, Hartree-Fock calculations using the exact-exchange operator (Ramaker, Kumar, and Harris, 1975) and later band-structure calculations (Friedli and Ashcroft, 1977) suggested that metallization may instead occur directly in the molecular phase. This is because a change in density causes the molecular bands to shift, which can lead to a direct and/or indirect band-gap closure (Mazin and Cohen, 1995). This can occur when the widths of the $1\sigma_g$ and $1\sigma_u$ bands (of the molecular orbitals) become larger than their splitting, causing them to overlap. Such early predictions suggested that metallization should occur near 150 GPa, and so it was originally thought that the phase II $\to$ III transition could be the onset of it (Hanfland, Hemley, and Mao, 1993). But this is not the case, and finding it (both theoretically and computationally) remains an open problem.

Metallization of solid molecular hydrogen was reported in some experiments, such as those by Maksimov and Shilov (1999) and more recently by Eremets and Troyan (2011), the latter from DAC experiments near 300 K and 265 GPa. However, it is difficult for DAC experiments to achieve the pressures and/or temperatures required for metallization, and opinions concerning these latter results have been mixed (Jephcoat, 2011; Nellis, Ruoff, and Silvera, 2012). Moreover, near-simultaneous DAC experiments around the same thermodynamic conditions by Zha, Liu, and Hemley (2012) reported a semimetallic state, rather than a metal. At lower temperatures, however, the experimental results agree that insulating molecular hydrogen exists up to some of the highest pressure currently achievable, $\sim 320$ GPa (Goncharov *et al.*, 2001; Loubeyre, Occelli, and LeToullec, 2002). Extrapolations of optical measurements of the band gap

provide an estimate that closure should occur between 325 and 450 GPa (Goncharov *et al.*, 2001; Loubeyre, Occelli, and LeToullec, 2002). This of course assumes that there are no further crystal structure changes above 320 GPa and also that the band gap closes smoothly as a function of pressure.

Predicting the IM transition also remains challenging theoretically and computationally. The first problem arises from the ignorance of the high-pressure crystal structure, as discussed in Sec. IV.A.1. Since each structure has a much different arrangement of bands, without this knowledge, one cannot easily say much about metallization (Barbee, III *et al.*, 1989). Transition-pressure predictions have thus varied greatly, ranging, for example, from 200 to 450 GPa. Since the most recent predictions essentially agree on the *Cmca* phase (see Fig. 4) as the most likely candidate at very high pressures (Johnson and Ashcroft, 2000; Pickard and Needs, 2007; McMahon and Ceperley, 2011a), its electronic structure has been the most thoroughly examined (suggesting ~400 GPa, see below).

There are also difficulties in calculating the effects of the electron correlation and ZPM of the protons. Further, most calculations used either the LDA or GGA DFT DF, which are known to underestimate band gaps (Perdew and Levy, 1983; Sham and Schlüter, 1983) implying that the IM transition density will be underestimated (Oliva and Ashcroft, 1981a, 1981b). As discussed in Sec. II.E.1, this error is related to both the lack of the derivative discontinuity of the exchange-correlation energy and the self-interaction error. Fortunately, these errors can be reduced by using much more computationally expensive quasiparticle methods (Chacham and Louie, 1991), methods that include exact exchange (Städele and Martin, 2000), or calculations based on the many-body *GW* method (Johnson and Ashcroft, 2000). Such calculations showed that the band gaps in hydrogen are indeed underestimated by ~1–2 eV, as seen in Fig. 9. Note that even the exact-exchange calculations slightly underestimate the band gap (Jones and Gunnarsson, 1989). With these more precise estimates, the IM transition is predicted to occur near pressures of at least 400 GPa ( $\sim 0.4$ mol/cm$^3$), in agreement with experimental extrapolations (Goncharov *et al.*, 2001; Loubeyre, Occelli, and LeToullec, 2002).

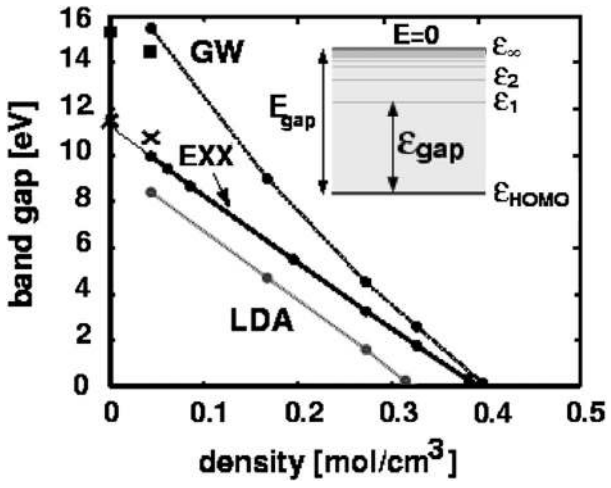


FIG. 9. Electronic band gaps for molecular hydrogen in a hcp lattice with molecules oriented along the *c* axis. No ZPM was included in these calculations. From Städele and Martin, 2000.

Another issue which has received much less attention is the effect of ZPM of the protons. If one assumes that the molecular phase has the protons confined near lattice sites, then the ZPM can be treated essentially as electron-phonon coupling. It is known that this can affect both the magnitude of the band gap and its dependence on pressure and temperature (Allen and Cardona, 1981a, 1981b). However, treating this self-consistently within the framework of DFT is currently not straightforward. One can, however, envision the possibility of such calculations using QMC and the full Hamiltonian calculations (Ceperley and Alder, 1987; Natoli, Martin, and Ceperley, 1995), which also would not suffer the band-gap problems discussed above.

### 6. Solid atomic hydrogen at low temperatures

In a landmark publication, Wigner and Huntington (1935) suggested that molecular hydrogen would dissociate to an atomic state at high pressures, and further, that any Bravais lattice of such a state would be metallic. These early predictions were that this phase would become energetically favorable at ~25 GPa. Of course, this was long before the availability of numerical methods or sophisticated high-pressure experimental techniques. Ever since this prediction, the pressure required to dissociate molecular hydrogen has been pushed ever upward, and the transition to the atomic lattice is yet to be observed. Recent predictions (Pickard and Needs, 2007; McMahon and Ceperley, 2011a; Liu, Wang, and Ma, 2012) suggest that at least ~500 GPa will be necessary.

The most fundamental property, that one must know to base further predictions on, is the crystal structure. Naively, one might expect hydrogen to assume a relatively simple structure, because at high pressures, as discussed in Sec. IV.A.5, the system will become a free-electron metal (Ashcroft and Mermin, 1976). At sufficiently high pressures, the lattice of protons will interact with the bare, unscreened Coulomb potential; and, as is well known, the structure minimizing the Coulomb potential is the body-centered cubic (bcc) lattice, which was thus the primary structure considered by Wigner and Huntington (1935).

However, it has turned out that the alkali metals, such as lithium and sodium, that are free electronlike already at ambient conditions, and should become even more so under pressure, exhibit rather exotic and complex pressure-induced structural transitions (Rousseau *et al.*, 2011). The simple scaling argument in fact fails, because even a small amount of electronic screening of the proton-proton interaction is enough to destabilize the bcc lattice. It is thus reasonable to expect that atomic hydrogen will undergo an analogous and complex sequence of phase transitions as a function of both pressure and temperature.

Many studies considered anisotropic structures, such as layered ones (Brovman, Kagan, and Kholas, 1972a; Kagan, Pushkarev, and Kholas, 1977), reminiscent of the graphite-type structure also considered by Wigner and Huntington (1935), or filamentary ones (Ebina and Miyagi, 1989; Nagara, 1989). Anisotropic structures were also considered by Barbee, III *et al.* (1989) and Barbee, III and Cohen (1991), the latter study drawing a structural analogy with the 9*R* ground-state structure of ambient-pressure lithium (Overhauser, 1984). Many other studies, however, focused

primarily on isotropic structures (Straus and Ashcroft, 1977; Ceperley and Alder, 1987; Natoli, Martin, and Ceperley, 1993; Nagao, Nagara, and Matsubara, 1997).

As discussed in Sec. II.E.2 and emphasized in previous sections, a central challenge to modeling hydrogen is the accurate treatment of proton ZPM. While the simple harmonic approximation, Eq. (40), continues to be used to study atomic hydrogen (Pickard and Needs, 2007; McMahon and Ceperley, 2011a; Liu, Wang, and Ma, 2012), Straus and Ashcroft (1977) demonstrated, using a family of face-centered tetragonal structures, similar, in fact, to those considered again in a later study by Nagao, Nagara, and Matsubara (1997), that this can easily fail. Only by including anharmonicity, for example, were some structures found to be energetically stabilized, such as the isotropic fcc structure. Later $T = 0$ K QMC calculations by Natoli, Martin, and Ceperley (1993) confirmed the basic idea behind these findings, demonstrating that a full account of ZPM indeed favors isotropic structures.

Following more recent advancements in structure prediction methods (Woodley and Catlow, 2008), as discussed, McMahon and Ceperley (2011a) considered atomic hydrogen, predicting a large number of previously unidentified structures. Their work suggested that after molecular dissociation, hydrogen should adopt a structure similar to the fourth phase of cesium, a body-centered tetragonal structure with space group $I4_1/amd$ and a $c/a$ ratio greater than unity, consistent with earlier predictions (Nagao, Nagara, and Matsubara, 1997; Pickard and Needs, 2007) and structure-searching calculations that followed based on the PSO method (Geng *et al.*, 2012). This structure was found to be stable at least up to ~1 TPa, when including a harmonic estimation of ZPE.

Recently, Liu, Wang, and Ma (2012) also applied the PSO method to the atomic phase of hydrogen, predicting two structures not found in the earlier searches at very high pressures (i.e., beyond the stability range of $I4_1/amd$). Above 2.1 TPa, atomic hydrogen was found to likely adopt a structure consisting of planar $H_3$ clusters and space group $Cmcm$, as shown in Fig. 10. This structure is in fact analogous to the enthalpically favored static-lattice structure $R3m$ predicted by McMahon and Ceperley (2011a) at such pressures, but allows for a more efficient packing. Liu, Wang, and Ma (2012) also suggested that above 3.5 TPa, a structure similar to a distorted bcc lattice with space group $I$-43$d$, also shown in Fig. 10, would become stabilized by proton ZPM (albeit, within the harmonic approximation).

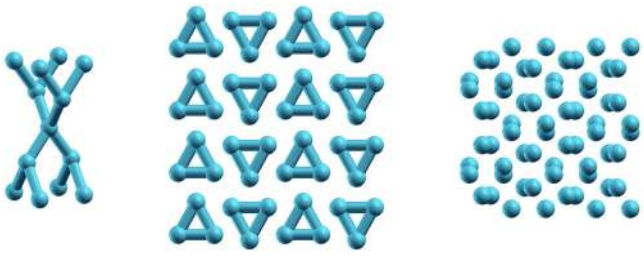

FIG. 10 (color online). Predicted ground-state structures of atomic metallic hydrogen: (left) $I4_1/amd$ at 500 GPa (Nagao, Nagara, and Matsubara, 1997; Pickard and Needs, 2007; McMahon and Ceperley, 2011a), (middle) $Cmcm$ at 2.5 TPa (Liu, Wang, and Ma, 2012a), and (right) $I$-43$d$ at 3.5 TPa (Liu, Wang, and Ma, 2012). Fictitious bonds are drawn between nearest neighbors.

At very, very high pressures (and relatively low temperatures), it is expected that atomic hydrogen will adopt a close-packed lattice, such as fcc or hcp (Kohanoff and Hansen, 1996). In this regime, one can "integrate out" the electrons and use a screened pair potential between the protons, as discussed in Sec. II.G.1. The validity of this screened Coulomb plasma (SCP) model in this regime ($r_s \leq 0.6$, $P \geq 20$ TPa) was established by comparing against both CPMD predictions (Kohanoff and Hansen, 1996) and more accurate CEIMC calculations (Pierleoni *et al.*, 2008; Liberatore, Pierleoni, and Ceperley, 2011).

We note that free-energy calculations (Liberatore, Pierleoni, and Ceperley, 2011) of the SCP at ~24 TPa give an estimated melting temperature of 1670 K. This is quite interesting, because if the melting temperature is low enough, an interesting quantum fluid could be stable. We return to this in Sec. IV.C.2.

### B. The normal fluid phase

While an understanding of the low-temperature region of the phase diagram of hydrogen is certainly important for fundamental reasons, the major fraction of hydrogen in the Universe is in the fluid phase at higher temperatures. What is necessary under these conditions is an accurate EOS that can be used for both planetary models and to validate computational assumptions and experimental procedures. Theoretical and computational methods progressed to the point where sufficient accuracy can now be obtained to resolve such issues. In this section, we first discuss first-principles calculations applied to the fluid phase of hydrogen, with particular focus on predicting the principal Hugoniots of hydrogen and deuterium, and then focus on the LLT.

#### 1. The equation of state and principal Hugoniot of hydrogen

The EOS of hydrogen in the fluid phase is particularly relevant for planetary and ICF physics (see Fig. 1). As discussed in Sec. III, experimental information for the liquid phase of hydrogen comes mainly from dynamic-compression experiments, with the exception of the low-temperature liquid near the melting line which can be studied using static-compression techniques. Particularly useful properties such as the electrical conductivity or reflectance can be measured during the experiment and are difficult to compute with simulations. However, dynamic-compression methods have large uncertainties in determining the pressure, and, particularly, the temperature of the sample after the shock, and, therefore, obtaining precise thermodynamic data. Also, since the experiments are difficult and rather expensive, the reached set of temperature-density points is rather sparse. Because of this, first-principles simulation methods are useful to complement the experimental data.

Early shock wave experiments on hydrogen and deuterium samples were done with a gas-gun compression method (van Thiel and Alder, 1966; van Thiel *et al.*, 1973) up to pressure of 20 GPa in the first shock and 90 GPa in the reflected shock, and by laser-driven compression methods (van Kessel and

Sigel, 1974) up to pressures of ~200 GPa in a single-shock experiment. Soon after, the first measurements of electrical conductivity in isentropically compressed hydrogen in a magnetic-flux compression device appeared (Hawke *et al.*, 1978) which reported a measured drop of electrical resistivity below 1.0 Ω cm at a density of 1.06 g/cm$^3$ and an estimated pressure of 200 GPa. Continuous progress in the experimental techniques provided better data for the first (single-shock) Hugoniot up to 20 GPa and the second (reflected-shock) Hugoniot (Nellis, Mitchell *et al.*, 1983; Nellis, Ross *et al.*, 1983) up to 76 GPa; see Fig. 11. However, the temperature was not measured; the estimated temperature was based on a phenomenological chemical model of fluid hydrogen (Kerley, 1972; Ross, Ree, and Young, 1983). By measuring the electrical conductivity in the deuterium and hydrogen shocked samples (Nellis *et al.*, 1992), it was inferred that, below 20 GPa, shocked fluid deuterium behaves as a hot semiconductor with a band gap of ~12 eV.

After the introduction of FPMD methods (Car and Parrinello, 1985) for studying *s*-*p* bond materials, application to high-pressure hydrogen with an orbital-free method was made by Zerah, Clerouin, and Pollock (1992) and by a ground-state DFT-LDA Car-Parrinello calculation (Hohl *et al.*, 1993). This was subsequently followed by several

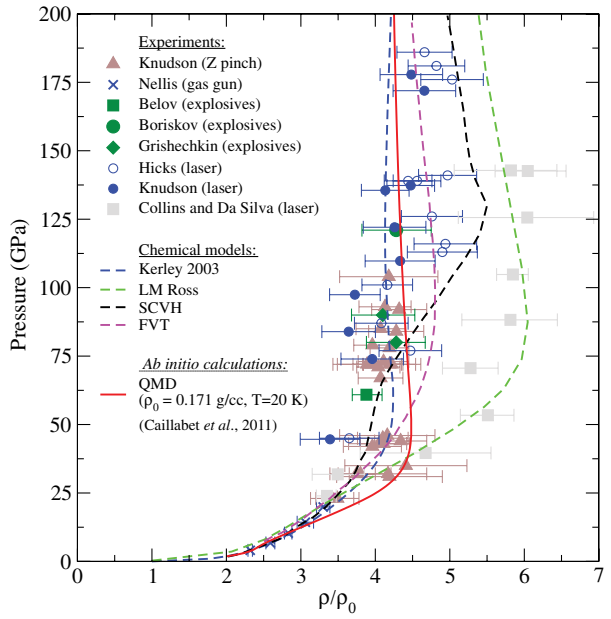


FIG. 11 (color online). Comparison between the measured and calculated principal Hugoniot for deuterium. The experimental data are plotted as symbols with error bars: *Z* machine (triangles) (Knudson *et al.*, 2004), gas gun (crosses) (Nellis, Ross *et al.*, 1983), explosives (dark squares) (Belov *et al.*, 2002), (large circles) (Boriskov *et al.*, 2003), (diamonds) (Grishechkin *et al.*, 2004a), and laser (open circles) (Hicks *et al.*, 2009), (filled small circles) (Knudson and Desjarlais, 2009), and (light squares) (Da Silva *et al.*, 1997; Collins, Da Silva *et al.*, 1998). The continuous line is the Hugoniot from Caillabet, Mazevet, and Loubeyre, 2011. Predictions of various chemical models are reported as dashed lines (from left to right): Kerley (Kerley, 2003), FVT (Juranek and Redmer, 2000), Saumon–Chabrier–van Horn (Saumon, Chabrier, and Horn, 1995), and Ross (Ross, 1998). From Caillabet, Mazevet, and Loubeyre, 2011.

studies including thermal effects on the electrons using the Mermin functional (Alavi *et al.*, 1994; Kwon *et al.*, 1994, 1995; Kwon, Kress, and Collins, 1994; Collins *et al.*, 1995; Kohanoff and Hansen, 1995, 1996) and an inclusion of excited states within the time dependent density functional theory LDA framework by Theilhaber (1992). These calculations were plagued by systematic errors due to limitations of the LDA energy functional and of small system sizes, in particular, in the metallic phase. Almost in parallel, the first RPIMC calculations of the EOS and the liquid-liquid phase transition (see Sec. IV.B.2) in high-pressure hydrogen appeared (Pierleoni *et al.*, 1994, 1996; Magro *et al.*, 1996). While FPMD studies concentrated on a density range above the density of the principal Hugoniot, RPIMC results, limited to temperature above 5000 K, also probed the region of phase space of the principal Hugoniot. RPIMC found a nonmonotonous behavior of the pressure versus density along the Hugoniot which was interpreted as the signature of a first-order phase transition between a molecular fluid and an atomic fluid. Unfortunately, in this first implementation of RPIMC, systematic effects due to system size and imaginary-time step errors limited the accuracy of the results. Wave-packet MD was also applied to high-pressure hydrogen (Klakow, Toepffer, and Reinhard, 1994a, 1994b). In this method, electrons are represented by single-electron Gaussian wave packets; Ehrenfest dynamics is used to simulate the electronic dynamics and to extract the forces acting on the protons. The approach is, however, limited to the semiclassical regime since Fermi statistics is only accounted for approximately and its applicability to the phenomena of molecular dissociation and metallization is only qualitative.

Holmes, Ross, and Nellis (1995) and Nellis, Weir, and Mitchell (1996) directly measured the temperature along the Hugoniot by fitting the radiance of the light emitted from the shocked sample to a gray-body Plank spectrum; see Fig. 12. They found temperatures substantially lower than predicted by the employed chemical model, with an increasing discrepancy with increasing pressure. This was interpreted as an indication of a substantial molecular dissociation above 20 GPa.

Principal Hugoniot pressures up to ~340 GPa were later achieved with a pulsed laser-produced shock compression (Da Silva *et al.*, 1997; Collins, Da Silva *et al.*, 1998; Celliers *et al.*, 2000); see Fig. 11. Those experiments reported a much higher compressibility, and therefore, higher shock density, up to a sixfold compression ($\rho/\rho_0 \sim 6$), higher than expected by the standard EOS (Kerley, 1972) which does not include molecular dissociation. Such a high compression would have a dramatic effect on the efficiency of inertial confined fusion. The unexpected compression was not incompatible with some existing theoretical predictions and models which allowed for molecular dissociation. Note that at sufficiently high pressure, the compression on the principal Hugoniot must attain the ideal gas value of 4 (Nellis, 2006a). Along the Hugoniot the system was observed, by optical reflectivity measurements (Celliers *et al.*, 2000), to undergo a continuous insulator-to-metal transition in the region from 17 to 50 GPa as inferred by a continuous increase in the reflectance signal (from 10% to 50%) and a saturation at higher pressures. Temperature was determined by pyrometric

measurements (Collins, Celliers *et al.*, 2001) and was found to increase from 0.47 to 4.4 eV (5000–50 000 K) in the pressure range from 31 to 230 GPa (see Fig. 12). This temperature is smaller than the Fermi temperature of the metallic fluid ( $\sim$ 16 eV), and the samples are a degenerate metal. Improvement in compression (up to $\sim$12-fold), with pressures up to 600 GPa, has been reported in reflected-shock experiments where the second shock occurs at $\sim$100 GPa along the primary Hugoniot line (Mostovych *et al.*, 2000, 2001). However, the temperature was not measured during these experiments. The results were again in close agreement with phenomenological models including molecular dissociation.

These experiments stimulated new first-principle simulation studies. Attempts to compute the electrical conductivity appeared (Pfaffenzeller and Hohl, 1997). This study found a more pronounced metallicity and atomic character than reported in the experiments probably attributable to the use of LDA. Further tight-binding MD found a principal Hugoniot in substantial agreement with the gas-gun data below 20 GPa but could not reproduce the laser-driven data at higher pressure (Lenosky, Kress, and Collins, 1997; Lenosky *et al.*, 1997a, 1997b, 1999). Two independent *ab initio* MD studies using DFT with gradient corrected exchange-correlation functional (GGA) were performed (Galli *et al.*, 2000; Lenosky *et al.*, 2000; Collins, Bickham *et al.*, 2001). A further study which exploited the LSDA in the FPMD was also performed (Bagnier, Blottiau, and Clérouin, 2000). The results of the three studies were all in agreement and supported a maximum compression of $\sim$4.4 in the region of 50 GPa, with a limiting compression for higher pressure around 4 in substantial disagreement with the laser-driven Hugoniot. On the other hand, the computed optical reflectivity was in good agreement with the measurements performed during the laser-driven runs up to 70 GPa (Collins, Bickham *et al.*, 2001). The system was found to smoothly dissociate along the Hugoniot reaching a value of the electrical conductivity of 4000 $(\Omega\,\mathrm{cm})^{-1}$ at maximum compression. Improved RPIMC simulation was also performed with smaller time step and finite-size errors and a better nodal restriction taking into account bound states (Militzer and Ceperley, 2000). As seen in Fig. 13, this calculation provided an almost vertical Hugoniot with maximum compression of $4.3 \pm 0.1$ also in disagreement with laser-driven shock experiments. In a subsequent study combining RPIMC ($T > 10^5$ K) and first-principles MD ($T < 10^5$ K) simulation techniques (Militzer *et al.*, 2001), the secondary Hugoniot was investigated and results compared with the experimental data of Mostovych *et al.* (2000, 2001). Even in this case it was found that RPIMC and AIMD were in essential agreement but both at variance with the secondary Hugoniot from laser-driven experiments.

Magnetic implosions at the $Z$ pinch were then used to create shock waves in much larger samples of liquid deuterium (Knudson *et al.*, 2001). Pressures of $\sim$70 GPa were

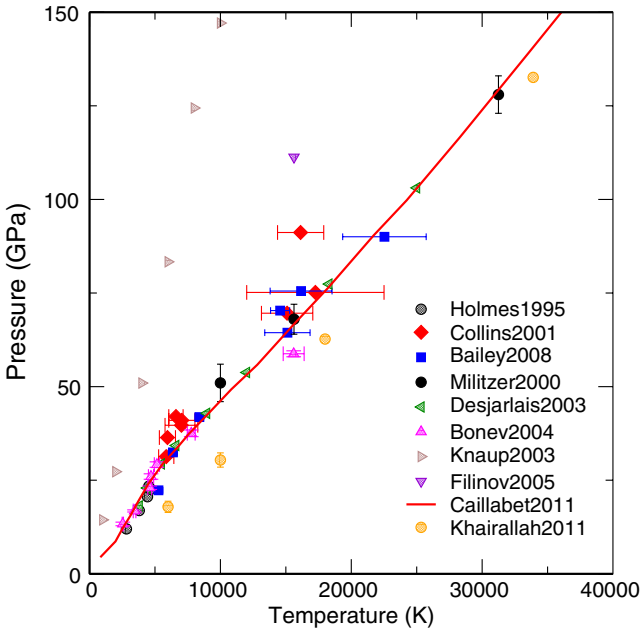


FIG. 12 (color online). Pressure vs temperature along the Hugoniot. Comparison among experimental data and various theoretical predictions. Experiments: gas-gun [shaded circles (Holmes, Ross, and Nellis, 1995)], Nova laser [diamonds (Collins, Celliers *et al.*, 2001)], $Z$ pinch [squares (Bailey *et al.*, 2008)]. Theory: RPIMC [closed circles (Militzer and Ceperley, 2000), light shaded circles (Khairallah, Shumway, and Draeger, 2011)], BOMD [left triangle (Desjarlais, 2003), up triangle (Bonev, Militzer, and Galli, 2004), line (Caillabet, Mazevet, and Loubeyre, 2011)], direct PIMC [down triangle (Filinov *et al.*, 2005)] and WPMD [right triangle (Knaup *et al.*, 2003)].

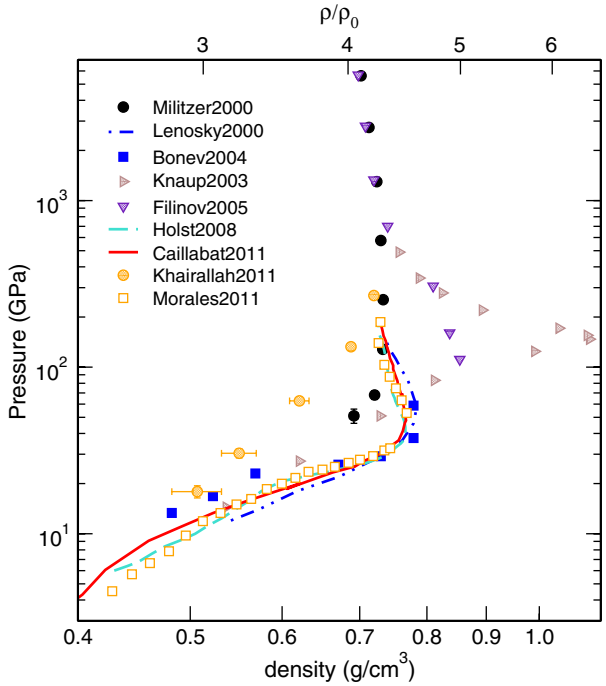


FIG. 13 (color online). Comparison among various theoretical methods of computations of the principal Hugoniot for deuterium. RPIMC (dark closed circles) (Militzer and Ceperley, 2000), (light closed circles) (Khairallah, Shumway, and Draeger, 2011) and direct PIMC (down triangles) (Filinov *et al.*, 2005). FPMD ground-state electrons (double dot-dashed line) (Lenosky *et al.*, 2000), (closed squares) (Bonev, Militzer, and Galli, 2004b) and thermal electrons (dashed line) (Holst, Redmer, and Desjarlais, 2008), (continuous line) (Desjarlais, 2003; Caillabet, Mazevet, and Loubeyre, 2011) and (open squares) (Morales *et al.*, 2012). WPMD (right triangle) (Knaup *et al.*, 2003).

achieved with a 4.0–4.5-fold compression, in contrast to the 6-fold compression observed in the laser-driven experiments; see Fig. 11. These data are in much closer agreement with the first-principle predictions of RPIMC and FPMD. Finally, a new technique based on spherically converging shock waves generated by explosives (Belov *et al.*, 2002) (data reported in Fig. 11) also produces lower compressions.

A subsequent refinement of the detection technique of the magnetic pressure apparatus (Knudson *et al.*, 2003) and further experiments (Knudson *et al.*, 2004) measured the principal Hugoniot up to 100 GPa confirming a maximum compression of ~4.3 (see Fig. 11) and provided data along the second-shock Hugoniot up to 400 GPa and final density of deuterium of 1.34 $g/cm^3$. In those experiments, temperature was not measured but later experiments using reflectivity and emissivity, to infer the temperature (Bailey *et al.*, 2008), are shown in Fig. 12, and found to be in good agreement with previous data. Also, second-shock data up to 900 GPa have been measured with laser-driven shocks at the OMEGA laser in Rochester (Boehly *et al.*, 2004). These data are consistent with a stiff EOS with 4.3- to 4.4-fold maximum compression along the principal Hugoniot. A further experimental confirmation of a stiff EOS along the principal Hugoniot came from converging explosive-driven shock waves (Grishechkin *et al.*, 2004a; Boriskov *et al.*, 2005); see Fig. 11.

Recently, new laser-driven experiments using impedance matching to an aluminum standard were performed (Hicks *et al.*, 2009). At variance with previous experiments, they found 4.2-fold compression for pressures near 100 GPa, in agreement with other experiments based on the impedance matching method. However, just above 100 GPa and up to the highest reached pressure (220 GPa), a sudden jump to higher compression ( $\sim 5$) was observed, but soon after (Knudson and Desjarlais, 2009), it was shown that this behavior was caused by an erroneous calibration of the quartz impedance matching standard used to infer the principal Hugoniot above 100 GPa. At present, after 20 years of effort, a consensus is emerging on the principal Hugoniot of deuterium obtained by several different experimental methods and teams.

While most previous experimental work has been on deuterium samples, a recent experiment using laser-driven shock waves (Sano *et al.*, 2011a) measured shocked hydrogen in the pressure range between 25 and 55 GPa. The lower pressure data are in agreement with previous experiments (Dick and Kerley, 1980; Nellis, Mitchell *et al.*, 1983) and at higher pressures they show a compression of ~5, which suggest that hydrogen is more compressible than deuterium. However, the measured temperature is higher in hydrogen by a factor of ~1.3.

In parallel with advances in experimental methods and results, first-principle methods have also been improved and extended. At the turn of the century, two FPMD studies investigated some of the systematic errors: the first used Born-Oppenheimer dynamics with thermal electrons (Desjarlais, 2003) while the second used Car-Parrinello dynamics with ground-state electrons (Bonev, Militzer, and Galli, 2004). As seen in Fig. 13 consistent results were obtained. The computed Hugoniot was slightly stiffer than in a previous work (Lenosky *et al.*, 2000) but still had a maximum compression of about 4.5 at ~40 GPa, and in agreement with the gas-gun $Z$-pinch experiment up to 20 GPa (Knudson *et al.*, 2001). Above this pressure, the new theoretical Hugoniot was slightly stiffer than the experimental data. Also, the predicted temperature along the Hugoniot for $P \leq 20$ GPa was found to be in very good agreement with the experimental gas-gun data (see Fig. 12). In contrast, previous first-principle studies predicted temperatures smaller by as much as 30% (Lenosky *et al.*, 2000). Several later BOMD simulations using DFT-GGA confirmed these results: Vorberger, Tamblyn, Militzer, and Bonev (2007) were limited to lower temperatures, used ground-state electrons, and investigated the hydrogen-helium mixture (see Sec. V), and Holst, Redmer, and Desjarlais (2008) used thermal electrons and computed optical properties such as reflectivity and conductivity (see below).

We also mention a number of theoretical investigations which predicted a soft principal Hugoniot. The first study was performed by wave-packet molecular dynamics (WPMD) (Knaup *et al.*, 2003) and reported a principal Hugoniot with a maximum compression of ~6 in agreement with the Nova laser data (see Fig. 13). The accuracy of the WPMD is, however, limited to the semiclassical regime and should not be applied at these temperatures. Also, the predicted temperature was considerably lower than in the experiments and in the first-principle methods. The second study employed the DPIMC method (Filinov *et al.*, 2005) and reported a maximum compression of ~5 at $P = 111$ GPa, providing a softer EOS with respect to the RPIMC predictions of Militzer and Ceperley (2000); see Fig. 13. Also in this method, the temperature along the Hugoniot was substantially lower than in experiments and in other first-principle methods (see Fig. 12). Finally, we mention a recent investigation of the principal Hugoniot by the antinodal-slice RPIMC method (Khairallah, Shumway, and Draeger, 2011) (see Sec. II.C). They obtain good agreement with the previous RPIMC Hugoniot at high pressure ($P \geq 200$ GPa) and a stiffer Hugoniot at lower pressure, but still compatible with the experimental data within their large uncertainty (see Fig. 13). However, these results do not agree well with the low-pressure gas-gun data. Also, as seen in Fig. 12, the predicted temperature along the Hugoniot is somewhat higher than the experimental measurements and the predictions from RPIMC and FPMD.

As seen in Fig. 11, the uncertainty on the experimental data is large, which makes it difficult to discriminate between different calculations. On the other hand, the most recent FPMD calculations of the principal Hugoniot give similar results and are in agreement with the experimental data, reinforcing the consensus on the experimental Hugoniot.

Validation of the FPMD predictions can be obtained either by comparing with experimental data or by comparing to results from a more fundamental method such as CEIMC. The two methods solve the electronic problem in very different ways and with different approximations: CEIMC is based on the variational principle (with respect to the nodes of the trial wave function) and can be systematically improved. CEIMC is a relatively recent method, rather more demanding than FPMD, and therefore its applications have been limited so far. Moreover, earlier implementations were plagued by insufficient accuracy of the trial wave function and gave results in disagreement with CPMD

(LDA) predictions at higher density around the melting transition of the atomic metallic crystal ($0.8 \leq r_s \leq 1.2$, $500 \leq T \leq 10\,000$ K) (Pierleoni, Ceperley, and Holzmann, 2004). Recent methodological progress, in particular, the implementation of LDA-KS orbitals in the Slater determinant of the trial wave function, considerably improves the accuracy and the flexibility of the method (Pierleoni *et al.*, 2008) and provides results for the hydrogen EOS which are in good agreement with the predictions of FPMD (Pierleoni *et al.*, 2008; Morales, Pierleoni, and Ceperley, 2010a). Morales, Pierleoni, and Ceperley (2010a) compared the EOS from both methods in the region $2000 \leq T \leq 10\,000$ K and $0.724 \leq \rho \leq 2.329$ g/cm$^3$ ($1.55 \geq r_s \geq 1.05$), corresponding to $100 \leq P \leq 2000$ GPa, a small region slightly to the right of the first Hugoniot (see Fig. 1) and relevant in modeling the Jovian planets. The pressure difference between the two methods was at most 5% at the lowest density (approaching the molecular dissociation regime) and decreases with increasing density. The difference in the internal energy ($\sim 0.8\%$) appears to be uniform with density. Also, predictions for the local structure of the proton fluid are in very good agreement. As seen in Sec. IV.B.2, this agreement is not observed at the metal-insulator transition underlying again the nontrivial character of this finding. Our present understanding is that DFT-based FPMD is quite accurate in comparison to CEIMC, both at high pressure and at low pressure in regions away from the metal-insulator transition. In the region where the system becomes metallic the local and semilocal functionals have a well-known problem of underestimating the band gap and FPMD provides wrong predictions: see below.

Most of the theoretical studies discussed so far concentrated on computing the first and second Hugoniots. Recently, first-principle calculations have been performed over a much wider region in thermodynamic space (Caillabet, Mazevet, and Loubeyre, 2011; Hu *et al.*, 2011; Morales *et al.*, 2012) to build a thermodynamically consistent EOS for conditions appropriate to planetary models and ICF applications. Morales *et al.* (2012) used both FPMD and CEIMC to study the EOS in the range $10 \leq P \leq 1000$ GPa, $3000 \leq T \leq 35\,000$ K. It was found that the Kerley (2003) EOS works well after a pressure dependent, but temperature independent, correction is applied. Hu *et al.* (2011) employed RPIMC to map the EOS in the range $0.002 \leq \rho \leq 1596$ g/cm$^3$, $10^4 \leq T \leq 10^8$ K. The RPIMC-based EOS is in good agreement with the Kerley (2003) table. We note that an earlier PIMC calculation of the low density phase diagram of hydrogen (Militzer and Ceperley, 2001) reported a substantial agreement between PIMC data for the EOS and the Saumon-Chabrier chemical model predictions. On the other hand, in the higher pressure range investigated by Morales, Pierleoni, and Ceperley (2010a) ($100 \leq p \leq 2000$ GPa) the modified SCVH EOS (Saumon, Chabrier, and Horn, 1995) was found to deviate from the CEIMC data by as much as ~25% at the edge of the dissociation region, the region in which chemical models are essentially based on interpolations. Because planetary models are sensitive to details in this regime and at lower pressures during dissociation, a deviation from SCVH will produce a much larger change; e.g., it is found using a less compressible EOS that Jupiter has a core mass of 14–18 Earth masses, much larger than the SCVH value of 0–7 Earth masses (Guillot, 2005; Militzer *et al.*, 2008). However, a consensus on the interior model for Jupiter and the EOS has yet to be reached.

### 2. Liquid-liquid phase transition (LLPT)

Fluid hydrogen at low pressure is $H_2$; molecular dissociation will occur both with increasing temperature or with pressure. At moderate pressures ($\sim 10^2$–$10^4$ bar), molecular dissociation happens when the temperature is approximately equal to the molecular bonding energy ($\sim 4.5$ eV). The dissociation temperature depends mildly on pressure since internal degrees of freedom (either molecular or atomic) are largely independent of pressure as shown in Fig. 2. This prediction is based on chemical models which are expected to be accurate at low density (Saumon, Chabrier, and Horn, 1995; Hu *et al.*, 2011). On the other hand, with increasing pressure at moderate temperature ($T \sim 1000$ K), the physics becomes more complex because the separation between internal degrees of freedom and many particle interactions disappears; the internal states of the molecules are strongly influenced by molecule-molecule interactions, and, for high enough pressure, molecules dissociate and the system becomes metallic.

Whether dissociation and metallization occur at the same time and whether the processes are continuous are open questions with recent experimental and theoretical findings. The occurrence of metallization induced by pressure was discussed by Wigner and Huntington (1935) for atomic hydrogen at $T = 0$ K, by Landau and Zeldovich (1943) for liquid mercury as a first-order phase transition, and by Norman and Starostin (1970) for a dense atomic plasma. In high-pressure fluid hydrogen, molecular dissociation and ionization was discussed by Ebeling and Richert (1985, 1985) and later by Marley and Hubbard (1988), Saumon and Chabrier (1989, 1991, 1992), Kitamura and Ichimaru (1998), Beule *et al.* (1999), Fortov *et al.* (2003), Edwards *et al.* (2010), and Redmer and Holst (2010) at several levels of sophistication in the framework of chemical models. These models exhibit a clear first-order LLT that persists for temperatures well above 10 000 K. However, approaches with separate free-energy functionals in different regions of phase space have great difficulty in having a continuous crossover from one behavior to another. The presence of a first-order phase transition in the chemical models is now recognized to be an artifact of the method (Chabrier, Saumon, and Winisdoerffer, 2007). Recent EOS tables now smooth the pressure in the transition region to ensure positive compressibility (Saumon, 2007).

Nellis, Weir, and Mitchell (1996) and Weir, Mitchell, and Nellis (1996) [see also Nellis, Weir, and Mitchell (1999)], using reverberating shocks to achieve quasi-isoentropic compression up to 180 GPa, found that the resistivity decreased by almost 4 orders of magnitude in a continuous manner (Nellis *et al.*, 1998) between 93 and 140 GPa, and then saturated to roughly 500 $\mu\Omega$ cm between 140 and 180 GPa, a typical resistivity value for liquid metals. They estimated the temperature from a model at 140 GPa to be ~3000 K as

shown in Fig. 14. They estimated the molecular dissociation to be ~5%: the system is still largely molecular.

Recently, Fortov *et al.* (2007), using reverberating shocks, ramp compressed hydrogen with high explosives and found a discontinuous behavior at the metal-insulator transition. Using highly resolved flash x-ray diagnostics, they were able to measure the compressibility of the liquid and found a 20% increase in density in the regime where the conductivity increases by ~5 orders of magnitude. The temperature was not measured directly but inferred from a chemical model EOS to be in the range of 3000–8000 K. The two data points around the density discontinuity [using the EOS from a recent FPMD study (Tamblyn and Bonev, 2010a)] are shown in Fig. 14. However, the measurements from this experiment were sparse in density and a rapid, yet continuous, change in conductivity with increasing pressure could not be ruled out from the data.

The first *ab initio* evidence of a first-order phase transition came from a restricted PIMC calculation (with free-particle trial nodes) showing an abrupt pressure change along isotherms (Magro *et al.*, 1996) with a critical point at $T_c \simeq 11\,000$ K, $P_c \simeq 48$ GPa in qualitative agreement with prediction by chemical models. However, the RPIMC method has

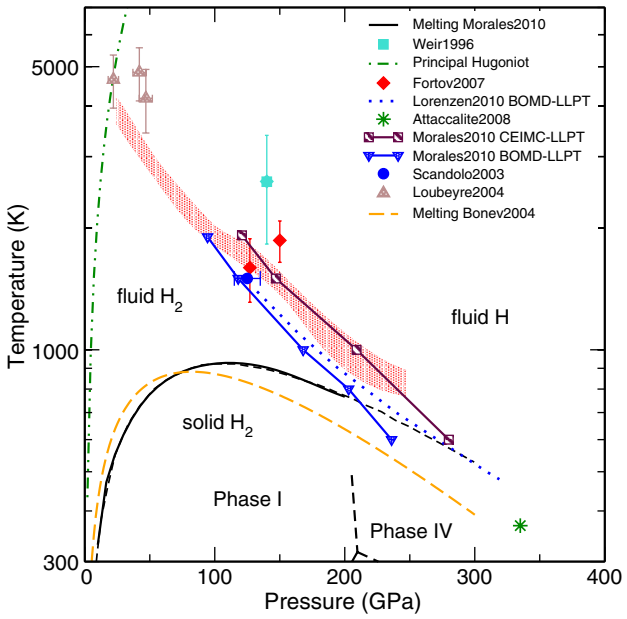


FIG. 14 (color online). Liquid-liquid transition line and pressure dissociation region. Experimental data for metallic hydrogen: [square (Nellis, Weir, and Mitchell, 1996; Weir, 1998), diamonds (Fortov *et al.*, 2007), triangles (Loubeyre *et al.*, 2004)]. Theoretical predictions for the LLPT: [downward triangle BOMD) (Morales *et al.*, 2010b) and (squares CEIMC (Morales *et al.*, 2010b; Liberatore *et al.*, 2011)]. The lines are a guide to the eye through BOMD and CEIMC simulation data, respectively. [Circle (Scandolo, 2003), dotted line (Lorenzen, Holst, and Redmer, 2010)]. Molecular dissociation region according to BOMD: shaded area (Tamblyn and Bonev, 2010a). Primary Hugoniot: thick double-dot-dashed line. QMC prediction of stable fluid state: star (Attaccalite and Sorella, 2008). Melting curve of the molecular solid (phase I) is represented by two possible curves as discussed in Sec. IV.A.4: solid (upper dashed) line (Morales *et al.*, 2010b), lower dashed line (Bonev *et al.*, 2004a). The expected boundary between phase I and phase IV is also reported (Howie *et al.*, 2012).

major problems with convergence at temperatures below 10 000 K and that calculation was plagued by finite imaginary-time step errors.

The next step toward the present understanding of liquid-liquid phase transition in hydrogen came from a CPMD (using DFT-GGA energy functional) and classical protons (Scandolo, 2003) in the constant-pressure ensemble. A first-order phase transition was signaled by large density fluctuations at $T = 1500$ K and $P = 125$ GPa with a 6% change of specific volume. At the transition, a rapid molecular dissociation was observed and the system became metallic with the gap at the Fermi level closing, both molecular dissociation and metallization of hydrogen occurring together with a first-order phase transition. This result is not in contradiction with the dynamical compression experiments of Nellis, Weir, and Mitchell (1996) and Weir, Mitchell, and Nellis (1996) but requires the existence of a critical temperature between 1500 and 3000 K. Note that the temperature in the shock experiments was estimated by an indirect method. Also, the transition pressure of first-principle DFT-GGA simulations is somehow lower than measured in the experiments; see Fig. 14. Evidence of a first-order liquid-liquid phase transition was also found by Bonev *et al.* (2004) and Bonev, Militzer, and Galli (2004) using the CPMD method with the GGA functional in the NVT ensemble at pressures of 200 GPa and temperatures between 900 and 1000 K. But a smooth dissociation process under pressure was found in subsequent BOMD investigations (Vorberger, Tamblyn, Bonev, and Militzer, 2007; Vorberger, Tamblyn, Militzer, and Bonev, 2007; Holst, Redmer, and Desjarlais, 2008). A region with $(\partial P/\partial T)_\rho < 0$ along isochores inside the dissociation region ($P \simeq 200$ GPa, $1000 \leq T \leq 4000$ K) was reported without a density discontinuity but a continuous crossover from an insulating to a conducting state.

Similarly, a CEIMC simulation (Delaney, Pierleoni, and Ceperley, 2006) reported no evidence for a first-order phase transition at $T = 1500$ and 2000 K in the pressure range from 135 to 290 GPa. In this work, the trial wave function had a Slater determinant using the orbitals from a band-structure solution with an effective electron-proton potential. Employing VMC energies along the isotherm at $T = 2000$ K, a jump in the molecular fraction was observed when increasing density around 220 GPa with an hysteresis when releasing the density. However, when using RQMC energies at the same conditions, the molecular fraction presented a much smoother behavior with density, suggesting a continuous dissociation process.

Finally, a convincing demonstration of the first-order liquid-liquid phase transition was found by Morales *et al.* (2010b) and Liberatore *et al.* (2011) exploiting both BOMD and CEIMC (see Fig. 14). The signature of the first-order character of the transition is a plateau in $P$ vs $\rho$ along isotherms for temperatures below $\approx 2000$ K. Both methods saw a density discontinuity at the transition of $\approx 2\%$, sufficiently small that a quick scan of this region, as done in previous simulations and experiments, could miss the discontinuity. However, the determined transition pressures with BOMD are $\approx 20\%$ smaller than with CEIMC because of the band-gap problem of local or semilocal density functionals. Inclusions of quantum proton effects within the

DFT-GGA method, as obtained by PIMD, produce a further 25% decrease of the transition pressure at the same temperature, because of the importance of nuclear zero-point motion at the transition; the kinetic energy of protons is higher in the molecular-rich phase than in the atomic-rich phase causing a shift in the transition pressure.

The dc electrical conductivity, as computed by the Kubo-Greenwood relation within DFT, undergoes a discontinuous jump across the transition, showing that it is an insulator-metal transition. Using the computed dc conductivity as an order parameter, a critical point was estimated at $T_c = 2000$ K. The transition corresponds to a sharp change from semiconducting to metallic behavior caused by the sudden collapse of the molecular state. Even though strong short-range correlations persist after the transition is crossed, the resulting atomic liquid is metallic.

In Fig. 14 we show the LLPT from BOMD and CEIMC together with two different Kechin fits to the melting line data from BOMD for phase I (see Sec. IV.A.4). At low temperatures, the predicted LLT is expected to meet the melting line at 700 K and 220 GPa (using the BOMD estimates) and should result in a liquid-liquid-solid multiphase coexistence point. This point could be either a triple point if the two liquid phases coexist with a single solid phase or a quadruple point if the metal-insulator transition extends below freezing. Unfortunately, the use of DFT to extend the melting curve to higher pressures has difficulties in the neighborhood of the insulator-metal transition. Moreover beyond 200 GPa the stable crystal phase at melting is expected to be phase IV, rather than phase I; a study of the melting line for phase IV has not been done. Also note that CEIMC simulations along the isotherm at $T = 600$ K in the pressure interval $220 \leq P \leq 330$ GPa did not show any tendency to freeze, but finite-size effects biased the result. Further evidence in favor of a lower melting temperature at $P \simeq 300$ GPa was given by an alternative QMC-based *ab initio* method (Attaccalite and Sorella, 2008) which observed a disordered state at $\approx 400$ K, shown in Fig. 14 as a star.

An independent determination (Lorenzen, Holst, and Redmer, 2010) of the LLPT line by FPMD based on DFT with finite-temperature electrons, shown in Fig. 14, gives general agreement, although the exact location of the LLPT line and critical point varies. The existence of the transition (continuous or first order) is sensitive to size effects since small systems at the $\Gamma$ point do not exhibit a discontinuous behavior. Morales *et al.* (2010b) employed ground-state DFT-GGA with 432 atoms at the $\Gamma$ point. Lorenzen, Holst, and Redmer (2010) considered finite-temperature DFT-GGA and systems of 512 atoms computed at the Baldereschi point in the Brillouin zone. These system sizes are comparable to the one used by Scandolo (2003) and Bonev *et al.* (2004) with CPMD, and considerably larger than the one used by Vorberger, Tamblyn, Militzer, and Bonev (2007) and Holst, Redmer, and Desjarlais (2008) with BOMD. Note that in CEIMC, a system of 54 atoms is used but with twist averaged boundary conditions, the many-body analog of the Brillouin zone integration.

Bonev *et al.* (2004) ascribed the reentrant nature of the melting of the insulating molecular phase I reported in Fig. 14 to an increased softening of the repulsive intermolecular interactions with pressure, more pronounced in the liquid than in the solid phase due to the presence of the disorder. The nature of the insulating molecular liquid near the melting line was further investigated by Tamblyn and Bonev (2010a, 2010b). It was found that the liquid develops a short-range orientational order for pressures beyond the maximum of the melting line, and, in general, in the region between the melting and the LLPT lines. The orientational order is preserved, although changing its nature, when molecules dissociate. Using a criterium of survival time, the region of dissociation (from 67% to 33% molecular fraction), reported in Fig. 14 as a shaded area, has been traced up to $T = 4000$ K, close to the primary Hugoniot. Since pressure dissociation and metallization are seen to occur at the same time, the shaded region also indicates metallization. This simulation is in agreement with some estimates of metallization obtained by laser shocking a precompressed sample (Loubeyre *et al.*, 2004) as shown in Fig. 14.

### 3. Optical and transport properties

Along with EOS studies, first-principles simulation methods have been used extensively to study the optical and transport properties of hydrogen at high pressure, particularly in the liquid state (Pfaffenzeller, Hohl, and Ballone, 1995; Collins *et al.*, 1998; Collins, Bickham *et al.*, 2001; Holst, Redmer, and Desjarlais, 2008; Lin *et al.*, 2009; Holst, French, and Redmer, 2011; Lambert *et al.*, 2011). Optical properties are most often calculated using the Kubo-Greenwood formula within linear-response theory (Kubo, 1957; Greenwood, 1958) and DFT. Diffusion, viscosity, and other transport properties can be calculated from the dynamical correlation functions of the ionic trajectories. The thermal conductivity in the liquid atomic regime is typically calculated with the Wiedemann-Franz law (Franz and Wiedemann, 1853). A detailed description of the formulation is given in Holst, French, and Redmer (2011) along with its application to dense hydrogen, in particular, the electrical and thermal conductivity, thermopower, and Lorentz number as a function of density for temperatures between 10 000 and 50 000 K. Figure 15 shows the electrical conductivity, for various densities, as a function of temperature. These calculations were extended (Lambert *et al.*, 2011) using orbital-free MD as well as DFT to densities up to 160 $g/cm^3$ and temperatures up to 800 eV ($\approx 10\,000\,000$ K), well within the plasma phase. They compare their results with plasma models and discuss the implications of their results for the simulation of capsule implosions for ICF experiments.

As discussed semilocal functionals in DFT underestimate the band gap, and as a consequence overestimate the conductivity, particularly near the metal-insulator transition, i.e., close to the predicted liquid-liquid phase transition or to the continuous dissociation region at higher temperatures. See Kowalski *et al.* (2007) for a discussion of this error in dense helium. Calculations of the conductivity near dissociation have been performed (Lin *et al.*, 2009) with QMC methods, using CEIMC simulations to sample ionic configurations at finite temperature, combined with correlation function quantum Monte Carlo calculations (Ceperley and Bernu, 1988; Bernu, Ceperley, and Lester, 1990) to calculate the low energy many-body excitation spectrum of the liquid.

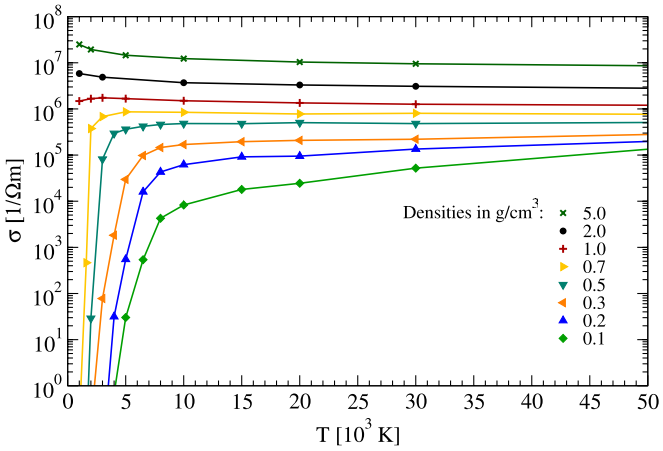


FIG. 15 (color online). Electrical conductivity of hydrogen as a function of temperature and density. From Holst, French, and Redmer, 2011.

Combining the excitation energies with the Green-Kubo formula, they calculated the electrical conductivity of hydrogen based entirely on QMC; these calculations do not suffer from self-interaction errors but suffer from other limitations, notably the numerical difficulty in obtaining accurate properties of excited states because of the QMC sign problem, and large finite cell size effects. However, good agreement with the limited data from shock experiments measurements was obtained (Weir, Mitchell, and Nellis, 1996).

### C. Quantum phases of high-pressure hydrogen

Because of the light proton mass, dense hydrogen may exhibit coherent quantum protonic phases at low temperatures. Two interesting possibilities that have been theoretically predicted are superconductivity and a low- or zero-temperature quantum fluid.

#### 1. Superconductivity

Ashcroft (1968) predicted that high-pressure hydrogen would be a high-temperature superconductor. Within the framework of the Bardeen-Cooper-Schrieffer (BCS) theory (Bardeen, Cooper, and Schrieffer, 1957), three key arguments support this prediction: (i) the light proton mass causes the vibrational energy scale of the phonons to be remarkably high (e.g., $\langle\omega\rangle/k_B \approx 2100$ K near 500 GPa), where $\langle\omega\rangle$ is the average phonon frequency, and thus is the prefactor in the expression for the critical temperature $T_c$ (see below); (ii) since the electron-ion interaction is simply the bare Coulomb attraction, electron-phonon coupling should be strong; and (iii) at high pressures, the electronic density of states at the Fermi surface should be large and the Coulomb repulsion between electrons should be relatively low, typical of high-density systems.

These essential ideas are highlighted in McMillan's estimate for $T_c$ (McMillan, 1968), which including the correction by Dynes (1972) can be written as

$$k_B T_c = \frac{\langle\omega\rangle}{1.2}\exp\left[-\frac{1.04(1+\lambda)}{\lambda-\mu^*(1+0.62\lambda)}\right], \tag{48}$$

where $\lambda$ is the electron-phonon-induced interaction and $\mu^*$ is the renormalized Coulomb repulsion. It is easy to see that if $\langle\omega\rangle$ and $\lambda$ are both high, while $\mu^*$ is low, then $T_c$ will be high as well.

Within standard *ab initio* methods, such as DFT, one can calculate both $\langle\omega\rangle$ and $\lambda$ (Savrasov and Savrasov, 1996), and further $\mu^*$ can be safely approximated as 0.1 in the atomic phase of high-pressure hydrogen (Richardson and Ashcroft, 1997). Note that this latter approximation does not work within the molecular phase, as will be discussed below. Note also that important corrections to Eq. (48) should be included (Carbotte, 1990) for strong-coupling superconductors using the Allen-Dynes equation (Allen and Dynes, 1975); see also a recent reparametrization for hydrogen (Szczesniak and Jarosik, 2009).

Ever since the original prediction (Ashcroft, 1968) of high-$T_c$ superconductivity, there have been several such efforts to predict $T_c$. However, since $T_c$ is sensitive to the presumed crystal structure (Whitmore, Carbotte, and Shukla, 1979), these have varied widely. We limit the discussion to some of the most promising structures for the molecular and atomic phases, as discussed in Secs. IV.A.1 and IV.A.6, the $Cmca$, $I4_1/amd$, and $R$-$3m$ structures; for a discussion of the older and other predictions, see McMahon and Ceperley (2011b).

Recently, McMahon and Ceperley (2011b, 2012) applied these techniques to investigate superconductivity in the atomic $I4_1/amd$ and $R$-$3m$ structures from 500 GPa to 3.5 TPa. Calculated values of $T_c$ from this work are shown in Fig. 16. As can be seen, the $T_c$ values are indeed remarkably high. Near the molecular-to-atomic transition ($\sim$ 500 GPa), $T_c \sim 311$ K. With increasing pressure, $\lambda$ increases, and together with the increase in phonon frequencies causes $T_c$ to increase to $\sim$360 K near 0.8–1 TPa. After the first (predicted) atomic-atomic structural phase transformation (i.e., $I4_1/amd \rightarrow R$-$3m$), a large jump in $\lambda$ occurs due to the high phonon density of states at low frequencies in the ensuing structure, which causes $T_c$ to increase beyond 400 K.

In the (metallic) molecular phase, the situation becomes especially interesting (but also more complex), as described

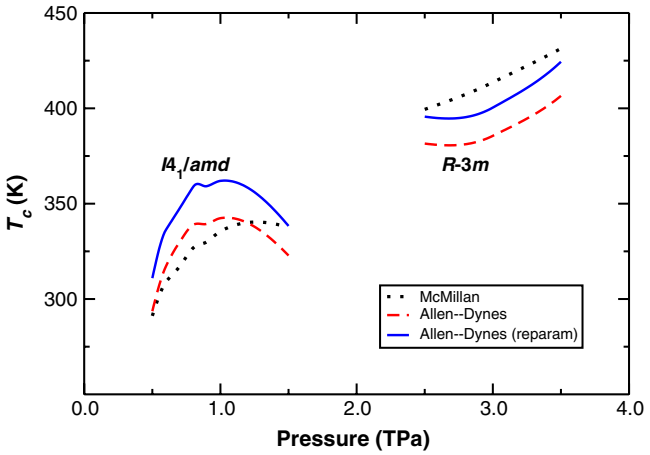


FIG. 16 (color online). Values of $T_c$ for atomic metallic hydrogen calculated using various formulas, as discussed by McMahon and Ceperley (2011b, 2012). Adapted from McMahon and Ceperley, 2012.

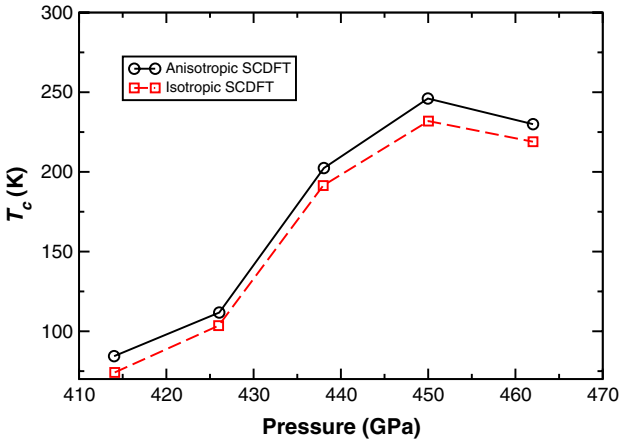


FIG. 17 (color online). Values of $T_c$ for metallic molecular hydrogen calculated using SCDFT. See Cudazzo *et al.* (2010b) for a discussion of the differences between anisotropic and isotropic SCDFT. Adapted from Cudazzo *et al.*, 2010b.

by Richardson and Ashcroft (1997). The assumption that $\mu^*$ adopts a fixed value becomes invalid. Lüders *et al.* (2005) developed a multicomponent DFT method for superconductivity, termed SCDFT, which involves solving a set of Kohn-Sham equations for wave functions that represent particle and hole amplitudes $\varphi_i(\mathbf{r})$ as well as protonic amplitudes $\Phi_l(\mathbf{R})$:

$$\left[-\frac{\nabla^2}{2}+v_s^e[n,\chi,\Gamma](\mathbf{r})-\mu\right]\varphi_i(\mathbf{r})=\epsilon_i\varphi_i(\mathbf{r}), \tag{49}$$

$$\left[-\sum_\alpha\frac{\nabla_\alpha^2}{2M}+v_s^n(\mathbf{R})\right]\Phi_l(\mathbf{R})=\varepsilon_l\Phi_l(\mathbf{R}), \tag{50}$$

where $n$ is the electronic density, $\chi$ is an "anomalous" density representing the order parameter that characterizes a singlet superconducting state, $\Gamma$ is the diagonal part of the $N$-particle density matrix, $v_s^e(\mathbf{r})$ and $v_s^n(\mathbf{R})$ are Kohn-Sham potentials for the electrons and nuclei, respectively, and $\mu$ is the chemical potential. For a comparison of those equations to the standard formulation of DFT, see Sec. II.E.1.

Following the development of SCDFT, Cudazzo *et al.* (2008, 2010a, 2010b) modeled the high-pressure metallic molecular phase of hydrogen, *Cmca*. Calculated $T_c$ values are shown in Fig. 17, where it can be seen that, much like in the atomic phase, they are remarkably high, increasing up to 242 K near 450 GPa.

As can be seen, and consistent with original predictions (Ashcroft, 1968), $T_c$ values in hydrogen are remarkably high, in both the molecular and atomic phases. It is intriguing to note that the high values of $T_c$ combined with the low values of $T_m$ (see Sec. IV.A.4) suggest that solid atomic hydrogen may exist entirely in a superconducting state. There have also been predictions (Jaffe and Ashcroft, 1981) that liquid metallic hydrogen (i.e., above the melting temperature) will itself be superconducting. These observations set the stage for the discussion that is to follow in the next section, where it will be demonstrated that superconductivity and quantum fluidity in hydrogen are rich areas of exploration awaiting experimental confirmations.

### 2. A quantum fluid

Brovman, Kagan, and Kholas (1972b) noted that there are many atomic hydrogen structures with similar energies, such as the anisotropic layered ones. This suggests that the transition from the molecular state to the atomic one might also involve a transition from the solid phase to a low-temperature liquid. There are two effects that favor such a state. First, the bare $p$-$p$ interaction is screened by the electrons, causing the effective interaction near $r_s = 1.3$ to be weak and short ranged.[7] Friedel oscillations in the effective interaction can then frustrate many crystal structures. Second, the large proton ZPM favors a disordered liquid state versus an ordered solid. Hohl *et al.* (1993) demonstrated that the kinetic energy of the protons in various crystal structures at 0 K (and at the lowest pressures that atomic hydrogen may exist) can be as large as 7000 K/atom. An analogous physical system is $^3$He, which indeed has a liquid ground state for pressures less than 0.003 44 GPa.

In passing, we point out that at sufficiently high pressures, it is almost certain that hydrogen will be in a liquid state at 0 K. Under such conditions, one can ignore the electrons, since they become uncorrelated with the protons. Hence, the proton system becomes the quantum one-component plasma (OCP) (i.e., jellium). Extensive QMC calculations (Ceperley and Alder, 1980) (using an electron mass or $r_s = 0.058$ times the proton mass) of the quantum OCP established that the Wigner crystal melts to a Fermi liquid near $r_s = 106$. This high-pressure transition is shown in Fig. 2, corresponding to the extremely high pressure of $10^{13}$ GPa. While these results are interesting, it is unlikely that there are conditions anywhere where hydrogen is this dense and this cold.

The complete absence of an atomic solid phase (at any pressure) was suggested by Kechin (2004a, 2004b) again due to the large atomic ZPM. However, many approximations were made to arise at this prediction. Moreover, the results do not appear consistent with *ab initio* calculations.

Such simulations of the melting line of atomic hydrogen (Xu, Hansen, and Chandler, 1994; Kohanoff and Hansen, 1995, 1996) indicate that at somewhat lower pressures (e.g., the TPa range), the bcc lattice may melt at surprisingly low temperatures and become even less stable with decreasing pressure. Even though these simulations neglected ZPM, recent calculations by Liberatore, Pierleoni, and Ceperley (2011) found that ZPM is similar in both the solid and liquid phases at these conditions (because of similarities in local structures), and thus, its overall impact is not large.

Now considering the molecular phase, in Sec. IV.A.4 we discussed that the melting temperature reaches a maximum at a pressure of ~100 GPa, but then decreases. Extrapolations of the melting curve from *ab initio* calculations (Bonev *et al.*, 2004), combined with the atomic melting results discussed above, suggest the possibility of an intermediate range where a low- or zero-temperature liquid phase could exist (Ashcroft, 2000, 2003).

[7]At a certain pressure, electrons become bound to protons, and the total interaction of the system becomes essentially that between neutral atoms.

Despite these indications, there have been simulations that in fact disagree with such a scenario. For example, early QMC calculations by Mon, Chester, and Ashcroft (1980, 1983) using an effective screened Coulomb interaction found that the solid has lower energy than the liquid for densities appropriate to atomic hydrogen [$0.8 \leq r_s \leq 1.36$, a range partially based on the VMC calculations by Ceperley, Chester, and Kalos (1978) for the Yukawa phase diagram]. As another example, a DMC calculation by Ceperley (1988), again using the screened Coulomb interaction, found solid phases to be stable for $r_s \leq 1.6$. Even if the crystal structures used in these calculations were incorrect, the results seem to exclude the existence of a ground-state liquid. These simulations did, however, invoke serious approximations through the use of effective (proton) interactions. Chakravarty and Ashcroft (1978) showed that the assumption of a pair proton interaction in this range of densities is likely to cause much greater errors than the difference in energies between the two phases. Nonetheless, DMC simulations involving electrons and protons (Ceperley, 1988), and with the proper masses, found stable solid fcc and bcc phases for densities above $r_s = 1.6$. These calculations also supported the perturbation estimates (Chakravarty and Ashcroft, 1978) that solid-liquid energy differences with the bare Coulomb interaction are much different (5 times larger) than when it is screened. On the other hand, use of the more recent crystal structures (see Sec. IV.A.6) would even further stabilize the solid. However, the fixed-node approximation and time-scale separation issues in QMC both favor a solid phase. It is clear that there is some uncertainty in these predictions.

More recent QMC-based MD simulations (Attaccalite and Sorella, 2008) of the *e-p* system using forces computed from VMC with a resonating valence bond trial wave function (albeit, without ZPM) again support the existence of a low-temperature liquid. These simulations indicated that a molecular liquid should be more stable than a simple hexagonal or bcc atomic solid, at least at ~400 K and 300 GPa. To make this claim with certainty though, one needs to explore more stable crystal structures, different trial wave functions, include proton ZPM, and perform a better treatment of finite-size effects. The predictions of a low- or zero-temperature quantum fluid combined with the prediction of high-$T_c$ superconductivity (see Sec. IV.C.1), led Jaffe and Ashcroft (1981) to predict that hydrogen could become a new state of matter altogether, a superconducting superfluid. Jaffe and Ashcroft (1983) analyzed the properties of such a state, demonstrating that it would likely pass from a type-II to a type-I superconductor with decreasing temperature. Furthermore, at low temperatures, Moulopoulos and Ashcroft (1999) and Ashcroft (2000) suggested further that not only should electrons form Cooper pairs, but protons could also. A topological analysis of such a two-component system by Babaev, Sudbø, and Ashcroft (2004) revealed that, because of these features, the presence of a magnetic field could cause hydrogen to exhibit several novel ordered states, ranging from metallic to superconducting superfluids.

The predictions of a low- or zero-temperature quantum fluid and its properties represent intriguing possibilities. As indicated above, however, its existence is still an open question. Further experiments and calculations are thus needed to settle this issue.

## V. HELIUM AND HELIUM-HYDROGEN MIXTURES

Thermodynamic properties of He-H mixtures have a special significance in the modeling of many giant planets, for example, Jupiter and Saturn. These planets, generally believed to have been formed approximately at the same time as the Sun, are made primarily of hydrogen and helium, with a mass fraction of the latter at the surface of $Y = 0.234 \pm 0.005$ for Jupiter (von Zahn, Hunten, and Lehmacher, 1998) and $Y = 0.18 - 0.25$ for Saturn (Conrath and Gautier, 2000). Note that the estimated protosolar helium mass fraction is $Y \sim 0.27$ (Bahcall, Pinsonneault, and Wasserburg, 1995). Possible interior models for these planets, which define their composition as a function of depth, are constrained by experimental observations, such as the total mass, radius, rotational rate, gravitational moments, and surface temperatures, among others.

Most models built so far are based on a three-layer structure, with a solid core made of heavy elements and ices, an intermediate layer made up mostly of metallic hydrogen and helium, and an upper layer rich in molecular hydrogen, helium, and small traces of other molecules such as methane, water, and ammonia; see Fig. 18. Such models typically assume solid body rotation, hydrostatic equilibrium, a fully convective and isentropic interior, and a homogeneous and constant mixture of helium in the metallic and molecular layers. These assumptions lead to a set of hydrostatic equations for the pressure, density, and entropy as a function of a planet's radius (Stevenson, 1982). In order to close this set of equations, the EOS of the mixture is needed, specifically $P = P(\rho, T, x_i)$, where the addition of $x_i$ indicates the molar fractions of the mixture. Most current models of Jupiter and Saturn are based on the SCVH EOS (Guillot, Chabrier *et al.*, 1994; Guillot, Gautier *et al.*, 1994; Guillot, Gautier, and Hubbard, 1997; Guillot, 1999). Recently, however, models for Jupiter used EOS derived from first-principles simulations (Militzer *et al.*, 2008; Nettelmann *et al.*, 2008). Currently,

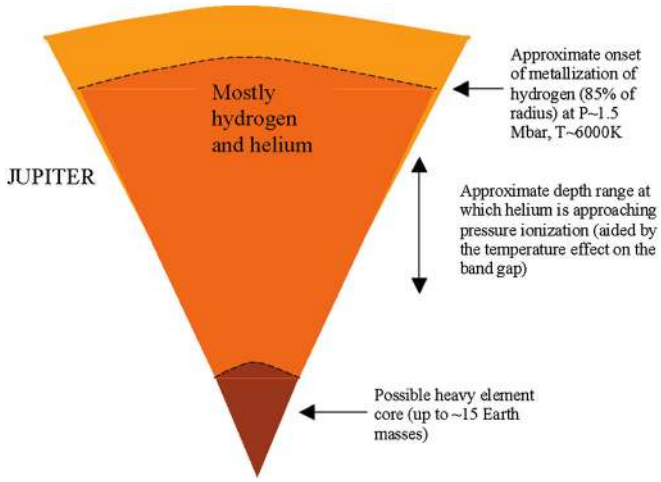


FIG. 18 (color online). Standard three-layer model of Jupiter. From Stevenson, 2008.

the largest uncertainty in the models comes from the limited knowledge of the equation of state of He-H mixtures at high pressures, the uncertainty associated with possible transitions in the dense liquid (e.g., the LLT), and the immiscibility of helium in metallic hydrogen (Fortney, 2004; Guillot, 2005), the latter which will be discussed below.

In this section, we review the current understanding of helium and He-H mixtures based on first-principle calculations. We first review work on pure helium, with an emphasis on the phase diagram, the EOS, and optical properties at high pressure. We then discuss recent work on mixtures, with an emphasis on the calculation of the EOS as well as the solubility of helium in metallic hydrogen.

### A. Helium

At ambient conditions helium is an inert gas with a large band gap. Because of its low mass and weak interatomic interactions, it has fascinating properties at low temperatures and displays a wide array of exotic phenomena such as superfluidity. In this review, we focus only on the high-pressure properties of the isotope $^4$He.

#### 1. Equilibrium properties: Equation of state and structure

At pressures above 25 bar (2.5 MPa) at zero temperature, $^4$He crystallizes into the hcp phase. Thermodynamic measurements show the existence of an hcp-fcc phase transition at $P \sim 1.1$ GPa, with a hcp-fcc-liquid triple point located approximately at 0.1 GPa and 15 K (Dugdale and Simon, 1953). Early melting experiments using DAC techniques by Loubeyre *et al.* (1982) showed the existence of a cusp in the melting line at 11.65 GPa and 299 K, suggesting the existence of a new phase at higher pressures. Single-crystal x-ray diffraction measurements at 300 K with DACs and synchrotron radiation showed that solid helium forms an hcp phase in the pressure range 15.6–23.3 GPa (Mao *et al.*, 1988); the stability of the hcp phase up to 58 GPa was subsequently confirmed (Loubeyre *et al.*, 1993). The melting line has been measured experimentally to pressures of 24 GPa by Vos, van Hinsberg, and Schouten (1990), and up to 41 GPa by Datchi, Loubeyre, and LeToullec (2000) with a resistively heated DAC. Recent measurements using laser-heated DACs extended the melting line to pressures up to 80 GPa (Santamaria-Perez *et al.*, 2010). There is good agreement in the measured melting lines up to 20 GPa, but the measurements of Santamaria-Perez *et al.* (2010) are in disagreement with an extrapolation of the measurements of Datchi, Loubeyre, and LeToullec (2000) to higher pressures. On the other hand, the extrapolation of the melting line of Vos, van Hinsberg, and Schouten (1990) is in reasonable agreement with that of Santamaria-Perez *et al.* (2010). This disagreement has led to some controversy regarding the high-pressure phase diagram of helium. Classical MD simulations using empirical potentials suggested the existence of a fcc-bcc phase transition above 12 GPa (Koi *et al.*, 2007), providing an alternative explanation to the measured cusp in the melting line. But since these results strongly depend on the empirical interatomic potential used to describe He, they do not resolve the discrepancy.

Various first-principles studies of the metallization transition in helium have been reported. The most recent calculations by Khairallah and Militzer (2008) predict a zero-temperature band-gap closure at 25.7 TPa, using both QMC and *GW* methods. As expected, DFT calculations using semilocal functionals predict a transition pressure that is 40% smaller. On the other hand, perfect agreement is found between *GW* and QMC predictions. First-principles calculations of the elastic properties of solid helium were reported by Nabi *et al.* (2005), showing good agreement with experimental results (Zha, Mao, and Hemley, 2004).

Liquid helium at high pressures and temperatures has been the subject of numerous studies. The principal Hugoniot was measured using a two-stage light-gas gun, liquid helium at 4.3 K and 1 bar was shocked to 16 GPa and 12 000 K and double shocked to pressures of 56 GPa and 21 000 K (Nellis *et al.*, 1984). The Hugoniot was recently extended to pressures over 100 GPa by combining DACs and laser-driven shock wave techniques (Eggert *et al.*, 2008). Several precompressed states were shocked, enabling the exploration of an enlarged region of phase space.

Several chemical models for helium have been developed (Saumon, Chabrier, and Horn, 1995; Juranek, Schwarz, and Redmer, 2003; Winisdoerfer and Chabrier, 2005; Chen *et al.*, 2007), most of them built from perturbative expansions of the free energy using theoretical helium interatomic potentials, such as the Aziz potential (Aziz and Slaman, 1991) or the Ceperley-Partridge potential (Ceperley and Partridge, 1986). These models, e.g., SCVH, have been extensively used in planetary models of Jovian planets. At low pressures, good agreement is found between experiments and these models. As pressure increases, electronic and thermal effects become important and perturbative treatments become less accurate. Available experimental input is very limited.

There are several first-principles studies of the thermodynamic properties of liquid helium (Militzer, 2005, 2006; 2009; Kietzmann *et al.*, 2007; Kowalski *et al.*, 2007; Vorberger *et al.*, 2007b; Lorenzen, Holst, and Redmer, 2009; Morales *et al.*, 2009), most of them using DFT-based MD with a semilocal functional, e.g., the PBE functional. Figure 19 shows a comparison of several Hugoniots of helium as measured and predicted by chemical models or first-principles simulations (Eggert *et al.*, 2008).

A recent study compared the EOS of helium between DFT-based BOMD and RPIMC methods (Militzer, 2009); RPIMC was used for temperatures above 60 000 K and DFT-MD for temperatures between 500 and 125 000 K, in the density range 0.38–5.35 g/cm$^3$. This work is particularly interesting because it establishes the importance of the electronic temperature in DFT-MD calculations and, in addition, compares predictions of both simulation methods for temperatures around 100 000 K, where both methods should be applicable and accurate. Good agreement between the methods was found for temperatures above 80 000 K, as long as the thermal occupation of the electrons is taken into account in DFT. These results suggest that the Born-Oppenheimer approximation is good for calculating the equilibrium properties at temperatures below 100 000 K. Its influence on dynamical properties at such high temperatures is still not well established.

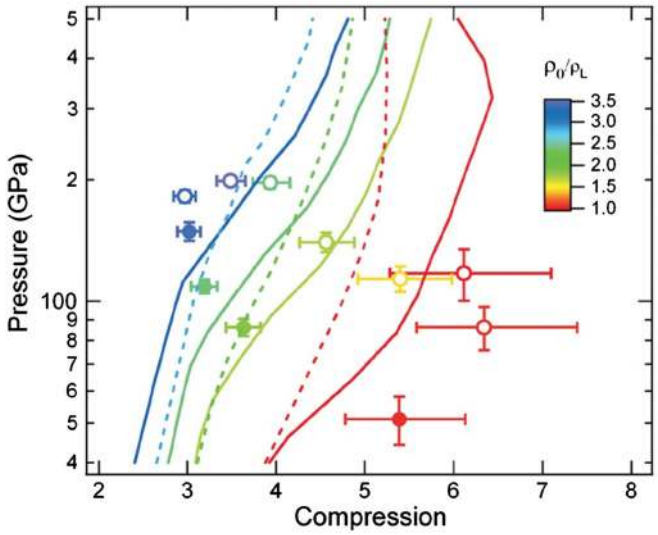


FIG. 19 (color online). Measurements of the principle helium Hugoniots for various initial densities. Symbols indicate the measured data, with open and closed symbols indicating whether the shocked state is reflecting or opaque, respectively. The solid line is the SCVH model (Saumon, Chabrier, and Horn, 1995) and the dashed line, *ab initio* calculations (Militzer, 2006). The initial (precompressed) He density, measured relative to the zero-pressure density of the cryogenic liquid and indicated by $\frac{\rho_0}{\rho_L}$, increases from right to left. From Eggert *et al.*, 2008.

At intermediate temperatures and pressures between 160 and 1600 GPa, the EOS has been studied in detail using the CEIMC method (Morales, 2009). Figure 20 shows the pressure of helium as a function of density as given by several chemical models: DFT-based BOMD and QMC-based CEIMC simulations. Good agreement exists between DFT and QMC-based simulation methods with these conditions. The chemical model, SCVH (Saumon, Chabrier, and Horn, 1995), agrees reasonably well with first-principles simulation results; however, the WC model (Winisdoerfer and Chabrier, 2005) shows marked differences in magnitude and overall density dependence. This comparison is further evidence that DFT and QMC simulation methods agree well and thus make robust predictions of the equilibrium thermodynamic properties of helium at high pressure.

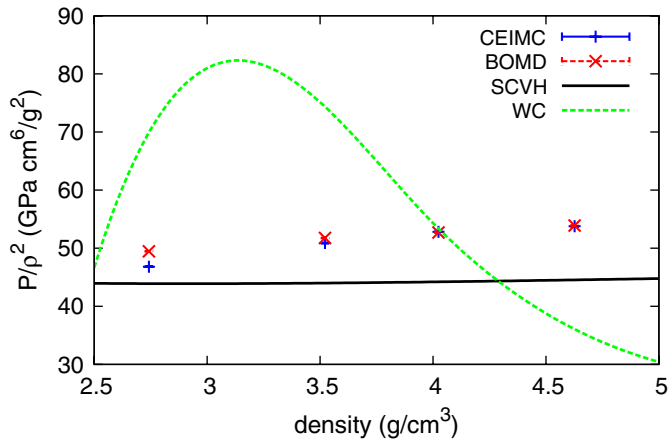


FIG. 20 (color online). Comparison of the pressure of liquid helium as a function of density, along an isotherm at $T = 6000$ K, between CEIMC (Morales, 2009), DFT-based BOMD (Morales *et al.*, 2009), and the SCVH (Saumon, Chabrier, and Horn, 1995) and WC (Winisdoerfer and Chabrier, 2005) chemical models.

## 2. Dynamic properties: Optical and transport properties

Advances over the last decade in the field of dynamic compression, particularly in their diagnostic tools, enabled the direct measurement of optical properties of helium at pressures above 100 GPa and temperatures up to 60 000 K (Ternovoi *et al.*, 2002; Celliers *et al.*, 2010). Figure 21 shows the measured reflectivity of helium as a function of temperature and density along several Hugoniots with different initial densities. The experiments suggest that helium undergoes an insulator-to-metal transition as either density or temperature is increased. The exact nature of the transition is still not clear, especially at low temperatures in the liquid.

There have been various first-principles studies of the optical properties of liquid helium at high pressure (Kietzmann *et al.*, 2007; Kowalski *et al.*, 2007; Stixrude and Jeanloz, 2008; Hamel, Morales, and Schwegler, 2011; Lorenzen, Holst, and Redmer, 2011). Using linear-response theory within the Kubo-Greenwood formulation and DFT, Kowalski *et al.* (2007) calculated the band gap, conductivity, reflectivity, index of refraction, and absorption coefficient as a function of density and temperature. They studied the influence of the DFT exchange-correlation potential on the band gap of the liquid, clearly demonstrating the strong reduction in the gap due to self-interaction errors in semilocal functionals such as PBE. Using the *GW* method and hybrid-DFT calculations, they were able to devise a simple correction to the optical properties obtained from semilocal functionals, improving the agreement with experiment. They also showed that the self-interaction errors decrease with increasing temperature. Stixrude and Jeanloz (2008) also calculated the band gap and the conductivity of liquid helium, extending

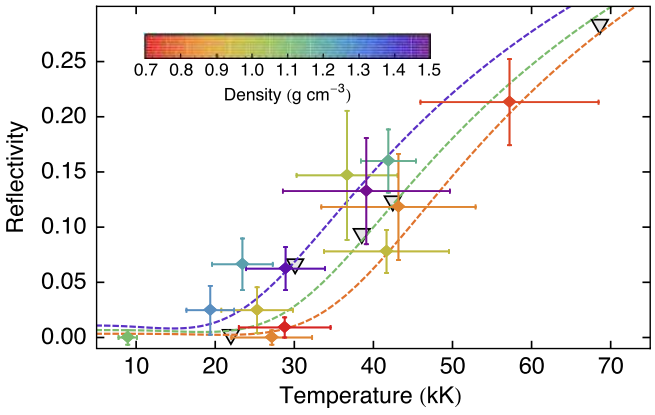


FIG. 21 (color online). Reflectivity measurements of helium using laser-driven dynamic compression (Celliers *et al.*, 2010). Solid diamonds show the observed reflectivity as a function of temperature and final density indicated by the color scale. Curves show the reflectivity obtained from a fit to the data using the semiconductor Drude model for three final state densities, from bottom to top: 0.8, 1.1, and 1.4 g/cm$^3$. Triangles are calculated reflectivities by Kowalski *et al.* (2007) near 1 g/cm$^3$ with $a + 3$ eV gap correction. From Celliers *et al.*, 2010.

to temperatures up to 50 000 K and densities up to 6 g/cm$^3$. Their work showed that the gap closure occurs at much lower pressures in the liquid compared to the solid and depends strongly on temperature.

The first detailed study of the optical properties of hydrogen-helium mixtures using first-principles simulations came with the recent work of Hamel, Morales, and Schwegler (2011), where the conductivity and reflectivity of the mixture were calculated as a function of pressure, temperature, and composition at pressures above 300 GPa and temperatures above 4000 K. This corresponds to the region of pressure and temperature where helium becomes immiscible in metallic hydrogen (Morales *et al.*, 2009). They use the frequency dependence of the reflectivity for both a mixed and a phase separated sample to predict a possible signature of phase separation in dynamic-compression experiments. The conductivity and miscibility of hydrogen-helium mixtures across the dissociation regime has also been studied by Lorenzen, Holst, and Redmer (2011) using first-principles methods.

### B. Phase separation of H and He

The EOS of hydrogen-helium mixtures is a key ingredient for the interior models of Jupiter, Saturn, and other hydrogen-rich planets. In fact, the solubility of helium in hydrogen at high pressure plays a crucial role in the correct description of these planets. The giant planets typically radiate more energy than they take in from the Sun. The current luminosity of Jupiter is well described with an evolution model for a convective homogeneous planet radiating energy left over from its formation $4.55 \times 10^9$ years ago. But a similar model for Saturn seriously underestimates its current luminosity (Hubbard *et al.*, 1999). Although solar heating prolongs the cooling time of Saturn, its influence is not enough to reconcile its age with the expected time of formation. Hence, an additional energy source playing a more important role in Saturn than in Jupiter needs to be found.

Helium condensation was proposed as a possible explanation for the excess luminosity in Saturn and the helium depletion in the atmosphere of both giant planets (Smoluchowski, 1967; Stevenson, 1975, 1979; Stevenson and Salpeter, 1977a, 1977b). Suppose that there is a region in the planet's interior where helium is insoluble; helium droplets will form and thereby act as a source of energy, both through the release of latent heat and by descending deeper into the center of the planet. Figure 22 shows a schematic representation of three different scenarios for the interior structure of Saturn based on possible mixing properties of helium in metallic hydrogen. Because Jupiter and Saturn have different total masses, the thermodynamic conditions in the planetary interiors could be such that this condensation process is more prevalent in Saturn than in Jupiter. Although this mechanism could explain most of the experimental observations in Saturn, an accurate understanding of the miscibility properties of helium on metallic hydrogen was only recently obtained using first-principles simulations.

This problem of helium solubility in metallic hydrogen has received great attention over the past 30 years. Before the development of first-principles simulations, calculations used perturbative treatments (Hansen, Torrie, and Vieillefosse, 1977; Pollock and Alder, 1977; Stevenson and Salpeter, 1977a, 1977b; Straus, Ashcroft, and Beck, 1977; Stevenson, 1979; Hubbard and DeWitt, 1985) of the mixture free energy with assumed interactions between chemical species (e.g., He, $He^+$, H, $H^+$, $H_2$, etc.). Almost all calculations assumed a fully pressure-ionized mixture in order to facilitate the perturbative treatment. For the temperature and pressures relevant to planetary modeling, the assumption of complete ionization is now believed to be inaccurate, limiting the reliability of those calculations. Although the details of each calculation varied in terms of approach and complexity, most calculations found that the critical temperature for immiscibility decreased with increasing pressure and was generally too low to explain the observed discrepancy in the luminosity of Saturn (Fortney and Hubbard, 2004).

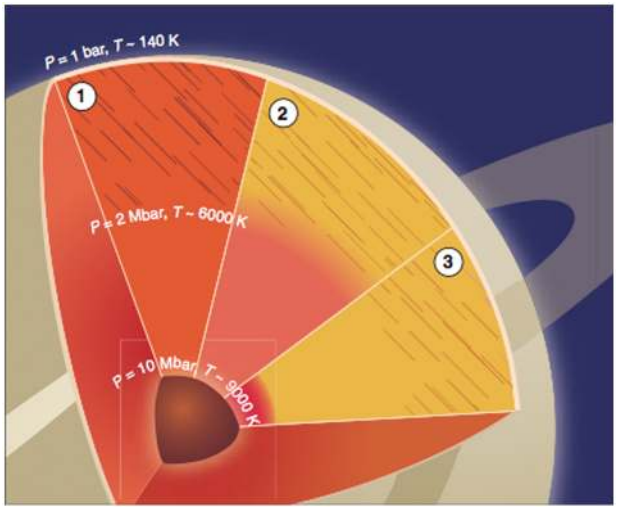


FIG. 22 (color online). Three views of the interior of Saturn. Indicated are the protosolar He/H ratio where color shows less He, and more He. The center is the ice/rock core. The hashed regions indicate molecular hydrogen, while the unhashed regions indicate atomic metallic hydrogen. (1) Saturn at an age of $1.5 \times 10^9$ years, before the onset of He phase separation. (2) The current Saturn according to a previously proposed H-He phase diagram (Stevenson, 1975). (3) The current Saturn according to a phase diagram derived from new evolutionary models (2). From Fortney, 2004.

The first application of first-principles methods (Klepeis *et al.*, 1991) used DFT calculations based on the LDA to calculate the enthalpy of mixing of alloys of hydrogen and helium at zero temperature as a function of composition. Using the ideal mixing approximation, they obtained a demixing temperature of 15 000 K for $x_{He} = 0.07$, suggesting that there should be phase separation in both Jupiter and Saturn. However, their work neglected both the relaxation of the ionic crystal after the introduction of helium and the disorder characteristic of a fluid. Using FPMD simulations with the Car-Parrinello technique Pfaffenzeller, Hohl, and Ballone (1995) estimated the free energies of a mixture by a reweighting technique from the pure hydrogen liquid. They found a negligible temperature effect on the mixing free energy up to temperatures of 3000 K, disregarded thermal effects in the enthalpy of mixing, using instead the ideal mixing entropy. They obtained immiscibility temperatures too low to allow for differentiation in either Jupiter or Saturn.

The first proper *ab initio* treatment of the problem came recently with the work of Morales *et al.* (2009). Using a combination of DFT-based BOMD calculations and thermodynamic integration, they calculated the Gibbs free energy of mixing as a function of pressure, temperature, and composition without resorting to the ideal mixing approximation. Independent DFT-based BOMD calculations, by Lorenzen, Holst, and Redmer (2009), of the Gibbs free energy with the ideal mixing approximation for the entropy were also done. The two calculations agree very well in the regime where ideal mixing is valid.

To determine when the H-He system is mixed, one needs the Gibbs free energy as a function of pressure, temperature, and composition. The free energy is important, not only to calculate the critical concentrations, but also to produce accurate equations of state for planetary modeling. In the case of H-He mixtures, the ideal mixing approximation significantly affects the resulting properties of planets and needs to be removed by direct calculation of the free energy.

Simulation methods such as Monte Carlo and molecular dynamics calculate ensemble averages of properties such as energy, pressure, density, etc. Free energies, or any property that directly involves the entropy, must be calculated by integrating along a thermodynamic pathway from a many-body system with known free energy (Frenkel and Smit, 2002). Until recently, this extra integration, in combination with the high computational cost of first-principles simulations, prevented the evaluation of the Gibbs free energy of H-He mixtures. Morales *et al.* (2009) used a coupling constant integration to determine the free-energy difference between a DFT description of the mixtures and that of a pair-potential model tuned to produce a reasonable description of the DFT model. The pair-potential simulation is many orders of magnitude faster than that of the first-principles model and its free energy can be calculated by integrating from the limit of zero density.[8]

Using energies and pressures from *ab initio* BOMD simulations on a grid of temperatures and densities, Morales *et al.* (2009) calculated free energies for pressures between 300 and 1800 GPa, and temperatures between 4000 and 10000 K. In Fig. 23, the Gibbs free energy of mixing is shown as a function of composition, as calculated by Lorenzen, Holst, and Redmer (2009) and Morales *et al.* (2009), at a pressure of 400 GPa. The strong temperature dependences of the immiscibility properties of the mixture are apparent from these results. A weak pressure dependence on the mixing free energies at low helium compositions is found. This leads to a weak dependence of critical mixing temperatures for compositions relevant to planetary interiors. Note how the Gibbs free energies reported by the different calculations agree well at low helium fractions, but disagree as the helium fraction increases.

As shown in Morales *et al.* (2009), the structure of hydrogen is strongly influenced by the helium concentration. The inert character of a helium atom makes it insensitive to changes in the local environment, however, a proton is very sensitive. While at low $x_{\mathrm{He}}$ hydrogen is in the monoatomic

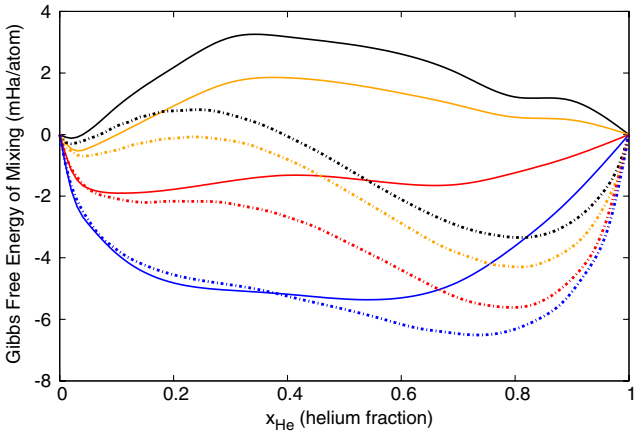


FIG. 23 (color online). The Gibbs free energy of mixing as a function of composition, at a pressure of 400 GPa, for several temperatures, from top to bottom: 5000 K, 6000 K, 8000 K, and 10 000 K. The solid lines represent full free-energy calculations from Morales *et al.* (2009). The dashed lines represent results using the ideal mixing approximation for the entropy from Lorenzen, Holst, and Redmer (2009).

fully ionized state, an effective proton-proton attraction reminiscent of the molecular bonding develops upon increasing $x_{\mathrm{He}}$, even at very high pressures and temperatures. Figure 24 shows the proton-proton radial distribution functions for mixtures with various helium concentrations, at 8000 K for the density $r_s = 1.05$. A molecularlike peak builds up smoothly as $x_{\mathrm{He}} \rightarrow 1$. The inert helium inhibits the delocalization of the hydrogenic electrons, enhancing the formation of weak molecular bonds with short lifetimes. A similar stabilization of molecular hydrogen by helium, but at much lower temperature and density, has been previously reported

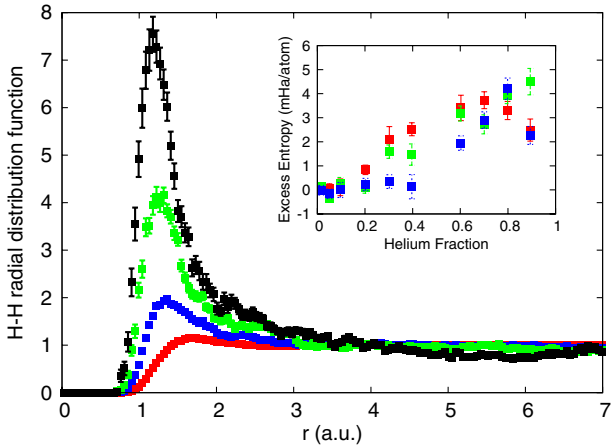


FIG. 24 (color online). The effect of increasing concentrations of helium on the proton-proton radial distribution function (Morales *et al.*, 2009) for various compositions at a temperature of 8000 K and an electronic density given by $r_s = 1.05$; helium fractions from top to bottom: $x_{\mathrm{He}} = 0.9$, $x_{\mathrm{He}} = 0.8$, $x_{\mathrm{He}} = 0.6$, and $x_{\mathrm{He}} = 0.0$. Inset: Excess entropic contribution of the Gibbs free energy of mixing, in mHa/atom, for several temperatures at a pressure of 800 GPa: $T = 6000$ K, $T = 8000$ K, and $T = 10\,000$ K.

[8]Care must be taken to ensure that first-order phase transitions are not crossed during the integration.

close to the dissociation regime in pure hydrogen by Vorberger, Tamblyn, Militzer,and Bonev (2007).

The change in the chemical properties of hydrogen produced by helium induces nonlinear effects in the mixing functions. Figure 24 shows the excess nonideal entropic contribution to the Helmholtz free energy, defined as $S_{\text{excess}}(x) = S(x) + [x\ln(x) + (1-x)\ln(1-x)]$, at a pressure of 800 GPa. It is zero up to a helium fraction of $x_{\text{He}} \approx 0.2$, and increases after this point. As long as the fraction of helium is not large enough to induce the pseudomolecular state in hydrogen, the ideal mixing approximation for the entropy is good. Once the pseudomolecular state emerges, nonlinear corrections to the mixing entropy appear and the full mixing free energy is needed to obtain an accurate description of the immiscibility process. The nonlinear mixing entropy is roughly 3 mHa/atom at high helium fraction, comparable to the mixing Gibbs free energy. Calculations ignoring the excess produce accurate results for $x_{\text{He}} < 0.2$, but nonphysical stable mixtures for $x_{\text{He}} < 0.5$; compare Fig. 23 with the inset in Fig. 24. The difference between results of Lorenzen, Holst, and Redmer (2009) and Morales *et al.* (2009) is well explained by the presence of a minimum in Lorenzen's mixing Gibbs free energies at $x_{\text{He}} \sim 0.8$ leading to demixing temperatures about 700 K higher. Otherwise the agreement between the calculations is excellent.

Figure 25 shows a comparison of demixing temperatures as a function of composition for several calculations described above. A prominent feature of the recent first-principles calculations is that pressure has only a moderate effect on the immiscibility process. For a fixed helium fraction, the demixing temperature changes by approximately 500 K in a pressure range of 800 GPa for the relevant concentrations of He (5%–10%). Immiscibility occurs at temperatures well below those required to produce ionization in helium (Stevenson, 2008); models with fully ionized He atoms are not appropriate for describing the pressure dependence of the demixing temperature. At pressures much higher than those discussed here, metallization of helium will play an important role and should produce significant changes to the pressure dependence of the immiscibility temperature.

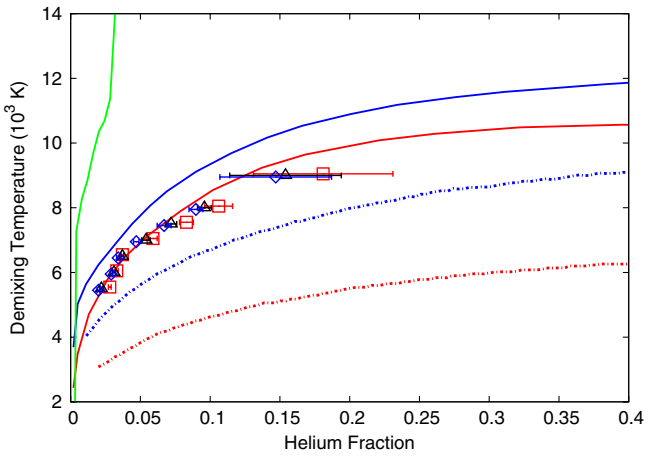


FIG. 25 (color online). Demixing temperatures as a function of the helium number fraction, for several pressures, from right to left: 400 (squares), 800 (triangles), and 1000 (diamonds) GPa. Symbols represent results from Morales *et al.* (2009), solid lines are results from Lorenzen, Holst, and Redmer (2009), dashed lines are results from Pfaffenzeller, Hohl, and Ballone (1995), and the almost vertical solid line at the extreme left is from Klepeis *et al.* (1991) at 1050 GPa.

Recent estimates of the demixing temperature have important implications for the study of the interior structure of hydrogen-rich planets, especially Saturn. First-principles results support the scenario that He becomes partially miscible in the intermediate layers of the planet, with the excess helium falling toward the core through gravitational differentiation. Whether the immiscible region is large enough to account for all the observed properties of Saturn is yet to be determined, but it is clear that planetary models should include phase separation. In general, the new DFT-based EOS could make a significant modification to interior models calculated with the SCVH EOS (Saumon, Chabrier, and Horn, 1995). While models of Jupiter based on first-principles EOS are beginning to appear (Militzer *et al.*, 2008; Nettelmann *et al.*, 2012), there is not yet a clear consensus on some of the details of the models. Nonetheless, the use of the new EOS is an important step forward which should help obtain more accurate models of planetary interiors.

## VI. CONCLUSIONS AND OUTLOOK

The last two decades have witnessed enormous progress in our understanding of high-pressure hydrogen, helium, and their mixtures, due in large part to the synergy between experiment and theory. We focused primarily on what was learned from numerical simulations, much of which occurred only recently, now that such methods and computer hardware have advanced to the point where important questions can be reliably answered.

Unfortunately, uncertainties in experimental findings are still rather large, and achievable pressures and temperatures are limited. Thus, experiments alone cannot yet provide enough definitive information. One outstanding constraint, for example, is that DAC experiments at low temperatures have not been able to reach pressures where hydrogen conclusively becomes an atomic metal. Even though the recent experiment by Eremets and Troyan (2011) in fact claims to have achieved this, this interpretation is both controversial (Jephcoat, 2011; Nellis, Ruoff, and Silvera, 2012) and inconsistent with the semimetallic behavior seen by Howie *et al.* (2012) and Zha, Liu, and Hemley (2012) under similar thermodynamic conditions. Going forward, impressive advances may come from new laser shock facilities, but the results will likely continue to have large uncertainties. Nonetheless, we encourage such experiments to utilize any advances to verify the predictions that have already been made, such as those concerning the LLT and H-He demixing.

First-principles simulations will likely continue to play a crucial role in our understanding of hydrogen, helium, and other materials at both extreme and normal conditions. A small selection of the recent successes of simulations have been (i) the prediction of the reentrant nature of the melting line of molecular hydrogen, validated by several experiments; (ii) the prediction of a maximum compression (of ~4–4.5) along the principal Hugoniot of cryogenic deuterium, which

first was at variance with laser-induced shock experiments, but then later confirmed by several others; (iii) the prediction of a LLT using both CEIMC and FPMD, which, while it has received some experimental support, still requires a systematic experimental validation; and (iv) the prediction of the demixing temperature in H-He mixtures, results which can account for the differences in luminosity between Jupiter and Saturn. Other predictions have been made as well, but most still require experimental verification, such as the precise crystal structures and superconductivity in dense solid hydrogen.

Considering differences among simulation methods, away from metallization and molecular dissociation, FPMD and DFT methods are very accurate when compared to experiments and higher-level methods (e.g., CEIMC and RPIMC). As an example of their utility, there are programs underway to make a complete survey of the phase diagrams for all values of pressure, temperature, and composition using FPMD, as well as RPIMC. The metallization region though is of particular importance for planetary modeling, for fundamental physics understanding at low temperature, and for ICF applications at high temperature. This region highlights an important difference among simulation methods. Current FPMD methods, based on the GGA functional within DFT, have errors as a result of the limitations in treating excited states and band gaps. Quantitative predictions in this region thus require a more accurate description of electronic correlation, such as via QMC methods or the use of more sophisticated and complex functionals in DFT.

Considering QMC methods, in particular, one of the major issues of past simulations has been a lack of convergence, in terms of the number of particles, size of basis set(s), number of reciprocal lattice vectors, length of time of dynamics, etc. While it is true that the phases of hydrogen are very sensitive to such issues, the systematic growth in the power of the algorithms and computational resources means that it is now becoming possible to routinely eliminate such errors, which is refining our understanding of dense hydrogen. The fundamental bottleneck that remains in such methods though is the fermion sign problem that was briefly discussed in Sec. II. If this were solved, QMC methods could compute completely reliable solutions to the many-body quantum equations. Although such exact methods are either severely limited in the number of electrons or only give an upper bound to the internal energy. It is important to realize that progress can still be made via QMC methods, even without solving the sign problem. This is because, first, it is a scaling issue; it is possible to calculate exact properties of smaller systems (say dozens of atoms), a number which is expected to increase in the future, and these systems can then act as benchmarks for fixed-node QMC methods that scale to much larger sizes. Second, the variational fixed-node principle gives an absolute signal when one has improved the trial wave function (an upper bound principle is lacking in DFT); substantial progress has been made in finding better trial wave functions. Third, accumulated experience suggests that the fixed-node errors using existing trial wave functions are quite small for hydrogen and helium systems at high pressures, at least in the normal liquid and solid phases.

An important issue is the effect of the ZPM of the nuclei. Such effects are likely to be important, for example, on the metallization transition below $\sim$1000 K, since they become more relevant as the temperature is lowered. As another example, the inclusion of these effects can change the relative stability of the low-temperature solid phases altogether (Natoli, Martin, and Ceperley, 1993). It is important to realize that these effects cannot be described by approximate methods (e.g., the self-consistent harmonic approximations), and to achieve definitive predictions of ordered quantum states, such as a low- or zero-temperature quantum fluid or superconductivity, complete and rigorous treatments of hydrogen including ZPM will be needed.

Despite the successes of both simulations and experiments, many properties of hydrogen remain unresolved. Some of the most basic questions that need answering concern low-temperature behavior: A number of structures have been predicted for phases II, III, and IV of molecular hydrogen, but the agreement with experiment is not perfect; are they correct? And, are the predicted phases at pressures beyond III and IV correct as well? How does the IM transition occur, and is this related to the molecular-to-atomic transition? Are the recently proposed atomic structures via studies employing the harmonic approximation for ZPM correct? Or, does ZPM destabilize the solid lattice, giving a low- or zero-temperature quantum fluid? If not, at what pressure does the melting reach a minimum, and what is its value?

The use of advanced simulation methods, in particular, FPMD based on DFT, RPIMC, and CEIMC will play pivotal roles in answering the above questions. Most of the problems that have held back any progress have been solved to a large extent, allowing important questions to be addressed. For example, simulations can now calculate the EOS to the accuracy needed for planetary modeling; EOS tables accurate to a few percent are already available in certain regions of phase space. We anticipate that in the next few years the computation and testing of these will be completed, and that accurate equilibrium properties for arbitrary H-He mixtures may be available as well. As another example, advances in correlated methods can now compute properties such as electrical and thermal conductivity, viscosity, and opacity, which are vital ingredients not only in planetary models but also in many other applications of matter under extreme conditions.

## ACKNOWLEDGMENTS

We acknowledge the interactions with many colleagues with whom we have worked on these problems with over the years, including B. J. Alder, B. Bernu, S. Bonev, K. Delaney, M. Dewing, M. Holzmann, E. Liberatore, F. Lin, W. Magro, R. M. Martin, B. Militzer, V. Natoli, E. Schwegler, and I. Tamblyn. The writing of this review was funded by the DOE under Grant No. DE-FG52-09NA29456, the Erasmus Mundus Scholarship, by the Materials Computation Center at the University of Illinois at Urbana-Champaign, funded by NSF No. DMR-0325939. M. A. M. is funded in part under the auspices of the U.S. DOE by LLNL under Contract No. DE-AC52-07NA27344 and also acknowledges support from LDRD Grant No. 10-ERD-058. C. P. is supported by the Italian Institute of Technology (IIT) under the SEED project Grant No. 259 SIMBEDD.

## REFERENCES


Abrikosov, A. A., 1954, Astron. Zh. **31**, 112.

Akahama, Y., M. Nishimura, H. Kawamura, N. Hirao, Y. Ohishi, and K. Takemura, 2010, Phys. Rev. B **82**, 060101(R).

Alavi, A., J. Kohanoff, M. Parrinello, and D. Frenkel, 1994, Phys. Rev. Lett. **73**, 2599.

Allen, P. B., and M. Cardona, 1981a, Phys. Rev. B **24**, 7479.

Allen, P. B., and M. Cardona, 1981b, Phys. Rev. B **23**, 1495.

Allen, P. B., and R. C. Dynes, 1975, Phys. Rev. B **12**, 905.

Ashcroft, N., and D. Stroud, 1978, *Solid State Physics* (Academic Press, New York), Vol. 33, p. 1.

Ashcroft, N. W., 1968, Phys. Rev. Lett. **21**, 1748.

Ashcroft, N. W., 2000, J. Phys. Condens. Matter **12**, A129.

Ashcroft, N. W., 2003, J. Phys. A **36**, 6137.

Ashcroft, N. W., and N. D. Mermin, 1976, *Solid State Physics* (Holt, Rinehart and Winston, New York).

Attaccalite, C., and S. Sorella, 2008, Phys. Rev. Lett. **100**, 114501.

Aziz, R. A., and M. J. Slaman, 1991, J. Chem. Phys. **94**, 8047.

Babaev, E., A. Sudbø, and N. W. Ashcroft, 2004, Nature (London) **431**, 666.

Baer, B. J., W. J. Evans, and C.-S. Yoo, 2007, Phys. Rev. Lett. **98**, 235503.

Baer, B. J., W. J. Evans, and C.-S. Yoo, 2009, Phys. Rev. Lett. **102**, 209901(E).

Bagnier, S., P. Blottiau, and J. Clérouin, 2000, Phys. Rev. E **63**, 015301(R).

Bahcall, J. N., M. H. Pinsonneault, and G. J. Wasserburg, 1995, Rev. Mod. Phys. **67**, 781.

Bailey, J., M. Knudson, A. Carlson, G. Dunham, M. Desjarlais, D. Hanson, and J. Asay, 2008, Phys. Rev. B **78**, 144107.

Bajdich, M., L. Mitas, G. Drobný, L. K. Wagner, and K. E. Schmidt, 2006, Phys. Rev. Lett. **96**, 130201.

Baraffe, I., G. Chabrier, and T. Barman, 2010, Rep. Prog. Phys. **73**, 016901.

Barbee, III, T. W., and M. L. Cohen, 1991, Phys. Rev. B **44**, 11 563.

Barbee, III, T. W., A. García, M. L. Cohen, and J. L. Martins, 1989, Phys. Rev. Lett. **62**, 1150.

Bardeen, J., L. N. Cooper, and J. R. Schrieffer, 1957, Phys. Rev. **108**, 1175.

Barker, J. A., 1979, J. Chem. Phys. **70**, 2914.

Becke, A. D., 1993, J. Chem. Phys. **98**, 5648.

Belov, S., G. Boriskov, A. Bykov, R. Il'Kaev, N. Luk'yanov, A. Matveev, O. Mikhailova, V. Selemir, G. Simakov, and R. Trunin, 2002, JETP Lett. **76**, 433.

Bernu, B., D. M. Ceperley, and W. A. Lester, 1990, J. Chem. Phys. **93**, 552.

Beule, D., W. Ebeling, A. Förster, H. Juranek, R. Redmer, and G. Röpke, 1999, Contrib. Plasma Phys. **39**, 21.

Boehly, T., D. Hicks, P. Celliers, T. Collins, R. Earley, J. Eggert, D. Jacobs-Perkins, S. Moon, E. Vianello, and D. Meyerhofer, 2004, Phys. Plasmas **11**, L49.

Bonev, S., E. Schwegler, T. Ogitsu, and G. Galli, 2004, Nature (London) **431**, 669.

Bonev, S. A., B. Militzer, and G. Galli, 2004, Phys. Rev. B **69**, 014101.

Boriskov, G., A. Bykov, R. Il'Kaev, V. Selemir, G. Simakov, R. Trunin, V. Urlin, V. Fortov, and A. Shuikin, 2003, Dokl. Phys. **48**, 553.

Boriskov, G., A. Bykov, R. Il'Kaev, V. Selemir, G. Simakov, R. Trunin, V. Urlin, A. Shuikin, and W. Nellis, 2005, Phys. Rev. B **71**, 092104.

Born, M., and R. Oppenheimer, 1927, Ann. Phys. (Leipzig) **389**, 457.

Brothers, E. N., A. F. Izmaylov, J. O. Normand, V. Barone, and G. E. Scuseria, 2008, J. Chem. Phys. **129**, 011102.

Brovman, E. G., Y. Kagan, and A. Kholas, 1972a, Sov. Phys. JETP **34**, 1300.

Brovman, E. G., Y. Kagan, and A. Kholas, 1972b, Sov. Phys. JETP **35**, 783.

Brush, S. G., H. L. Sahlin, and E. Teller, 1966, J. Chem. Phys. **45**, 2102.

Burke, K., 2012, J. Chem. Phys. **136**, 150901.

Burrows, A., W. B. Hubbard, J. I. Lunine, and J. Liebert, 2001, Rev. Mod. Phys. **73**, 719.

Caillabet, L., S. Mazevet, and P. Loubeyre, 2011, Phys. Rev. B **83**, 094101.

Cao, J., and B. J. Berne, 1993, J. Chem. Phys. **99**, 2902.

Car, R., and M. Parrinello, 1985, Phys. Rev. Lett. **55**, 2471.

Carbotte, J. P., 1990, Rev. Mod. Phys. **62**, 1027.

Casula, M., C. Attaccalite, and S. Sorella, 2004, J. Chem. Phys. **121**, 7110.

Celliers, P., G. Collins, L. D. Silva, D. Gold, R. Cauble, R. Wallace, M. Foord, and B. Hammel, 2000, Phys. Rev. Lett. **84**, 5564.

Celliers, P. M., P. Loubeyre, J. H. Eggert, S. Brygoo, R. S. McWilliams, D. G. Hicks, T. R. Boehly, R. Jeanloz, and G. W. Collins, 2010, Phys. Rev. Lett. **104**, 184503.

Ceperley, D., M. Dewing, and C. Pierleoni, 2002, in *Bridging Time Scales: Molecular Simulations for the Next Decade*, edited by P. Nielaba, M. Mareschal, and G. Ciccotti, Topics in Condensed Matter Physics Vol. 605 (Springer-Verlag, Berlin), p. 473.

Ceperley, D. M., 1988, *Quantum Monte Carlo Simulation of Systems at High Pressure* (Plenum, New York).

Ceperley, D. M., 1992, Phys. Rev. Lett. **69**, 331.

Ceperley, D. M., 1995, Rev. Mod. Phys. **67**, 279.

Ceperley, D. M., 1996, in *Monte Carlo and Molecular Dynamics of Condensed Matter Systems*, edited by K. Binder, and G. Ciccotti (Editrice Compositori, Bologna).

Ceperley, D. M., and B. J. Alder, 1980, Phys. Rev. Lett. **45**, 566.

Ceperley, D. M., and B. J. Alder, 1981, Physica (Amsterdam) **108B + C**, 875.

Ceperley, D. M., and B. J. Alder, 1987, Phys. Rev. B **36**, 2092.

Ceperley, D. M., and B. Bernu, 1988, J. Chem. Phys. **89**, 6316.

Ceperley, D. M., G. V. Chester, and M. H. Kalos, 1977, Phys. Rev. B **16**, 3081.

Ceperley, D. M., G. V. Chester, and M. H. Kalos, 1978, Phys. Rev. B **17**, 1070.

Ceperley, D. M., and M. Dewing, 1999, J. Chem. Phys. **110**, 9812.

Ceperley, D. M., and H. Partridge, 1986, J. Chem. Phys. **84**, 820.

Ceriotti, M., D. E. Manolopoulos, and M. Parrinello, 2011, J. Chem. Phys. **134**, 084104.

Ceriotti, M., M. Parrinello, T. E. Markland, and D. E. Manolopoulos, 2010, J. Chem. Phys. **133**, 124104.

Chabrier, G., D. Saumon, and C. Winisdoerffer, 2007, Astrophys. Space Sci. **307**, 263.

Chacham, H., and S. G. Louie, 1991, Phys. Rev. Lett. **66**, 64.

Chacham, H., X. Zhu, and S. G. Louie, 1992, Phys. Rev. B **46**, 6688.

Chakravarty, S., and N. W. Ashcroft, 1978, Phys. Rev. B **18**, 4588.

Chen, Q., Y. Zhang, L. Cai, Y. Gu, and F. Jing, 2007, Phys. Plasmas **14**, 012703.

Chiesa, S., D. M. Ceperley, R. M. Martin, and M. Holzmann, 2006, Phys. Rev. Lett. **97**, 076404.

Clark, B. K., M. A. Morales, J. McMinis, J. Kim, and G. E. Scuseria, 2011, J. Chem. Phys. **135**, 244105.

Clouter, M., and H. P. Gush, 1965, Phys. Rev. Lett. **15**, 200.

Collins, G., P. Celliers, L. D. Silva, R. Cauble, D. Gold, M. Foord, N. Holmes, B. Hammel, R. Wallace, and A. Ng, 2001, Phys. Rev. Lett. **87**, 165504.

Collins, G. W., L. B. Da Silva, P. Celliers, D. Gold, M. Foord, R. Wallace, A. Ng, S. Weber, K. Budil, and R. Cauble, 1998, Science **281**, 1178.

Collins, L., J. Kress, I. Kwon, W. Windl, T. Lenosky, N. Troullier, and R. Bauer, 1998, J. Comput. Aided Mater. Des. **5**, 173.

Collins, L., I. Kwon, J. Kress, N. Troullier, and D. Lynch, 1995, Phys. Rev. E **52**, 6202.

Collins, L. A., S. R. Bickham, J. D. Kress, S. Mazevet, N. J. Troullier, and W. Windl, 2001, Phys. Rev. B **63**, 184110.

Collins, G. W., *et al.*, 1998, Phys. Plasmas **5**, 1864.

Conrath, B. J., and D. Gautier, 2000, Icarus **144**, 124.

Cudazzo, P., G. Profeta, A. Sanna, A. Floris, A. Continenza, S. Massidda, and E. K. U. Gross, 2008, Phys. Rev. Lett. **100**, 257001.

Cudazzo, P., G. Profeta, A. Sanna, A. Floris, A. Continenza, S. Massidda, and E. K. U. Gross, 2010a, Phys. Rev. B **81**, 134505.

Cudazzo, P., G. Profeta, A. Sanna, A. Floris, A. Continenza, S. Massidda, and E. K. U. Gross, 2010b, Phys. Rev. B **81**, 134506.

Cui, L., N. H. Chen, and I. F. Silvera, 1995, Phys. Rev. B **51**, 14 987.

Cui, T., E. Cheng, B. J. Alder, and K. B. Whaley, 1997, Phys. Rev. B **55**, 12 253.

Da Silva, L. B., *et al.*, 1997, Phys. Rev. Lett. **78**, 483.

Datchi, F., P. Loubeyre, and R. LeToullec, 2000, Phys. Rev. B **61**, 6535.

Deemyad, S., and I. F. Silvera, 2008, Phys. Rev. Lett. **100**, 155701.

Delaney, K., C. Pierleoni, and D. Ceperley, 2006, Phys. Rev. Lett. **97**, 235702.

De Raedt, H., and B. De Raedt, 1983, Phys. Rev. A **28**, 3575.

Desjarlais, M., 2003, Phys. Rev. B **68**, 064204.

Dharma-wardana, M. W. C., and F. m. c. Perrot, 2002, Phys. Rev. B **66**, 014110.

Diatschenko, V., and C. W. Chu, 1981, Science **212**, 1393.

Diatschenko, V., C. W. Chu, D. H. Liebenberg, D. A. Young, M. Ross, and R. L. Mills, 1985, Phys. Rev. B **32**, 381.

Dick, R., and G. Kerley, 1980, J. Chem. Phys. **73**, 5264.

Dion, M., H. Rydberg, E. Schröder, D. C. Langreth, and B. I. Lundqvist, 2004, Phys. Rev. Lett. **92**, 246401.

Driver, K., and B. Militzer, 2012, Phys. Rev. Lett. **108**, 115502.

Drummond, N., R. J. Needs, A. Sorouri, and M. Foulkes, 2008, Phys. Rev. B **78**, 125106.

Drummond, N. D., and R. J. Needs, 2005, Phys. Rev. B **72**, 085124.

Dugdale, J. S., and F. E. Simon, 1953, Proc. R. Soc. A **218**, 291.

Dykstra, C., 2005, *Theory and Applications of Computational Chemistry: The First Forty Years* (Elsevier, New York).

Dynes, R. C., 1972, Solid State Commun. **10**, 615.

Ebeling, W., and W. Richert, 1985, Phys. Status Solidi B **128**, 467.

Ebeling, W., and W. Richert, 1985, Phys. Lett. **108A**, 80.

Ebina, K., and H. Miyagi, 1989, Phys. Lett. A **142**, 237.

Edwards, B., N. W. Ashcroft, and T. Lenosky, 1996, Europhys. Lett. **34**, 519.

Edwards, P. P., M. T. J. Lodge, F. Hensel, and R. Redmer, 2010, Phil. Trans. R. Soc. A **368**, 941.

Eggert, J., S. Brygoo, P. Loubeyre, R. S. McWilliams, P. M. Celliers, D. G. Hicks, T. R. Boehly, R. Jeanloz, and G. W. Collins, 2008, Phys. Rev. Lett. **100**, 124503.

Ercolessi, F., and J. B. Adams, 1994, Europhys. Lett. **26**, 583.

Eremets, M., and I. Trojan, 2009, JETP Lett. **89**, 174.

Eremets, M. I., and I. A. Troyan, 2011, Nature Mater. **10**, 927.

Feller, W., 1968, *An Introduction to Probability Theory and its Applications* (Wiley, New York).

Felsteiner, J., 1965, Phys. Rev. Lett. **15**, 1025.

Fermi, E., 1927, Rend. Accad. Naz. Lincei **6**, 602.

Feynman, R., 1939, Phys. Rev. **56**, 340.

Feynman, R., 1972, *Statistical Mechanics: A Set of Lectures*, Frontiers in Physics (W. A. Benjamin, New York).

Feynman, R., and A. Hibbs, 1965, *Quantum Mechanics and Path Integrals* (McGraw-Hill, New York).

Filinov, V., M. Bonitz, P. Levashov, V. Fortov, W. Ebeling, M. Schlanges, and S. Koch, 2003, J. Phys. A **36**, 6069.

Filinov, V., P. Levashov, M. Bonitz, and V. Fortov, 2005, Plasma Phys. Rep. **31**, 700.

Fiolhais, C., F. Nogueira, and M. Marques, 2003, *A Primer in Density Functional Theory*, Lecture Notes in Physics (Springer, New York).

Fortney, J., 2004, Science **305**, 1414.

Fortney, J., and N. Nettelmann, 2010, Space Sci. Rev. **152**, 423.

Fortney, J. J., and W. Hubbard, 2004, Astrophys. J. **608**, 1039.

Fortney, J. J., and W. B. Hubbard, 2003, Icarus **164**, 228.

Fortov, V. E., *et al.*, 2007, Phys. Rev. Lett. **99**, 185001.

Fortov, V. E., V. Y. Ternovoi, M. V. Zhernokletov, M. A. Mochalov, A. L. Mikhailov, A. S. Filimonov, A. A. Pyalling, V. B. Mintsev, V. K. Gryaznov, and I. L. Iosilevskii, 2003, JETP **97**, 259.

Foulkes, W. M. C., L. Mitas, R. J. Needs, and G. Rajagopal, 2001, Rev. Mod. Phys. **73**, 33.

Franz, R., and G. Wiedemann, 1853, Ann. Phys. (Leipzig) **165**, 497.

Freiman, Y. A., S. M. Tretyak, T. N. Antsygina, and R. J. Hemley, 2003, J. Low Temp. Phys. **133**, 251.

Frenkel, D., and B. Smit, 2002, *Understanding Molecular Simulation: From Algorithms to Applications* (Academic Press, New York), 2nd ed.

Friedli, C., and N. W. Ashcroft, 1977, Phys. Rev. B **16**, 662.

Galam, S., and J.-P. Hansen, 1976, Phys. Rev. A **14**, 816.

Galli, G., R. Hood, A. Hazi, and F. Gygi, 2000, Phys. Rev. B **61**, 909.

Geneste, G., M. Torrent, F. Bottin, and P. Loubeyre, 2012, Phys. Rev. Lett. **109**, 155303.

Geng, H. Y., H. X. Song, J. F. Li, and Q. Wu, 2012, J. Appl. Phys. **111**, 063510.

Giuliani, G., and G. Vignale, 2005, *Quantum Theory of the Electron Liquid* (Cambridge University Press, Cambridge, England).

Goncharenko, I., and P. Loubeyre, 2005, Nature (London) **435**, 1206.

Goncharov, A. F., E. Gregoryanz, R. J. Hemley, and H. k. Mao, 2001, Proc. Natl. Acad. Sci. U.S.A. **98**, 14 234.

Goncharov, A. F., and R. J. Hemley, 2006, Chem. Soc. Rev. **35**, 899.

Goncharov, A. F., R. J. Hemley, and H. k. Mao, 2011, J. Chem. Phys. **134**, 174501.

Goncharov, A. F., R. J. Hemley, H. k. Mao, and J. Shu, 1998, Phys. Rev. Lett. **80**, 101.

Goncharov, A. F., I. I. Mazin, J. H. Eggert, R. J. Hemley, and H. k. Mao, 1995, Phys. Rev. Lett. **75**, 2514.

Greenwood, D. A., 1958, Proc. Phys. Soc. London **71**, 585.

Gregoryanz, E., A. F. Goncharov, K. Matsuishi, H.-k. Mao, and R. J. Hemley, 2003, Phys. Rev. Lett. **90**, 175701.

Grishechkin, S., S. Gruzdev, V. Gryaznov, M. Zhernokletov, R. Il'Kaev, I. Iosilevskii, G. Kashintseva, S. Kirshanov, S. Manachkin, and V. Mintsev, 2004a, JETP Lett. **80**, 398.

Grishechkin, S., *et al.*, 2004b, JETP Lett. **80**, 398.

Guillot, T., 1999, Planet. Space Sci. **47**, 1183.

Guillot, T., 2005, Annu. Rev. Earth Planet Sci. **33**, 493.

Guillot, T., G. Chabrier, P. Morel, and D. Gautier, 1994, Icarus **112**, 354.

Guillot, T., D. Gautier, G. Chabrier, and B. Mosser, 1994, Icarus **112**, 337.

Guillot, T., D. Gautier, and W. B. Hubbard, 1997, Icarus **130**, 534.

Guillot, T., and A. P. Showman, 2002, Astron. Astrophys. **385**, 156.

Hafner, J., 2008, J. Comput. Chem. **29**, 2044.

Hamel, S., M. A. Morales, and E. Schwegler, 2011, Phys. Rev. B **84**, 165110.

Hanfland, M., R. J. Hemley, and H.-k. Mao, 1993, Phys. Rev. Lett. **70**, 3760.

Hansen, J. P., 1973, Phys. Rev. A **8**, 3096.
Hansen, J. P., and I. R. McDonald, 1981, Phys. Rev. A **23**, 2041.
Hansen, J. P., I. R. McDonald, and E. L. Pollock, 1975, Phys. Rev. A **11**, 1025.
Hansen, J. P., G. M. Torrie, and P. Vieillefosse, 1977, Phys. Rev. A **16**, 2153.
Hawke, P., T. Burgess, D. Duerre, J. Huebel, R. Keeler, H. Klapper, and W. Wallace, 1978, Phys. Rev. Lett. **41**, 994.
Hazen, R. M., H. K. Mao, L. W. Finger, and R. J. Hemley, 1987, Phys. Rev. B **36**, 3944.
Hellmann, H., 1937, *Einfuhrung in die Quantumchemie* (Franz Duetsche, Leipzig).
Hemley, R. J., and H. K. Mao, 1988, Phys. Rev. Lett. **61**, 857.
Heyd, J., G. E. Scuseria, and M. Ernzerhof, 2003, J. Chem. Phys. **118**, 8207.
Hicks, D., T. Boegly, P. Celliers, J. Eggert, S. Moon, D. Meyerhofer, and G. Collins, 2009, Phys. Rev. B **79**, 014112.
Hohenberg, P., and W. Kohn, 1964, Phys. Rev. **136**, B864.
Hohl, D., V. Natoli, D. M. Ceperley, and R. M. Martin, 1993, Phys. Rev. Lett. **71**, 541.
Holmes, N., M. Ross, and W. Nellis, 1995, Phys. Rev. B **52**, 15 835.
Holst, B., M. French, and R. Redmer, 2011, Phys. Rev. B **83**, 235120.
Holst, B., R. Redmer, and M. Desjarlais, 2008, Phys. Rev. B **77**, 184201.
Holzmann, M., B. Bernu, and D. M. Ceperley, 2011, J. Phys. Conf. Ser. **321**, 012020.
Holzmann, M., D. M. Ceperley, C. Pierleoni, and K. Esler, 2003, Phys. Rev. E **68**, 046707.
Howie, R. T., C. L. Guillaume, T. Scheler, A. F. Goncharov, and E. Gregoryanz, 2012, Phys. Rev. Lett. **108**, 125501.
Hu, S., B. Militzer, V. Goncharov, and S. Skupsky, 2011, Phys. Rev. B **84**, 224109.
Hubbard, W. B., 1972, Astrophys. J. **176**, 525.
Hubbard, W. B., and H. E. DeWitt, 1985, Astrophys. J. **290**, 388.
Hubbard, W. B., T. Guillot, M. S. Marley, A. Burrows, J. I. Lunine, and D. S. Saumon, 1999, Planet. Space Sci. **47**, 1175.
Hubbard, W. B., and W. L. Slattery, 1971, Astrophys. J. **168**, 131.
Huotari, S., *et al.*, 2010, Phys. Rev. Lett. **105**, 086403.
Hutter, J., M. E. Tuckerman, and M. Parrinello, 1995, J. Chem. Phys. **102**, 859.
Ichimaru, S., 1982, Rev. Mod. Phys. **54**, 1017.
Jaffe, J. E., and N. W. Ashcroft, 1981, Phys. Rev. B **23**, 6176.
Jaffe, J. E., and N. W. Ashcroft, 1983, Phys. Rev. B **27**, 5852.
Jeanloz, R., P. Celliers, G. Collins, J. Eggert, K. Lee, R. McWilliams, S. Brygoo, and P. Loubeyre, 2007, Proc. Natl. Acad. Sci. U.S.A. **104**, 9172.
Jephcoat, A. P., 2011, Nature Mater. **10**, 904.
Johnson, K. A., and N. W. Ashcroft, 2000, Nature (London) **403**, 632.
Jones, M. D., and D. M. Ceperley, 1996, Phys. Rev. Lett. **76**, 4572.
Jones, R. O., and O. Gunnarsson, 1989, Rev. Mod. Phys. **61**, 689.
Juranek, H., and R. Redmer, 2000, J. Chem. Phys. **112**, 3780.
Juranek, H., V. Schwarz, and R. Redmer, 2003, J. Phys. A **36**, 6181.
Kagan, Y., V. V. Pushkarev, and A. Kholas, 1977, Sov. Phys. JETP **46**, 511.
Kaxiras, E., and J. Broughton, 1992, Europhys. Lett. **17**, 151.
Kaxiras, E., J. Broughton, and R. J. Hemley, 1991, Phys. Rev. Lett. **67**, 1138.
Kechin, V. V., 2004a, JETP Lett. **79**, 40.
Kechin, V. V., 2004b, J. Phys. Condens. Matter **16**, L125.
Keesom, W. H., J. de Smedt, and H. H. Mooy, 1930, Commun. Kamerlingh Onnes Lab., Univ. Leiden **19**, 2090.
Kerley, G. I., 1972, Phys. Earth Planet. Inter. **6**, 78.
Kerley, G. I., 2003 (unpublished).
Khairallah, S., J. Shumway, and E. Draeger, 2011, arXiv:1108.1711.
Khairallah, S. A., and B. Militzer, 2008, Phys. Rev. Lett. **101**, 106407.
Kietzmann, A., B. Holst, R. Redmer, M. P. Desjarlais, and T. R. Mattsson, 2007, Phys. Rev. Lett. **98**, 190602.
Kitaigorodskii, A. I., and K. V. Mirskaya, 1965, Sov. Phys. Crystallogr. **10**, 121.
Kitamura, H., and S. Ichimaru, 1998, J. Phys. Soc. Jpn. **67**, 950.
Kitamura, H., S. Tsuneyuki, T. Ogitsu, and T. Miyake, 2000, Nature (London) **404**, 259.
Klakow, D., C. Toepffer, and P. Reinhard, 1994a, J. Chem. Phys. **101**, 10 766.
Klakow, D., C. Toepffer, and P.-G. Reinhard, 1994b, Phys. Lett. A **192**, 55.
Klepeis, J. E., K. J. Schafer, T. W. Barbee, and M. Ross, 1991, Science **254**, 986.
Knaup, M., P. Reinhard, C. Toepffer, and G. Zwicknagel, 2003, J. Phys. A **36**, 6165.
Knudson, M., and M. Desjarlais, 2009, Phys. Rev. Lett. **103**, 225501.
Knudson, M., D. Hanson, J. Bailey, C. Hall, and J. Asay, 2003, Phys. Rev. Lett. **90**, 35 505.
Knudson, M., D. Hanson, J. Bailey, C. Hall, J. Asay, and W. Anderson, 2001, Phys. Rev. Lett. **87**, 225501.
Knudson, M., D. Hanson, J. Bailey, C. Hall, J. Asay, and C. Deeney, 2004, Phys. Rev. B **69**, 144209.
Kohanoff, J., 2006, *Electronic Structure Calculation for Solids and Molecules* (Cambridge University Press, Cambridge, England).
Kohanoff, J., and J. Hansen, 1995, Phys. Rev. Lett. **74**, 626.
Kohanoff, J., and J. Hansen, 1996, Phys. Rev. E **54**, 768.
Kohanoff, J., S. Scandolo, G. L. Chiarotti, and E. Tosatti, 1997, Phys. Rev. Lett. **78**, 2783.
Kohn, W., and L. Sham, 1965, Phys. Rev. **140**, A1133.
Koi, L., R. Ahuja, A. B. Belonoshko, and B. Johansson, 2007, J. Phys. Condens. Matter **19**, 016206.
Kowalski, P. M., S. Mazevet, D. Saumon, and M. Challacombe, 2007, Phys. Rev. B **76**, 075112.
Kubo, R., 1957, J. Phys. Soc. Jpn. **12**, 570.
Kümmel, S., and L. Kronik, 2008, Rev. Mod. Phys. **80**, 3.
Kwon, I., L. Collins, J. Kress, and N. Troullier, 1995, Europhys. Lett. **29**, 537.
Kwon, I., L. A. Collins, J. D. Kress, N. Troullier, and D. L. Lynch, 1994, Phys. Rev. E **49**, R4771.
Kwon, I., J. Kress, and L. Collins, 1994, Phys. Rev. B **50**, 9118.
Kwon, Y., D. M. Ceperley, and R. M. Martin, 1993, Phys. Rev. B **48**, 12 037.
Labet, V., P. Gonzalez-Morelos, R. Hoffmann, and N. W. Ashcroft, 2012, J. Chem. Phys. **136**, 074501.
Labet, V., R. Hoffmann, and N. W. Ashcroft, 2012a, J. Chem. Phys. **136**, 074502.
Labet, V., R. Hoffmann, and N. W. Ashcroft, 2012b, J. Chem. Phys. **136**, 074503.
Labet, V., R. Hoffmann, and N. W. Ashcroft, 2012c, J. Chem. Phys. **136**, 074504.
Lambert, F., V. Recoules, A. Decoster, J. Clerouin, and M. Desjarlais, 2011, Phys. Plasmas **18**, 056306.
Landau, L., and G. Zeldovich, 1943, Acta Phys.-Chim. USSR **18**, 194.
Lee, K., E. D. Murray, L. Kong, B. I. Lundqvist, and D. C. Langreth, 2010, Phys. Rev. B **82**, 081101.
Lenosky, T., S. Bickham, J. Kress, and L. Collins, 2000, Phys. Rev. B **61**, 1.
Lenosky, T., J. Kress, and L. Collins, 1997, Phys. Rev. B **56**, 5164.

Lenosky, T., J. Kress, L. Collins, and I. Kwon, 1997a, Phys. Rev. B **55**, R11 907.
Lenosky, T., J. Kress, L. Collins, and I. Kwon, 1997b, J. Quant. Spectrosc. Radiat. Transfer **58**, 743.
Lenosky, T., J. Kress, L. Collins, R. Redmer, and H. Juranek, 1999, Phys. Rev. E **60**, 1665.
Liberatore, E., M. A. Morales, D. M. Ceperley, and C. Pierleoni, 2011, Mol. Phys. **109**, 3029.
Liberatore, E., C. Pierleoni, and D. M. Ceperley, 2011, J. Chem. Phys. **134**, 184505.
Liebenberg, D. H., R. L. Mills, and J. C. Bronson, 1978, Phys. Rev. B **18**, 4526.
Lin, C., F.-H. Zong, and D. M. Ceperley, 2001, Phys. Rev. E **64**, 016702.
Lin, F., M. A. Morales, K. T. Delaney, C. Pierleoni, R. M. Martin, and D. M. Ceperley, 2009, Phys. Rev. Lett. **103**, 256401.
Lin, J.-F., M. Santoro, V. V. Struzhkin, H.-k. Mao, and R. J. Hemley, 2004, Rev. Sci. Instrum. **75**, 3302.
Lindl, J. D., P. Amendt, R. L. Berger, S. G. Glendinning, S. H. Glenzer, S. W. Haan, R. L. Kauffman, O. L. Landen, and L. J. Suter, 2004, Phys. Plasmas **11**, 339.
Liu, H., H. Wang, and Y. Ma, 2012, J. Phys. Chem. C **116**, 9221.
Liu, H., L. Zhu, W. Cui, and Y. Ma, 2012, J. Chem. Phys. **137**, 074501.
Lorenzana, H. E., I. F. Silvera, and K. A. Goettel, 1989, Phys. Rev. Lett. **63**, 2080.
Lorenzana, H. E., I. F. Silvera, and K. A. Goettel, 1990, Phys. Rev. Lett. **64**, 1939.
Lorenzen, W., B. Holst, and R. Redmer, 2009, Phys. Rev. Lett. **102**, 115701.
Lorenzen, W., B. Holst, and R. Redmer, 2010, Phys. Rev. B **82**, 195107.
Lorenzen, W., B. Holst, and R. Redmer, 2011, Phys. Rev. B **84**, 235109.
Loubeyre, P., J. M. Besson, J. P. Pinceaux, and J. P. Hansen, 1982, Phys. Rev. Lett. **49**, 1172.
Loubeyre, P., P. Celliers, D. Hicks, E. Henry, A. Dewaele, J. Pasley, J. Eggert, M. Koenig, F. Occelli, and K. Lee, 2004, High Press. Res. **24**, 25.
Loubeyre, P., R. LeToullec, J. P. Pinceaux, H. K. Mao, J. Hu, and R. J. Hemley, 1993, Phys. Rev. Lett. **71**, 2272.
Loubeyre, P., F. Occelli, and R. LeToullec, 2002, Nature (London) **416**, 613.
Lüders, M., M. A. L. Marques, N. N. Lathiotakis, A. Floris, G. Profeta, L. Fast, A. Continenza, S. Massidda, and E. K. U. Gross, 2005, Phys. Rev. B **72**, 024545.
Magro, W., D. Ceperley, C. Pierleoni, and B. Bernu, 1996, Phys. Rev. Lett. **76**, 1240.
Maksimov, E. G., and Y. I. Shilov, 1999, Phys. Usp. **42**, 1121.
Mao, H., and R. Hemley, 1989, Science **244**, 1462.
Mao, H. K., R. J. Hemley, Y. Wu, A. P. Jephcoat, L. W. Finger, C. S. Zha, and W. A. Bassett, 1988, Phys. Rev. Lett. **60**, 2649.
Mao, H.-k., and R. J. Hemley, 1994, Rev. Mod. Phys. **66**, 671.
Marley, M. S., and W. B. Hubbard, 1988, Icarus **73**, 536.
Martin, R. M., 2004, *Electronic Structure: Basic Theory and Practical Methods* (Cambridge University Press, Cambridge, England).
Martyna, G. J., D. J. Tobias, and M. L. Klein, 1994, J. Chem. Phys. **101**, 4177.
Marx, D., and J. Hutter, 2000, *Modern Methods and Algorithms of Quantum Chemistry* (NIC, FZ, Jülich), p. 301.
Marx, D., and J. Hutter, 2009, *Ab initio Molecular Dynamics: Basic Theory and Advanced Methods* (Cambridge University Press, Cambridge, England).
Marx, D., and M. Parrinello, 1996, J. Chem. Phys. **104**, 4077.
Matsuishi, K., E. Gregoryanz, H. Mao, and R. Hemley, 2003, J. Chem. Phys. **118**, 10 683.
Mattsson, A. E., P. A. Schultz, M. P. Desjarlais, T. R. Mattsson, and K. Leung, 2005, Model. Simul. Mater. Sci. Eng. **13**, R1.
Mazin, I. I., and R. E. Cohen, 1995, Phys. Rev. B **52**, R8597.
McGrath, M. J., J. I. Siepmann, I.-F. W. Kuo, C. J. Mundy, J. VandeVondele, J. Hutter, F. Mohamed, and M. Krack, 2006, J. Phys. Chem. A **110**, 640.
McMahon, J. M., and D. M. Ceperley, 2011a, Phys. Rev. Lett. **106**, 165302.
McMahon, J. M., and D. M. Ceperley, 2011b, Phys. Rev. B **84**, 144515.
McMahon, J. M., and D. M. Ceperley, 2012, Phys. Rev. B **85**, 219902.
McMillan, W. L., 1965, Phys. Rev. **138**, A442.
McMillan, W. L., 1968, Phys. Rev. **167**, 331.
Mermin, D., 1965, Phys. Rev. **137**, A1441.
Metropolis, N., A. W. Rosenbluth, M. N. Rosenbluth, A. H. Teller, and E. Teller, 1953, J. Chem. Phys. **21**, 1087.
Militzer, B., 2005, J. Low Temp. Phys. **139**, 739.
Militzer, B., 2006, Phys. Rev. Lett. **97**, 175501.
Militzer, B., 2009, Phys. Rev. B **79**, 155105.
Militzer, B., and D. Ceperley, 2000, Phys. Rev. Lett. **85**, 1890.
Militzer, B., and D. Ceperley, 2001, Phys. Rev. E **63**, 066404.
Militzer, B., D. Ceperley, J. Kress, J. Johnson, L. Collins, and S. Mazevet, 2001, Phys. Rev. Lett. **87**, 275502.
Militzer, B., W. B. Hubbard, J. Vorberger, I. Tamblyn, and S. A. Bonev, 2008, Astrophys. J. **688**, L45.
Mills, R. L., and A. F. Schuch, 1965, Phys. Rev. Lett. **15**, 722.
Mills, R. L., J. L. Yarnell, and A. F. Schuch, 1973 (Plenum, New York), Vol. 2, p. 202.
Mon, K. K., G. V. Chester, and N. W. Ashcroft, 1980, Phys. Rev. B **21**, 2641.
Mon, K. K., G. V. Chester, and N. W. Ashcroft, 1983, Phys. Rev. B **27**, 3895.
Moraldi, M., 2009, Phys. Rev. B **80**, 134117.
Morales, M. A., 2009, Ph.D. thesis, University of Illinois at Urbana-Champaign.
Morales, M. A., L. X. Benedict, D. S. Clark, E. Schwegler, I. Tamblyn, S. A. Bonev, A. A. Correa, and S. W. Haan, 2012, High Energy Density Phys. **8**, 5.
Morales, M. A., C. Pierleoni, and D. M. Ceperley, 2010a, Phys. Rev. E **81**, 021202.
Morales, M. A., C. Pierleoni, E. Schwegler, and D. M. Ceperley, 2010b, Proc. Natl. Acad. Sci. U.S.A. **107**, 12 799.
Morales, M. A., E. Schwegler, D. Ceperley, C. Pierleoni, S. Hamel, and K. Caspersen, 2009, Proc. Natl. Acad. Sci. U.S.A. **106**, 1324.
Moshary, F., N. H. Chen, and I. F. Silvera, 1993, Phys. Rev. Lett. **71**, 3814.
Mostovych, A., Y. Chan, T. Lehecha, L. Phillips, A. Schmitt, and J. Sethian, 2001, Phys. Plasmas **8**, 2281.
Mostovych, A., Y. Chan, T. Lehecha, A. Schmitt, and J. Sethian, 2000, Phys. Rev. Lett. **85**, 3870.
Moulopoulos, K., and N. W. Ashcroft, 1999, Phys. Rev. B **59**, 12 309.
Nabi, Z., L. Vitos, B. Johansson, and R. Ahuja, 2005, Phys. Rev. B **72**, 172102.
Nagao, K., S. Bonev, B. A., and N. Ashcroft, 2003, Phys. Rev. Lett. **90**, 35501.
Nagao, K., H. Nagara, and S. Matsubara, 1997, Phys. Rev. B **56**, 2295.
Nagao, K., T. Takezawa, and H. Nagara, 1999, Phys. Rev. B **59**, 13 741.

Nagara, H., 1989, J. Phys. Soc. Jpn. **58**, 3861.
Nagara, H., and T. Nakamura, 1992, Phys. Rev. Lett. **68**, 2468.
Nakamura, T., 1955, Prog. Theor. Phys. **14**, 135.
Natoli, V., and D. M. Ceperley, 1995, J. Comput. Phys. **117**, 171.
Natoli, V., R. M. Martin, and D. M. Ceperley, 1993, Phys. Rev. Lett. **70**, 1952.
Natoli, V., R. M. Martin, and D. M. Ceperley, 1995, Phys. Rev. Lett. **74**, 1601.
Nellis, W., A. Louis, N. Ashcroft, R. Johnston, C. Rao, D. Tunstall, H. von Lohneysen, P. Edwards, and D. Logan, 1998, Philos. Trans. Ser. A, Math. Phys. Eng. Sci. **356**, 119.
Nellis, W., A. Mitchell, P. McCandless, D. Erskine, and S. Weir, 1992, Phys. Rev. Lett. **68**, 2937.
Nellis, W., A. Mitchell, M. V. Thiel, G. Devine, R. Trainor, and N. Brown, 1983, J. Chem. Phys. **79**, 1480.
Nellis, W., M. Ross, A. Mitchell, M. V. Thiel, D. Young, F. Ree, and R. Trainor, 1983, Phys. Rev. A **27**, 608.
Nellis, W. J., 2006a, Rep. Prog. Phys. **69**, 1479.
Nellis, W. J., 2006b, Rep. Prog. Phys. **69**, 1479.
Nellis, W. J., N. C. Holmes, A. C. Mitchell, R. J. Trainor, G. K. Governo, M. Ross, and D. A. Young, 1984, Phys. Rev. Lett. **53**, 1248.
Nellis, W. J., A. L. Ruoff, and I. F. Silvera, 2012, arXiv:1201.0407.
Nellis, W. J., S. T. Weir, and A. C. Mitchell, 1996, Science **273**, 936.
Nellis, W. J., S. T. Weir, and A. C. Mitchell, 1999, Phys. Rev. B **59**, 3434.
Nettelmann, N., A. Becker, B. Holst, and R. Redmer, 2012, Astrophys. J. **750**, 52.
Nettelmann, N., B. Holst, A. Kietzmann, M. French, R. Redmer, and D. Blaschke, 2008, Astrophys. J. **683**, 1217.
Norman, G. E., and A. N. Starostin, 1970, J. Appl. Spectrosc. **13**, 965.
Oliva, J., and N. W. Ashcroft, 1981a, Phys. Rev. B **24**, 6200.
Oliva, J., and N. W. Ashcroft, 1981b, Phys. Rev. B **23**, 6399.
Onida, G., L. Reining, and A. Rubio, 2002, Rev. Mod. Phys. **74**, 601.
Overhauser, A. W., 1984, Phys. Rev. Lett. **53**, 64.
Parr, R. G., and Y. Weitao, 1994, *Density Functional Theory of Atoms and Molecules* (Oxford University Press, New York).
Payne, M. C., M. P. Teter, D. C. Allan, T. A. Arias, and J. D. Joannopoulos, 1992, Rev. Mod. Phys. **64**, 1045.
Perdew, J., K. Burke, and M. Ernzerhof, 1996, Phys. Rev. Lett. **77**, 3865.
Perdew, J. P., and K. Schmidt, 2001, in *Density Functional Theory and Its Application to Materials*, edited by V. Van Doren, C. Van Alsenoy, and P. Geerlings, AIP Conf. Proc. No. 577 (AIP, New York), p. 1.
Perdew, J., and A. Zunger, 1981, Phys. Rev. B **23**, 5048.
Perdew, J. P., M. Ernzerhof, and K. Burke, 1996, J. Chem. Phys. **105**, 9982.
Perdew, J. P., and M. Levy, 1983, Phys. Rev. Lett. **51**, 1884.
Pfaffenzeller, O., and D. Hohl, 1997, J. Phys. Condens. Matter **9**, 11 023.
Pfaffenzeller, O., D. Hohl, and P. Ballone, 1995, Phys. Rev. Lett. **74**, 2599.
Pickard, C. J., M. Martinez-Canales, and R. J. Needs, 2012a, Phys. Rev. B **85**, 214114.
Pickard, C. J., M. Martinez-Canales, and R. J. Needs, 2012b, Phys. Rev. B **86**, 059902(E).
Pickard, C. J., and R. J. Needs, 2006, Phys. Rev. Lett. **97**, 045504.
Pickard, C. J., and R. J. Needs, 2007, Nature Phys. **3**, 473.
Pickard, C. J., and R. J. Needs, 2009, Phys. Status Solidi B **246**, 536.
Pierleoni, C., D. Ceperley, B. Bernu, and W. Magro, 1994, Phys. Rev. Lett. **73**, 2145.
Pierleoni, C., and D. M. Ceperley, 2005, Chem. Phys. Chem. **6**, 1872.
Pierleoni, C., and D. M. Ceperley, 2006, *Lecture Notes in Physics* Vol. 703, p. 641.
Pierleoni, C., D. M. Ceperley, and M. Holzmann, 2004, Phys. Rev. Lett. **93**, 146402.
Pierleoni, C., K. Delaney, M. Morales, D. Ceperley, and M. Holzmann, 2008, Comput. Phys. Commun. **179**, 89.
Pierleoni, C., W. R. Magro, D. M. Ceperley, and B. Bernu, 1996, in *Physics of Strongly Coupled Plasmas*, edited by W. D. Kraeft and M. Schlanges (World Scientific, Singapore).
Pollock, E. L., and B. J. Alder, 1977, Phys. Rev. A **15**, 1263.
Pollock, E. L., and J. P. Hansen, 1973, Phys. Rev. A **8**, 3110.
Raich, J. C., and H. M. James, 1966, Phys. Rev. Lett. **16**, 173.
Ramaker, D. E., L. Kumar, and F. E. Harris, 1975, Phys. Rev. Lett. **34**, 812.
Redmer, R., and B. Holst, 2010, in *Metal-to-Nonmetal Transitions*, edited by R. Redmer, F. Hensel, and B. Holst, Springer Series in Materials Science (Springer, Berlin), Vol. 132, p. 63.
Richardson, C. F., and N. W. Ashcroft, 1997, Phys. Rev. Lett. **78**, 118.
Robitaille, P.-M., 2011, Prog. Phys. **3**, 60.
Ross, M., 1998, Phys. Rev. B **58**, 669.
Ross, M., F. Ree, and D. Young, 1983, J. Chem. Phys. **79**, 1487.
Ross, M., and D. Seale, 1974, Phys. Rev. A **9**, 396.
Rousseau, B., Y. Xie, Y. Ma, and A. Bergara, 2011, Eur. Phys. J. B **81**, 1.
Runge, K. J., M. P. Surh, C. Mailhiot, and E. L. Pollock, 1992, Phys. Rev. Lett. **69**, 3527.
Sano, T., N. Ozaki, T. Sakaiya, K. Shigemori, M. Ikoma, T. Kimura, K. Miyanishi, T. Endo, A. Shiroshita, and H. Takahashi, 2011a, Phys. Rev. B **83**, 054117.
Sano, T., *et al.*, 2011b, Phys. Rev. B **83**, 054117.
Santamaria-Perez, D., G. D. Mukherjee, B. Schwager, and R. Boehler, 2010, Phys. Rev. B **81**, 214101.
Saumon, D., 2007, AIP Conf. Proc. **955**, 101.
Saumon, D., and G. Chabrier, 1989, Phys. Rev. Lett. **62**, 2397.
Saumon, D., and G. Chabrier, 1991, Phys. Rev. A **44**, 5122.
Saumon, D., and G. Chabrier, 1992, Phys. Rev. A **46**, 2084.
Saumon, D., G. Chabrier, and H. van Horn, 1995, Astrophys. J. Suppl. Ser. **99**, 713.
Saumon, D., and T. Guillot, 2004, Astrophys. J. **609**, 1170.
Savrasov, S. Y., and D. Y. Savrasov, 1996, Phys. Rev. B **54**, 16 487.
Scandolo, S., 2003, Proc. Natl. Acad. Sci. U.S.A. **100**, 3051.
Sham, L. J., and M. Schlüter, 1983, Phys. Rev. Lett. **51**, 1888.
Silvera, I., and V. Goldman, 1978, J. Chem. Phys. **69**, 4209.
Silvera, I. F., 1980, Rev. Mod. Phys. **52**, 393.
Silvera, I. F., and S. Deemyad, 2009, Low Temp. Phys. **35**, 318.
Silvera, I. F., and R. J. Wijngaarden, 1981, Phys. Rev. Lett. **47**, 39.
Smoluchowski, R., 1967, Nature (London) **215**, 691.
Souvatzis, P., O. Eriksson, M. I. Katsnelson, and S. P. Rudin, 2008, Phys. Rev. Lett. **100**, 095901.
Städele, M., J. A. Majewski, P. Vogl, and A. Görling, 1997, Phys. Rev. Lett. **79**, 2089.
Städele, M., and R. M. Martin, 2000, Phys. Rev. Lett. **84**, 6070.
Städele, M., M. Moukara, J. A. Majewski, P. Vogl, and A. Görling, 1999, Phys. Rev. B **59**, 10 031.
Stevenson, D. J., 1975, Phys. Rev. B **12**, 3999.
Stevenson, D. J., 1979, J. Phys. F **9**, 791.
Stevenson, D. J., 1982, Annu. Rev. Earth Planet Sci. **10**, 257.
Stevenson, D. J., 2008, Proc. Natl. Acad. Sci. U.S.A. **105**, 11 035.
Stevenson, D. J., 2010 (private communication).
Stevenson, D. J., and E. E. Salpeter, 1977a, Astrophys. J. Suppl. Ser. **35**, 239.

Stevenson, D. J., and E. E. Salpeter, 1977b, Astrophys. J. Suppl. Ser. **35**, 221.
Stixrude, L., and R. Jeanloz, 2008, Proc. Natl. Acad. Sci. U.S.A. **105**, 11 071.
Straus, D. M., and N. W. Ashcroft, 1977, Phys. Rev. Lett. **38**, 415.
Straus, D. M., N. W. Ashcroft, and H. Beck, 1977, Phys. Rev. B **15**, 1914.
Subramanian, N., A. Goncharov, V. Struzhkin, M. Somayazulu, and R. Hemley, 2011, Proc. Natl. Acad. Sci. U.S.A. **108**, 6014.
Surh, M. P., T. W. Barbee, III, and C. Mailhiot, 1993, Phys. Rev. Lett. **70**, 4090.
Surh, M. P., K. J. Runge, T. W. Barbee, E. L. Pollock, and C. Mailhiot, 1997, Phys. Rev. B **55**, 11330.
Szczesniak, R., and M. W. Jarosik, 2009, Solid State Commun. **149**, 2053.
Takahashi, M., and M. Imada, 1984, J. Phys. Soc. Jpn. **53**, 3765.
Tamblyn, I., and S. Bonev, 2010a, Phys. Rev. Lett. **104**, 065702.
Tamblyn, I., and S. A. Bonev, 2010b, J. Chem. Phys. **132**, 134503.
Ternovoi, V. Y., A. S. Filimonov, A. A. Pyalling, V. B. Mintsev, and V. E. Fortov, 2002, AIP Conf. Proc. **620**, 107.
Theilhaber, J., 1992, Phys. Fluids B **4**, 2044.
Thomas, L. H., 1927, Math Proc. Cambridge Philos. Soc. **23**, 542.
Tkatchenko, A., and M. Scheffler, 2009, Phys. Rev. Lett. **102**, 073005.
Totsuji, H., and K. Tokami, 1984, Phys. Rev. A **30**, 3175.
Toulouse, J., and C. J. Umrigar, 2007, J. Chem. Phys. **126**, 084102.
Trotter, H., 1959, Proc. Am. Math. Soc. **10**, 545.
Tuckerman, M. E., B. J. Berne, G. J. Martyna, and M. L. Klein, 1993, J. Chem. Phys. **99**, 2796.
Tuckerman, M. E., and M. Parrinello, 1994a, J. Chem. Phys. **101**, 1302.
Tuckerman, M. E., and M. Parrinello, 1994b, J. Chem. Phys. **101**, 1316.
Umrigar, C. J., J. Toulouse, C. Filippi, S. Sorella, and R. G. Hennig, 2007, Phys. Rev. Lett. **98**, 110201.
Umrigar, C. J., K. G. Wilson, and J. W. Wilkins, 1988, Phys. Rev. Lett. **60**, 1719.
van Kessel, C. G. M., and R. Sigel, 1974, Phys. Rev. Lett. **33**, 1020.
van Thiel, M., and B. J. Alder, 1966, Mol. Phys. **10**, 427.
van Thiel, M., M. Ross, B. Hord, A. Mitchell, W. Gust, M. D'Addario, R. Keeler, and K. Boutwell, 1973, Phys. Rev. Lett. **31**, 979.
Vieillefosse, P., and J. P. Hansen, 1975, Phys. Rev. A **12**, 1106.
von Zahn, U., D. M. Hunten, and G. Lehmacher, 1998, J. Geophys. Res. **103**, 22 815.
Vorberger, J., I. Tamblyn, St. A. Bonev, and B. Militzer, 2007, Contrib. Plasma Phys. **47**, 375.
Vorberger, J., I. Tamblyn, B. Militzer, and S. Bonev, 2007, Phys. Rev. B **75**, 024206.
Vos, W. L., M. G. E. van Hinsberg, and J. A. Schouten, 1990, Phys. Rev. B **42**, 6106.
Vuilleumier, R., 2006, in *Computer Simulations in Condensed Matter Systems: From Materials to Chemical Biology Volume 1*, edited by M. Ferrario, G. Ciccotti, and K. Binder, Lecture Notes in Physics Vol. 703 (Springer, Berlin), p. 223.
Wang, X. W., J. Zhu, S. G. Louie, and S. Fahy, 1990, Phys. Rev. Lett. **65**, 2414.
Wang, Y., J. Lv, L. Zhu, and Y. Ma, 2010, Phys. Rev. B **82**, 094116.
Weir, S., 1998, J. Phys. Condens. Matter **10**, 11147.
Weir, S., A. Mitchell, and W. Nellis, 1996, Phys. Rev. Lett. **76**, 1860.
Whitmore, M. D., J. P. Carbotte, and R. C. Shukla, 1979, Can. J. Phys. **57**, 1185.
Wigner, E., and H. B. Huntington, 1935, J. Chem. Phys. **3**, 764.
Winisdoerfer, C., and G. Chabrier, 2005, Phys. Rev. E **71**, 026402.
Woodley, S. M., and R. Catlow, 2008, Nature Mater. **7**, 937.
Xu, H., J.-P. Hansen, and D. Chandler, 1994, Europhys. Lett. **26**, 419.
Yarnell, J. L., R. L. Mills, and A. F. Schuch, 1975, Sov. J. Low Temp. Phys. **1**, 366.
Zeldovich, Y. B., and Y. P. Raizer, 1967, *Physics of Shock Waves and High Temperature Phenomena* (Academic Press, New York).
Zerah, G., J. Clerouin, and E. Pollock, 1992, Phys. Rev. Lett. **69**, 446.
Zha, C.-S., Z. Liu, and R. J. Hemley, 2012, Phys. Rev. Lett. **108**, 146402.
Zha, C.-S., H.-k. Mao, and R. J. Hemley, 2004, Phys. Rev. B **70**, 174107.
Zhang, L. J., Y. L. Niu, T. Cui, Y. Li, Y. M. Ma, Z. He, and G. T. Zou, 2007, J. Phys. Condens. Matter **19**, 425237.
Zhang, L. J., Y. L. Niu, T. Cui, Y. Li, Y. Wang, Y. M. Ma, Z. He, and G. T. Zou, 2006, J. Phys. Condens. Matter **18**, 9917.